



THE HONG KONG  
POLYTECHNIC UNIVERSITY

香港理工大學

Pao Yue-kong Library

包玉剛圖書館

---

## Copyright Undertaking

This thesis is protected by copyright, with all rights reserved.

**By reading and using the thesis, the reader understands and agrees to the following terms:**

1. The reader will abide by the rules and legal ordinances governing copyright regarding the use of the thesis.
2. The reader will use the thesis for the purpose of research or private study only and not for distribution or further reproduction or any other purpose.
3. The reader agrees to indemnify and hold the University harmless from and against any loss, damage, cost, liability or expenses arising from copyright infringement or unauthorized usage.

### IMPORTANT

If you have reasons to believe that any materials in this thesis are deemed not suitable to be distributed in this form, or a copyright owner having difficulty with the material being included in our database, please contact [lbsys@polyu.edu.hk](mailto:lbsys@polyu.edu.hk) providing details. The Library will look into your claim and consider taking remedial action upon receipt of the written requests.

Pao Yue-kong Library, The Hong Kong Polytechnic University, Hung Hom, Kowloon, Hong Kong

<http://www.lib.polyu.edu.hk>

**INTERFACIAL MECHANICS IN  
BI-MATERIALS AND STRUCTURES**

GAO YANG

PhD

The Hong Kong Polytechnic University

2020



The Hong Kong Polytechnic University

Department of Mechanical Engineering

# **Interfacial Mechanics in Bi-materials and Structures**

GAO Yang

A thesis submitted in partial fulfilment of the requirements for the degree of

Doctor of Philosophy

January 2020



## CERTIFICATE OF ORIGINALITY

I hereby declare that this thesis is my own work and that, to the best of my knowledge and belief, it reproduces no material previously published or written, nor material that has been accepted for the award of any other degree or diploma, except where due acknowledgement has been made in the text.

\_\_\_\_\_ (Signed)

GAO YANG (Name of student)



*Lovingly dedicated to my family*



## Abstract

Bi-materials and structures are broadly adopted in nature and engineering due to their ability to take advantage of the merits of individual constituents and to minimize their weaknesses. However, there are some interfacial problems impairing their mechanical performance. For example, the interface between the two materials is often much weaker than the bulk constituents, making interfacial crack and subsequent interfacial delamination easy to happen. This problem would become even worse when stress concentration is present on the interface due to the strain misfit between the two distinct materials. This thesis would focus on solving these interface-related problems for an enhanced or controllable mechanical performance in bi-materials and structures.

In Chapter 4, a micro-screw dislocation ( $\mu$ -SD) found in biological laminated composites was systematically studied. Mechanical tests indicate that  $\mu$ -SDs can greatly enhance the resistance to scratching. Finite element analysis was performed to shed light on the underlying reinforcing mechanism. Results show that the failure of a  $\mu$ -SD under tension involves the delamination of the prolonged spiral interface, thus giving rise to more energy consumption and higher toughness compared with the planar counterparts. The operation of such reinforcing mechanism requires proclivity of cracking along the spiral interface. Fracture mechanics-based modelling indicates that if the fracture toughness of interface is less than 60% of that of the lamina material,

crack would always propagate along the interface. These findings not only reveal the reinforcing mechanism of spiral interface but also imply a great promise of applying  $\mu$ -SDs in laminated composites for higher fracture toughness.

Interfaces in bi-materials such as film-substrate systems are often subjected to shear stress due to distinct deformation responses of two bonded materials to the external stimuli. The distribution of such shear stress over the interface normally exhibits high concentration. To enhance the interface's resistance to delamination, a gradient thickness strategy was proposed to homogenize interfacial shear stress caused by strain misfit in film-substrate bi-material systems in Chapter 5. The solutions to the gradient thickness in the films were obtained based on two typical bi-material systems: continuous film on disk-like substrate and island film on half-space substrate. The effectiveness of these theoretical solutions were well demonstrated via finite element simulation and experimental test. This strategy is believed to be of great value to the enhancement of resistance to interface delamination in diverse film-substrate systems.

The strain misfit between the two bonded materials can be exploited instead to achieve controllable morphing behaviors for a broad range of applications. In Chapter 6, the deformation of stacked assembly of graphene (SAG)/polyethylene (PE) bilayer under thermal loadings was systematically studied via a combination of theoretical modelling and finite element simulation. As SAG layer has asymmetric

elastoplastic properties, i.e., high plasticity under tension and high elasticity under compression, the strain misfit between the two bonded materials can originate from either thermal mismatch or plastic strain. Through theoretical analysis, the morphing behaviors of SAG/PE bilayer under different thermal loadings were well predicted. These results would provide valuable guidelines when applying such bi-materials in the field of sensors, actuators and soft robotics, etc.

Through our investigation, several strategies and guidelines were proposed to resolve the interface-related problems in bi-materials and structures. These results would be of significant value for the design of bi-materials and structures with enhanced or controllable mechanical behaviors.



## Publications Arising from the Thesis

1. **Yang Gao**<sup>†</sup>, Zhenbin Guo<sup>†</sup>, Zhaoqiang Song, Haimin Yao. Spiral interface: A reinforcing mechanism for laminated composite materials learned from nature. *Journal of the Mechanics and Physics of Solids*, 2017, 109: 252-263. (†Co-first authors)
2. **Yang Gao**, Haimin Yao. Homogenizing interfacial shear stress via thickness gradient. *Journal of the Mechanics and Physics of Solids*, 2019, 131: 112-124.
3. Shuai Wang<sup>†</sup>, **Yang Gao**<sup>†</sup>, Anran Wei<sup>†</sup>, Peng Xiao, Yun Liang, Wei Lu, Chinyin Chen, Chi Zhang, Guilin Yang, Haimin Yao, Tao Chen. Asymmetric elastoplasticity of stacked graphene assembly actualizes programmable untethered soft robotics. *Nature Communications*, accepted. (†Co-first authors)
4. Haimin Yao, Zhenbin Guo, **Yang Gao**. Inhomogeneous Si distribution in Si-based lithium-ion batteries. In application of Chinese patent.

## Conference Presentations

1. **Yang Gao**, Zhenbin Guo, Zhaoqiang Song, Haimin Yao. Spiral interface: A reinforcing mechanism for laminated composite materials learned from nature. Poster presentation at the *Gordon Research Conference (GRC) on Nano-Mechanical Interfaces*, July 30-August 4, 2017, Hong Kong.
2. **Yang Gao**, Zhenbin Guo, Zhaoqiang Song, Haimin Yao. Spiral interface: A reinforcing mechanism for laminated composite materials learned from biomaterials. Oral presentation at the *18th U.S. National Congress for Theoretical and Applied Mechanics*, June 5-9, 2018, Chicago.

## Acknowledgements

Three years of PhD study is approaching the end, which will also be the end of my study career. At this moment, I want to express my sincere gratitude to all the people who have ever helped, encouraged, criticized, inspired me during this period.

First of all, I would like to express my deepest appreciation to my supervisor, Dr. Haimin Yao. During the past three years, he imparted me not only plenty of knowledge in mechanics and material science, but also the method and ability to solve problems. Whenever I got lost or confused, he could always guide me back to the right direction. His insight and creativity endowed me a lot of inspirations, and his diligent and energetic working attitude motivated me to be like him. Under his guidance, I really realized the joy from scientific research. I am so lucky to be one of his students, and what I have learned from him will be beneficial for my whole life.

Secondly, I would like to thank my colleagues, Mr. Zhenbin Guo and Mr. Zhaoqiang Song. We worked together to accomplish the research on the spiral interface reinforced composites. I also appreciate the helpful discussions with Mr. Anran Wei on the morphing behaviors of SAG/PE bilayer material.

It is lucky to work with the lovely members in the Bio-inspired Mechanics and Structures (BiMS) Group, including Dr. Weiqun Li, Dr. Qifang Yin, Dr. Jimin Fu, Mr. Zhenbin Guo, Mr. Juntan Yang, Miss Yanwei Xue, Mr. Zhaoqiang Song, Mr.

Zhenbang Li, Dr. Ji Lin, Mr. Andre Eccel Vellwock, Mr. Anran Wei, Mr. Wenhao Sha and Miss Yujie Xie. It is an unforgettable memory to play and hang out with these intelligent and lovely friends. Thanks for your company along the way.

Many thanks go to technical staff including Dr. Curtis Ng, Mr. Benny Leung, Mr. Jack Wong, Mr. Kam-keung Tang, Mr. Ka-on Yuen, and the administrative staff including Ms. Lily Tam, Mrs. Michelle Lai, Ms. Celia Wong. Thanks extend to the colleagues in ME department who have ever helped me during my doctoral period.

Last but not least, I would like give my sincere gratitude to my beloved parents and grandparents for their long-lasting understanding, support and encouragement. Also, I must thank my husband Yang Liu, who has push me forward and let me conquer all the difficulties over the past three years.

# Table of Contents

Abstract .....	I
Publications Arising from the Thesis .....	V
Conference Presentations .....	VI
Acknowledgements.....	VII
Table of Contents .....	IX
List of Figures.....	XI
List of Tables .....	XVIII
Chapter 1. Introduction .....	1
1.1 Typical bi-materials and structures.....	1
1.2 Interface-related problems in bi-materials and structures.....	4
1.3 Objectives and outline of this thesis .....	7
Chapter 2. Research background and literature review .....	9
2.1 Strategies to increase mechanical properties of bi-materials and structures .....	9
2.2 Strategies to reduce stress concentration on interface .....	23
2.3 Controllable deformation of bi-materials by utilizing strain misfit .....	33
Chapter 3. Research methods .....	45
3.1 Experimental method.....	45
3.2 Theoretical method.....	46

Chapter 4.	Spiral interface reinforced laminated composite.....	61
4.1	Characterization of mechanical reinforcement .....	62
4.2	Numerical verification of the reinforcement of spiral interface .....	65
4.3	Theoretical prediction of mechanical behaviors of $\mu$ -SD.....	70
4.4	Working condition for the reinforcing mechanism of $\mu$ -SD.....	78
4.5	Summary.....	82
Chapter 5.	Homogenizing interfacial shear stress in bi-materials via thickness gradient .....	85
5.1	Theoretical modelling.....	86
5.2	Experimental validation.....	105
5.3	Summary.....	108
Chapter 6.	Controllable morphing behavior of SAG/PE bi-material by utilizing strain misfit.....	111
6.1	Deformation of SAG/PE bi-material driven by thermal misfit.....	112
6.2	Deformation of SAG/PE bi-material driven by plastic strain.....	119
6.3	Summary.....	129
Chapter 7.	Conclusions and future work .....	131
7.1	Conclusions.....	131
7.2	Outlook to the future work .....	134
References.....		136

## List of Figures

- Figure 1.1 Hard biological tissues. (a) tooth, (b) bone, and (c) nacre are bi-material composites with hard-mineral platelets embedded in a soft protein matrix. (d) The enamel of tooth is composed of needle-like crystals embedded in soft organic matrix. (e) Dentin and cortical bone are made of mineral plates staggered in protein matrix. (f) Nacre is composed of plate crystals with small quantity of soft matrix in between (adapted from [8]). ..... 2
- Figure 1.2 Schematic diagram of (a) particle reinforced composite, (b) fiber reinforced composite and (c) laminated composite. .... 3
- Figure 1.3 (a) Particle/matrix interface delamination and microcrack coalescence observed in particle-reinforced composites under compressive loading (adapted from [16]). (b) Fiber/matrix interface delamination observed in fiber-reinforced composites after flexural testing (adapted from [17]). ... 5
- Figure 1.4 (a) Ceramic thermal barrier coating delaminated from superalloy substrate after thermal cycles (adapted from [22]). (b) Si-based electrode film of lithium-ion battery detached from the current collector (copper foil) after lithiation/delithiation cycles. .... 6
- Figure 2.1 Biological suture structures in nature. (a) Diagram of suture structure consisting of rigid teeth and compliant interface; (b) Osteoderm sutures in red-eared slider; (c) Cranial sutures in white-tailed deer; (d) Pelvic sutures in stickleback; (e) Scute sutures in boxfish; (f) Exoskeletal sutures in diatom; (g) Hierarchical sutures in *Craspedites nodiger*; (h) Suture on the seedcoat of *Portulaca oleracea*. Scale bars: (b) 1 mm, (c) 1 cm, (d) 1 mm, (e) 500  $\mu\text{m}$ , (f) 1  $\mu\text{m}$ , (g) 1 cm, (h) 50  $\mu\text{m}$ . ((a-f) adapted from [26], (g) adapted from [27], (h) adapted from [28])..... 11
- Figure 2.2 Contour of the normalized strength of suture structure as a function of the component strengths and suture tooth angle. (Adapted from [29])..... 13
- Figure 2.3 Overview of the design of bi-stable interlocked tabs. (a) The schematic diagram showing the profile of the tab; (b) Pullout process of the bi-stable interlocked tabs. During this process, there are two stable

positions in this system, which would result in more energy consumption. (Adapted from [36]) .....	14
Figure 2.4 Schematic of some toughening mechanisms around a propagating crack tip in nacre. (Adapted from [10]) .....	18
Figure 2.5 (a) STEM and (b) TEM image showing the mineral bridges at the platelet-platelet interface in nacre. ((a) adapted from [77], (b) adapted from [80]) (c) SEM image showing the interlocks between the platelets in nacre; (d) Schematic illustration showing the interlocks between the platelets in nacre. ((c, d) adapted from [78]) .....	21
Figure 2.6 Comparison of microstructures of (a-c) natural nacre and (d-f) nacre-like alumina. (a, d) SEM images showing the short and long-range orders of platelets. (b, e) Local stacking of platelets. Liquid phases is presented in (e) mimicking the protein layer in nacre. (c, f) Closer views of the platelet interface. Inorganic bridges and nano-asperities can be observed at the platelets interface in (f). (Adapted from [81]) .....	22
Figure 2.7 Fabrication protocol for nacre-like glass panels. (Adapted from [82]) ....	23
Figure 2.8 (a) Two structures are bonded together and subject to an external load. (b) Stress concentration occurs at interface edge. The spring represents the molecular interaction forces between the contacting surfaces. (c) Uniform tensile stress distribution at interface. (d) The optimal shape profile of a rigid fiber tip for a uniform tensile stress distribution. (Adapted from [83]) .....	25
Figure 2.9 SEM images of fibrillar PDMS surfaces with different tip shapes: (a) flat, (b) spherical, (c) flat with rounded edges, (d) spatula, (e) mushroom, (g) concave tips. (f) Comparison of pull-off force for different tip shapes under different preloads. (Adapted from [88]) .....	27
Figure 2.10 Different geometrical models for fibers with mushroom tip. ((a) adapted from [89], (b) adapted from [85], (c) adapted from [90]) .....	28
Figure 2.11 (a) Dental-enamel junction (DEJ) of human teeth (Adapted from [26]), and gradient elastic modulus and hardness at DEJ (Adapted from [96]). (b) Fish with gradient scales (Adapted from [26]) .....	30

Figure 2.12 EDS mapping of Si element for (a) gradient and (b) homogeneous Si-based anodes. Cross-section of (c) gradient and (d) homogeneous Si-based anodes after 500 discharge-charge cycles. (Adapted from [23]) .....31

Figure 2.13 Morphology of *Selaginella lepidophylla* under (a) dry and (b) wet state. (c) Curling sequence of fully hydrated inner stems during dehydration. (Adapted from [106]).....34

Figure 2.14 Deflection of bi-material strip subject to uniform heating. (Adapted from [108]) .....35

Figure 2.15 (a) Bilayer actuator with two legs attached. The static friction coefficients of the end tips and knees of legs are different. (b) Advance of actuator under periodic humidity variation. ((a, b) adapted from [115].) (c) Self-propelling robot in fabricated configuration. (d) Self-propelling robot in rolling configuration. (e) The self-propelling locomotion process of robot when heated. ((c-e) adapted from [109].) (f) The swimming of a bilayer actuator under cyclic UV light. (g) Schematic of the self-propelling actuator mimicking the dolphin. ((f, g) adapted from [118].).....37

Figure 2.16 (a) The fabrication of buckling wrinkles on metal film-PDMS substrate system. (b-e) Optical micrographs showing the diverse buckling wave patterns. (b) Disordered regions far from any steps or edges. (c) A flat waveless region near edge gradually becomes a system with well aligned waves guided by the rectangular ridges. (d) Flat squares elevated relative to the surface exhibits no buckling on the plateau, but ordered wave patterns on the recessed regions between them. (e) Rectangular ridges directed the waves parallel to the direction of the protruding portion of PDMS. (Adapted from [121]) .....40

Figure 2.17 (a) Schematic diagram of the fabrication protocol of concave microlens array. (Adapted from [127].) (b) Schematic illustration of the process for building stretchable Si devices on elastomeric substrate. (Adapted from [128]) .....41

Figure 3.1 Free body diagram of an infinitesimal element in Cartesian coordinate...47

Figure 3.2 Free body diagram of an infinitesimal element in polar coordinate.....	49
Figure 3.3 An infinite plate with a crack subject to a remote tensile stress.....	52
Figure 3.4 (a) An infinite plate with an angled crack subject to a remote tensile loading. (b) Infinitesimal kink at the tip of a macroscopic crack. ....	55
Figure 3.5 (a) Two-dimensional discrete domain, (b) Three-node triangle element..	56
Figure 4.1 (a) Translucent shells of <i>P. placenta</i> . (b) False-colored SEM image of $\mu$ -SDs in the shell of <i>P. placenta</i> with opposite helicity.....	63
Figure 4.2 (a) A scratch groove passing through a $\mu$ -SD and the corresponding real-time resistance force experienced by the probe. (b) The three-dimensional reconstruction of $\mu$ -CT model of the scratched surface and the depth contour of the scratch groove obtained by surface scanning (Hysitron Ti 900).....	65
Figure 4.3 Schematics of finite element models for laminated composites with (a) spiral and (b) parallel planar interfaces. $D=18 \mu\text{m}$ , $l=15 \mu\text{m}$ and $p=1 \mu\text{m}$ ; (c) Calculated stress-strain curves for two models under uniaxial tension. $S_I$ , $S_{II}$ , $E_I$ and $E_{III}$ are the characteristic mechanical properties of $\mu$ -SD predicted by theory; (d, e) Snapshots of the SDEG (scalar stiffness degradation variable) field at different moments as indicated on the stress-strain curves in (c) showing the evolution of the interface damage. The deep blue color (SDEG=0) represents zero damage while the deep red color (SDEG=1.0) stands for the complete damage. For clarity, the lamina phase is hidden here. ....	67
Figure 4.4 (a) SEM image of an area ( $90 \mu\text{m} \times 70 \mu\text{m}$ ) on shell of <i>P. Placenta</i> containing 17 $\mu$ -SDs as marked by the yellow arrows. The areal density is estimated to be $\approx 2,700 \text{ mm}^{-2}$ . (b) Schematics of an idealized composite model containing periodically distributed $\mu$ -SD couples. A representative volume element (RVE) with dimensions of $2D' \times 2D'$ is highlighted in green. (c) Calculated stress-strain curves for composites with $\mu$ -SDs of different areal densities using the RVE model shown in (b). ....	69
Figure 4.5 (a) Schematics of traction-separation law for bilinear cohesive elements	

modelling adhesive interface, (b) Schematic stress-strain curve of $\mu$ -SD under uniaxial tension. ....	72
Figure 4.6 Dependence of $S_{II}/S_I$ of a $\mu$ -SD on the length scale characterized by $D$ . Here, following representative values are taken: $G_{in}=1.0 \text{ J/m}^2$ , $K_{in}=1.25 \text{ GPa}/\mu\text{m}$ , $S_{in}=10 \text{ MPa}$ , $E_{la}=100 \text{ GPa}$ and $Q=2.4$ . ....	75
Figure 4.7 (a) Schematics of a unit segment of $\mu$ -SD with failed interface. (b) Free body diagram of an annular element for analysis and its analogy.....	76
Figure 4.8 The crack frontier of a spiral interface in (a) is equated to a 2D (plane strain) mixed-mode crack shown in (b). ....	79
Figure 5.1 (a) Schematics of a bi-material consisting of a circular film on a disk-like substrate. The nonuniform thickness of the film is to be determined so that the interfacial shear stress induced by strain misfit, if available, is uniform and equal to $\tau_{de}$ . Here, the direction of the shear stress plotted is based on the assumption that $\varepsilon_{f0} > \varepsilon_{s0}$ . If $\varepsilon_{f0} < \varepsilon_{s0}$ , the direction of the shear stress should be opposite or $\tau_{de} < 0$ . (b, c) Free body diagrams of infinitesimal elements in the substrate and film, respectively.....	88
Figure 5.2 (a) Profile of the optimal gradient film thickness. (b) The simulated shear stress field on the interface between the thin film and substrate at different degrees of strain misfit. Parameters adopted: $E_f=100 \text{ GPa}$ , $\nu_f=0.3$ , $E_s=200 \text{ GPa}$ , $\nu_s=0.25$ , $R=10 \text{ mm}$ , $t_s=10 \mu\text{m}$ , $\varepsilon_{mis}=1\%$ and $\tau_{de}=1 \text{ MPa}$ . The stiffness of the cohesive interface is taken as $100 \text{ GPa}/\text{mm}$ . ..	95
Figure 5.3 (a) Schematics of a bi-material consisting of a circular island film on a half-space substrate. The thickness of the film is to be optimized so that the interfacial shear stress induced by strain misfit, if available, is uniform and equal to $\tau_{de}$ as shown in (b). ....	97
Figure 5.4 (a) Profile of the optimal nonuniform island film thickness. (b) The simulated shear stress field on the interface between the thin film and substrate at different degrees of strain misfit. Parameters adopted: $E_f=100 \text{ GPa}$ , $\nu_f=0.3$ , $E_s=200 \text{ GPa}$ , $\nu_s=0.25$ , $R=10 \text{ mm}$ , $\varepsilon_{mis}=1\%$ and $\tau_{de}=1 \text{ MPa}$ . The stiffness of the cohesive interface is taken as $100 \text{ GPa}/\text{mm}$ . ....	100

Figure 5.5 Variation of  $g(\bar{r})$  with  $\bar{r}$  in comparison with its asymptotic form of  $2/\bar{r}$ . Here, the Poisson's ratio of the film is taken as  $\nu_f=0.3$ . ..... 102

Figure 5.6 (a) Linear approximations of the optimal thickness profiles of island film for different  $\varphi$ . (b) The simulated shear stress field on the interface between the island film and substrate under the strain misfit  $\varepsilon_{\text{mis}}$ . Here,  $E_f=100$  GPa,  $\nu_f=0.3$ ,  $E_s=200$  GPa,  $\nu_s=0.25$ ,  $R=10$  mm,  $\varepsilon_{\text{mis}}=1\%$  and  $\tau_{\text{de}}=0.277, 2.773, 27.733$  or  $277.333$  MPa. The stiffness of the cohesive interface is taken as 100 GPa/mm. .... 103

Figure 5.7 (a) Thickness profiles of the optimal gradient film and uniform control. (b) Schematics of the experimental setups (units: mm). (c) Shear strain field ( $\varepsilon_{xy}$ ) on the side surface under a tensile loading  $\sigma_t = 173.3$  MPa, which was obtained by DIC analysis using software Nccor with the subset size, subset spacing and strain radius being taken as 40 pixels, 1 pixel and 15 pixels, respectively. (d) Shear strain ( $\varepsilon_{xy}$ ) distribution along the interface between film and substrate under tensile loading  $\sigma_t = 173.3$  MPa. .... 108

Figure 6.1 Asymmetric mechanical properties of SAG layer under tension and compression. (Adapted from [181]) ..... 113

Figure 6.2 Bending of SAG/PE bilayer under uniform heating ..... 114

Figure 6.3 Maximum temperature increment ( $\Delta T_e$ ) for SAG/PE bilayer without triggering plastic deformation in SAG layer. Parameters adopted:  $E_{\text{PE}}=300$  MPa,  $\nu_{\text{PE}}=0.46$ ,  $t_{\text{PE}}=10$   $\mu\text{m}$ ,  $\alpha=4\times 10^{-4}/^\circ\text{C}$ ,  $E_{\text{SAG}}^t=20.7$  GPa,  $S_{\text{SAG}}^t=20.4$  MPa,  $E_{\text{SAG}}^c=2.2$  GPa,  $\nu_{\text{SAG}}=0.19$ . .... 119

Figure 6.4 Schematic illustration showing the constrained tempering process of SAG/PE bilayer. (a) An SAG/PE bilayer is sandwiched by two rigid plates. (b) Upon heating by  $\Delta T$ , the PE layer expands laterally, resulting in tensile force in SAG layer and compressive force in PE layer. (c) Upon cooling, the PE layer would return to its initial configuration while the deformation in SAG layer cannot be fully recovered due to the plastic deformation in step (b), resulting in the residual tensile force in PE layer and residual compressive force in SAG layer. (d) After releasing the constraint of the plates, the SAG/PE bilayer film coils due to the internal

residual stress. ....	120
Figure 6.5 Simulated deforming process of a tempered SAG/PE bilayer film after being released from external constraint. (a) Configuration of an SAG/PE bilayer film after constrained tempering. (b-f) Snapshots of the deforming process of the tempered SAG/PE bilayer after removing the constraint. Parameters adopted in the simulation: $E_{PE}=300$ MPa, $\nu_{PE}=0.46$ , $t_{PE}=10$ $\mu\text{m}$ , $\alpha=4\times 10^{-4}/^{\circ}\text{C}$ , $E_{SAG}^t=20.7$ GPa, $S_{SAG}^t=20.4$ MPa, $E_{SAG}^c=2.2$ GPa, $\nu_{SAG}=0.19$ , $t_{SAG}=0.6$ $\mu\text{m}$ , $\Delta T = 40$ $^{\circ}\text{C}$ . ....	120
Figure 6.6 Forces experienced by the SAG/PE bilayer under constrained heating..	122
Figure 6.7 Curling of SAG/PE bilayer after constrained tempering and releasing ..	124
Figure 6.8 Bending curvature of the SAG/PE bi-material after constrained tempering predicted by theory and simulation. Parameters adopted: $E_{PE}=300$ MPa, $\nu_{PE}=0.46$ , $t_{PE}=10$ $\mu\text{m}$ , $\alpha=4\times 10^{-4}/^{\circ}\text{C}$ , $E_{SAG}^t=20.7$ GPa, $S_{SAG}^t=20.4$ MPa, $E_{SAG}^c=2.2$ GPa, $\nu_{SAG}=0.19$ , $t_{SAG}=0.1-0.6$ $\mu\text{m}$ . ....	127
Figure 6.9 The dependence of $(\Delta T - \Delta T_f)$ on the thickness of SAG layer. Here, $\Delta T$ and $\Delta T_f$ represent the tempering temperature and the critical temperature increment to re-flatten the tempered SAG/PE bilayer, respectively. Parameters adopted in simulation: $E_{PE}=300$ MPa, $\nu_{PE}=0.46$ , $t_{PE}=10$ $\mu\text{m}$ , $\alpha=4\times 10^{-4}/^{\circ}\text{C}$ , $E_{SAG}^t=20.7$ GPa, $S_{SAG}^t=20.4$ MPa, $E_{SAG}^c=2.2$ GPa, $\nu_{SAG}=0.19$ , $t_{SAG}=0.1-0.6$ $\mu\text{m}$ .....	128

## List of Tables

Table 4.1 Characteristic parameters of cohesive elements (COH3D8 in ABAQUS) adopted in the finite element simulations .....	68
Table 5.1 The optimal film thickness for different plane-strain configurations.....	105
Table 6.1 Mechanical properties of SAG layer obtained from MD simulation (Adapted from [181]) .....	118

# **Chapter 1. Introduction**

Bi-materials and structures are widely present in an extensive range of natural and engineering systems due to their ability to take advantage of the merits of the individual constituents and to minimize their weaknesses. As a result, they usually exhibit much superior mechanical performance, e.g., high strength, toughness and/or wear resistance, compared with their monolithic counterparts. However, limitations still exist in bi-materials and structures. Firstly, the interface between the two materials is often much weaker than the bulk constituents, making interfacial crack and subsequent interfacial delamination easy to happen, which would largely reduce the mechanical properties of bi-materials and structures. Another problem is the strain misfit-induced stress concentration on the interface between the two constituents due to their different responses to external stimuli such as temperature and humidity, which tends to evoke crack initiation and propagation. For the development of bi-materials and structures with exceptional mechanical performance, therefore, it would be of great value to solve or mitigate these interface-related problems. On the other hand, the strain misfit between the two materials may not always be detrimental and it can be utilized instead for specific applications of bi-material systems.

## **1.1 Typical bi-materials and structures**

Through billions years of evolution, biological materials are well-known for their high efficiency in conducting a series of functions such as structural support, predation,

protection and mobility, etc., by using small quantities of constituent materials in limited selection. The hard biological tissues like tooth, bone and nacre, are often bi-material composites comprising mineral phase connected with organic materials as shown in Figure 1.1. For the enamel of tooth, it is composed of needle-like mineral crystals embedded in the soft organic matrix [1, 2]. In cortical bone, mineral plates are staggered in collagen matrix to form mineralized collagen fibrils [3-5]. Dentin of tooth, similar to bone, is also composed of protein matrix reinforced by calcium phosphate mineral crystals [1, 6, 7]. The nacre layer of abalone composites the microscopic aragonite tablets and proteins in a well-known brick-and-mortar structure [8-11]. Although with similar constituents, these bi-material systems organize in different manners to satisfy various functional requirements of the organisms.

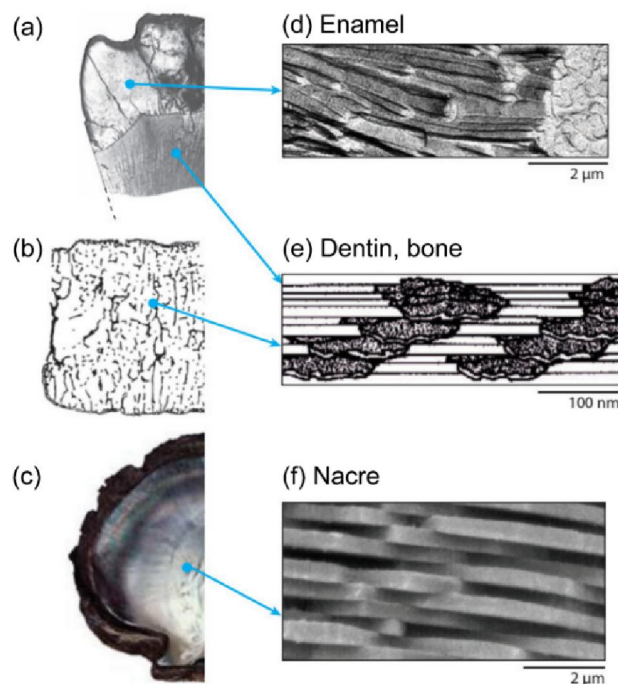


Figure 1.1 Hard biological tissues. (a) tooth, (b) bone, and (c) nacre are bi-material composites with hard-mineral platelets embedded in a soft protein matrix. (d) The

enamel of tooth is composed of needle-like crystals embedded in soft organic matrix. (e) Dentin and cortical bone are made of mineral plates staggered in protein matrix. (f) Nacre is composed of plate crystals with small quantity of soft matrix in between (adapted from [8]).

Since ancient times, mankind have already realized the advantage of combining two or more different materials together, and started the manufacturing of bi-material composites. Before 2000 BC, for instance, ancient Chinese people were found adding grass stems into adobe to manufacture housing wall materials. Nowadays, the bi-material composites have been extensively applied in many fields, such as aerospace, military and auto industry. According to the dimension of the second phase added, bi-material composites can be divided into three categories, i.e., particle reinforced composite, fiber reinforced composite, laminated composite, as schematically shown in Figure 1.2. Numerous studies [12-15] have demonstrated the superior mechanical properties of bi-material composites, such as high stiffness, strength and fracture toughness.

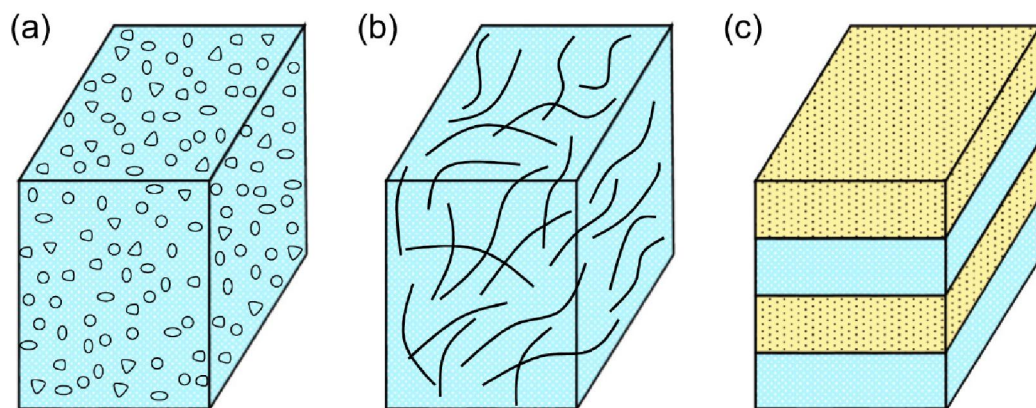


Figure 1.2 Schematic diagram of (a) particle reinforced composite, (b) fiber reinforced composite and (c) laminated composite.

For engineering applications, materials are not only required to possess excellent mechanical properties, but also be capable of surviving in complicated environment, such as high temperature, high wear/friction contact, corrosive atmosphere. To fulfill these requirements, diverse film-substrate bi-material systems were developed. One typical example is the thermal barrier coatings on the gas turbine engines. The surface thin film is required to be inert to chemicals, stable at evaluated temperature and thermal insulated to improve engine efficiency and also extend the service lifetime of substrate material. Another example is the wear-resistant coatings on some components subjected to wear or friction due to contact in service, such as cutting tools, knee plants and internal combustion engines. Furthermore, an anode film-current collector bi-material system is employed in lithium-ion batteries, in which anode film is used for energy storage and supply while current collector works as electrical conductor.

## **1.2 Interface-related problems in bi-materials and structures**

For bi-materials and structures, apart from the individual constituents, the interface between them has great influence on the mechanical performance. This is because the interface could combine the two materials together and transfer loading between them. However, the interface bonding between the two materials is often much weaker than the bulk constituents. As a result, under mechanical loading, crack initiation and propagation are prone to occur at interface, thus leading to interfacial delamination

and early failure of materials. Figure 1.3(a) shows the crack initiation at the particle/matrix interface and microcrack coalescence in particle-reinforced composite material under compressive loading. Figure 1.3(b) shows the fiber/matrix interface delamination in fiber-reinforced composite after flexural testing.

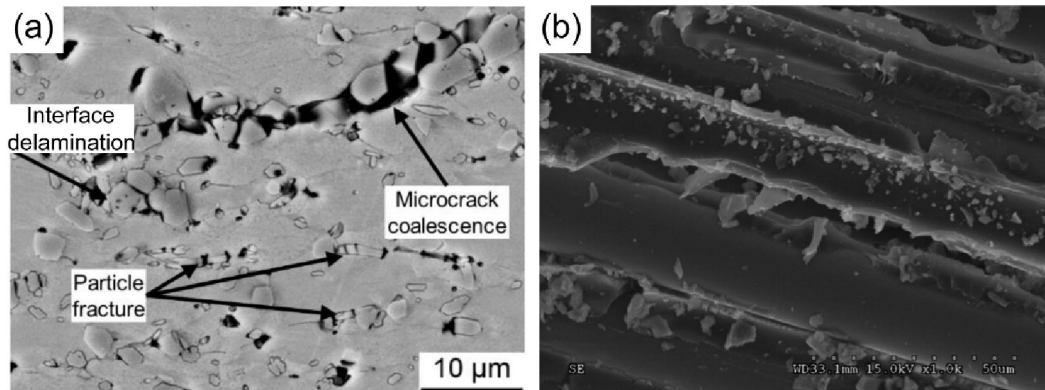


Figure 1.3 (a) Particle/matrix interface delamination and microcrack coalescence observed in particle-reinforced composites under compressive loading (adapted from [16]). (b) Fiber/matrix interface delamination observed in fiber-reinforced composites after flexural testing (adapted from [17]).

Another interface-related problem is stress concentration on the interface of bi-materials and structures. Different from their monolithic counterparts, bi-materials contain two materials with distinct properties. When subjected to change of external environment such as temperature and humidity or variation of internal structures due to, for example, phase transformation, the individual components may exhibit different extents of volume change, resulting in shear stress on the interface between them [18]. Typically, such shear stress does not distribute uniformly over the interface. Instead, high stress concentration exists at the edge of interface [19-21], where interfacial crack is apt to occur, resulting in crack propagation and subsequent

interface delamination. Figure 1.4(a) shows a thermal barrier coating delaminated from substrate after multiple thermal cycles owing to the thermal misfit between the film and substrate [22]. Figure 1.4(b) displays a Si-based anode film in lithium-ion battery detached from current collector after many charge-discharge cycles due to the strain misfit between the electrode film and current collector [23]. Clearly, apart from interfacial delamination, other failure modes including film cracking and film buckling are also involved in these bi-material systems, while this thesis would focus on tackling the problem of strain misfit-induced interfacial failure.

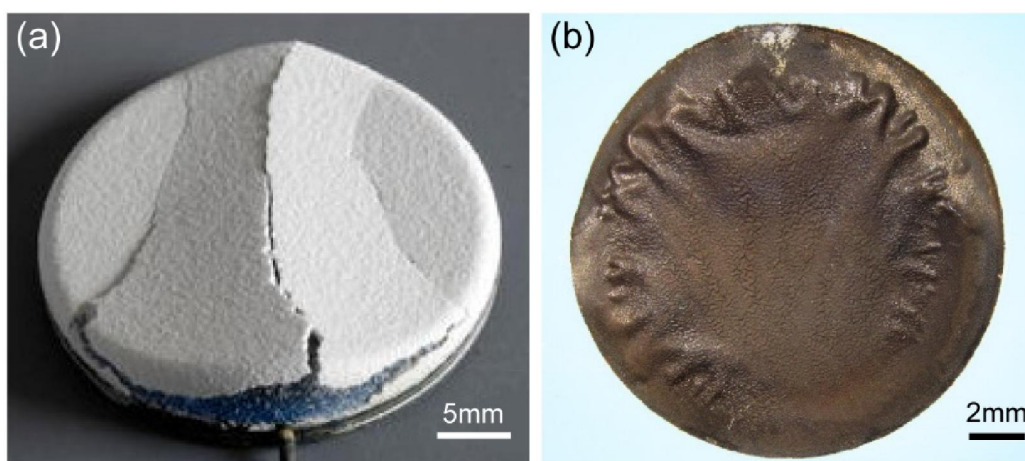


Figure 1.4 (a) Ceramic thermal barrier coating delaminated from superalloy substrate after thermal cycles (adapted from [22]). (b) Si-based electrode film of lithium-ion battery detached from the current collector (copper foil) after lithiation/delithiation cycles.

Numerous studies have been carried out to settle the aforementioned interface-related problems. For example, some delicate interface geometries like suture interface are employed in biomaterials to enhance the crack-propagation resistance and prolong the interfacial crack pathway. Gradient designs at interface

were found effective in mitigating and even eliminating the strain misfit-induced stress concentration on interface. Size reduction is another way found recently to alleviate interfacial stress concentration. These strategies would be introduced thoroughly in Chapter 2.

### **1.3 Objectives and outline of this thesis**

The objective of this thesis is to explore strategies to settle or mitigate the interface-related problems in bi-materials and structures, so as to provide guidelines for the design of bi-material systems with desirable mechanical performance. In Chapter 2, I firstly reviewed the existing strategies employed in natural and engineering materials to tackle these interface-related problems, including strategies to increase the mechanical properties of bi-materials and structures, and strategies to reduce the interfacial stress concentration in bi-materials systems. In addition, recent studies on the controllable deformation achieved in bi-materials by taking advantage of strain misfit were also introduced. Then in Chapter 3, the experimental method to evaluate the wear resistance of materials was presented, followed by fundamental reviews of elastic mechanics, fracture mechanics and finite element method. Subsequently, a spiral architecture called microscopic screw dislocation ( $\mu$ -SD) found in natural materials was studied in Chapter 4. Both scratching test and finite element simulation were carried out to reveal its reinforcing mechanism, and then its working condition was determined by fracture mechanics-based modelling. In Chapter 5, I

proposed to suppress the shear stress concentration on the interface of film-substrate bi-materials by adopting films with gradient thickness. This strategy is illustrated through two typical examples of bi-material including a continuous film bonded on a disk-like substrate and a discrete island film on a half-space substrate. For each case, theoretical solution to the optimal gradient film thickness is obtained, followed by computational and experimental validations. In Chapter 6, the strain misfit-induced morphing behavior of stacked assembly of graphene (SAG)/polyethylene (PE) bi-material was studied systematically. Theoretical modelling demonstrated that controllable morphing behavior can be achieved in SAG /PE bilayer, which was further validated by finite element simulation. Finally, in Chapter 7, the results of this thesis were concluded and discussed, followed by an outlook to the future work.

## **Chapter 2. Research background and literature review**

Due to the exceptional mechanical performance over monolithic counterparts, bi-materials and structures can find applications in many diverse fields. Nevertheless, interface-related issues, including low interface strength and interfacial stress concentration induced by strain misfit, still exist and impair their reliability and service lifetime. Bi-materials and structures in nature may be confronted with similar problems, while they always boast outstanding mechanical properties via delicate structures and designs to adapt to the cruel natural environment. For example, mollusk shells [24], with minerals taking up more than 95 vol. %, are expected to be fragile, yet they exhibit high toughness and damage tolerance. Specifically, nacre in mollusk shells is 3000 times tougher than the mineral component in terms of energy [25]. Over the years, therefore, a great deal of effort has been spent on investigating the strategies employed in natural materials for the development of high-performance engineering materials via biomimetic design. On the other hand, the strain misfit in bi-material systems is not always detrimental and can be exploited instead. Diverse controllable deformations have been realized by taking advantage of the strain misfit in bi-material systems.

### **2.1 Strategies to increase mechanical properties of bi-materials and structures**

In bi-materials and structures, weak interface would lead to early crack initiation

and propagation, and consequently reduced mechanical properties. Then how to increase the mechanical properties of bi-materials with such weak interface becomes a problem. Abundant studies demonstrate that, delicate structures developed in biomaterials, such as suture structure, brick and mortar structure, could effectively amplify the mechanical properties of bi-materials. Multiple toughening mechanisms may be involved, including crack deflection, crack blunting/branching and crack bridging etc., which are largely dependent on the weak interfaces.

### **2.1.1 Suture structure**

Suture structures are wavy or interlocking interfaces consisting of rigid teeth and compliant interfaces, as schematically shown in Figure 2.1(a). In biological materials, they can be broadly observed in regions where the intrinsic strength and flexibility of material interface need to be controlled. Figure 2.1(b-h) show some typical examples of suture structures found in organisms, which exhibit diverse geometries and complexities among different species. Numerous studies have been conducted to investigate the impact of geometric features of suture structure on its mechanical properties, so as to provide guidelines for the biomimetic design of bi-materials and structures reinforced by suture interface.

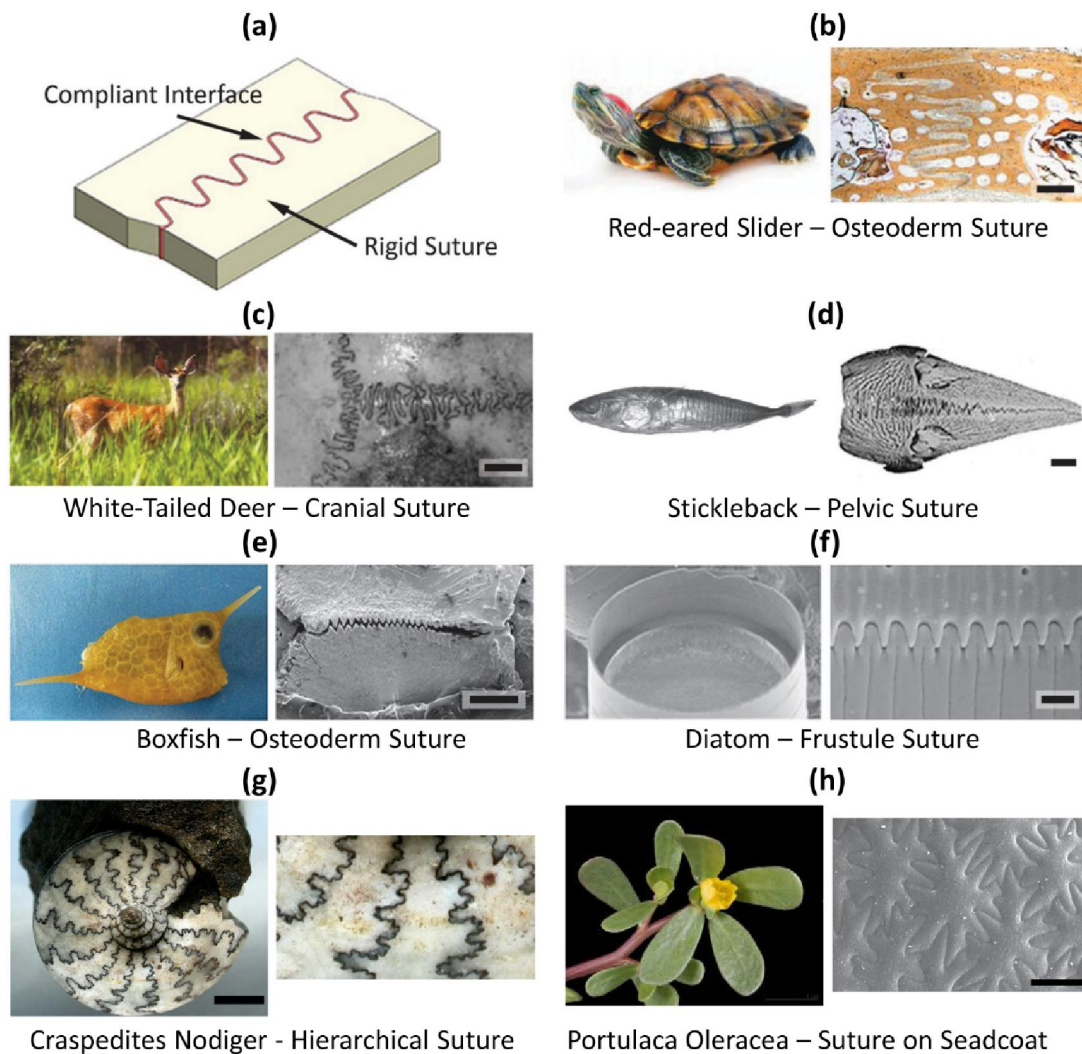


Figure 2.1 Biological suture structures in nature. (a) Diagram of suture structure consisting of rigid teeth and compliant interface; (b) Osteoderm sutures in red-eared slider; (c) Cranial sutures in white-tailed deer; (d) Pelvic sutures in stickleback; (e) Scute sutures in boxfish; (f) Exoskeletal sutures in diatom; (g) Hierarchical sutures in *Craspedites nodiger*; (h) Suture on the seedcoat of *Portulaca oleracea*. Scale bars: (b) 1 mm, (c) 1 cm, (d) 1 mm, (e) 500  $\mu\text{m}$ , (f) 1  $\mu\text{m}$ , (g) 1 cm, (h) 50  $\mu\text{m}$ . ((a-f) adapted from [26], (g) adapted from [27], (h) adapted from [28])

Li and coworkers [29] established theoretical models to predict the strength of suture structure with arbitrary geometry. Here, the most generalized case, periodic suture joints with triangular teeth, was taken for illustration. For such a structure under tension normal to suture seam, two failure modes, i.e., teeth breakage and

interface failure, may take place depending on the combination of component strengths as well as suture geometries. For given component strengths, there is a critical suture tooth angle  $2\theta_0$ , with which the tooth skeleton and interface layer would fail simultaneously, thus resulting in an optimized strength [29]:

$$2\theta_0 = \sin^{-1} \frac{2\tau_0^f}{\sigma_1^f}, \quad \theta_0 \leq \frac{\pi}{4}$$

in which  $\tau_0^f$  denotes the shear strength of interface layer, and  $\sigma_1^f$  denotes the tensile strength of tooth skeleton. This relationship is plotted in Figure 2.2 displaying the boundary of the two failure modes. Clearly, with  $2\theta < 2\theta_0$  tooth failure would happen, while with  $2\theta > 2\theta_0$ , interfacial failure would take place. The transition of failure mode from tooth breakage to interfacial failure was observed in their subsequent experimental studies [30]. Meanwhile, the effective stiffness of a sutured structure ( $\bar{E}$ ) can be expressed in terms of mechanical and geometric parameters as [29]:

$$\frac{\bar{E}}{E_1} = \frac{f_v^2}{(1-f_v) \left( \frac{E_1}{G_0} \sin^2 \theta \cos^2 \theta + \frac{E_1}{E_0} \sin^4 \theta \right) + f_v}$$

where  $E_1$  and  $E_0$  denote the elastic moduli of suture skeleton and interface phase respectively,  $G_0$  is the shear modulus of interface phase, and  $f_v$  is skeletal volume fraction. Although these results are obtained based on idealized assumption, we could get basic understanding of optimized geometry in suture structure. Subsequently,

their theoretical model was further extended by taking more factors into consideration, including arbitrary geometry and arbitrary in-plane loading [31], bonded tip interfacial layer [32], and aligned fiber embedded connective layer [33], to provide insights for the correlation between mechanical properties and geometrical features of suture structure.

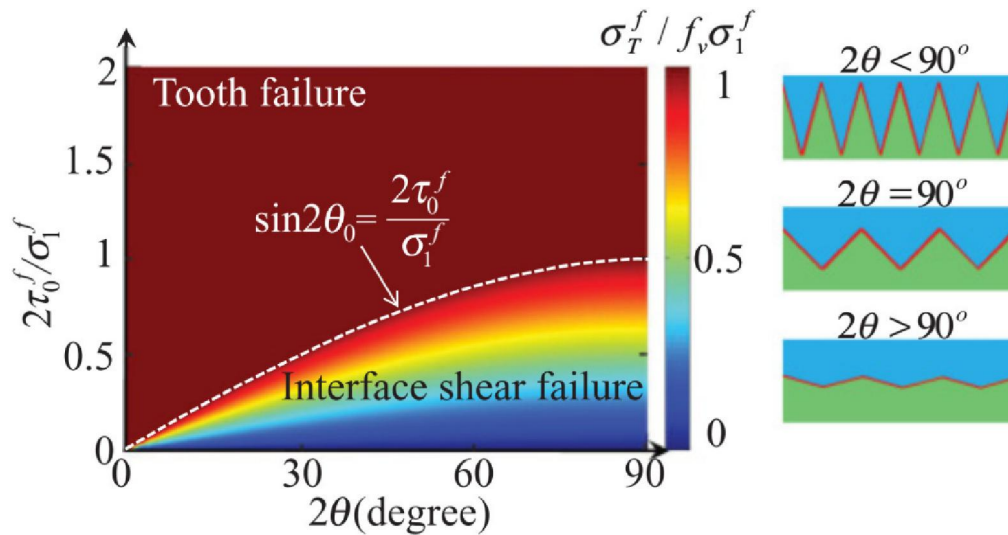


Figure 2.2 Contour of the normalized strength of suture structure as a function of the component strengths and suture tooth angle. (Adapted from [29])

Meanwhile, Barthelat and coworkers [34-36] systematically studied the mechanical behaviors of interlocking sutures during pullout process through a combination of theoretical modelling, FE simulation and experimental tests. Firstly, they [34] examined the pullout response of jigsaw-like suture structure and concluded that the optimal pullout performance, i.e., high strength as well as high energy absorption, can be achieved via the combination of low friction coefficient at interface and high interlocking angles. Based on jigsaw-like morphologies, they [36]

further developed a bi-stable structure which could achieve geometrical lock at two distinct stable positions (see Figure 2.3), and the second equilibrium position was found effective providing a geometric hardening mechanism. As a result, the bi-stable structure is 10 times tougher than the constituent material. Subsequently, a suture structure with additional geometrical features including plateau regions and multiple locking sites was further investigated theoretically and computationally [35]. It was found that low frictional stress at interface, by either low friction coefficient or multiple locking sites, could contribute to an optimal combination of strength and energy consumption.

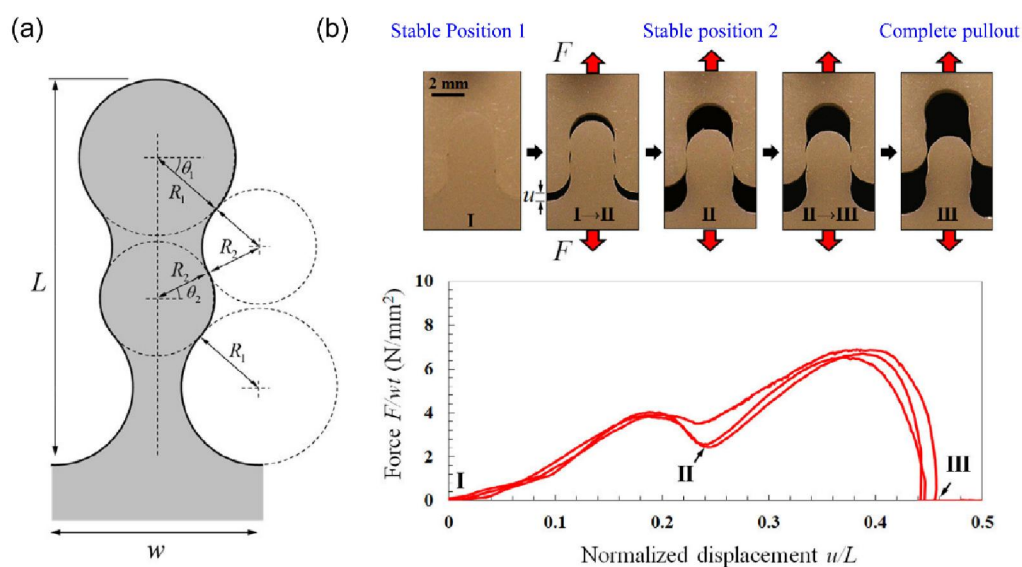


Figure 2.3 Overview of the design of bi-stable interlocked tabs. (a) The schematic diagram showing the profile of the tab; (b) Pullout process of the bi-stable interlocked tabs. During this process, there are two stable positions in this system, which would result in more energy consumption. (Adapted from [36])

Besides a single repeating wave, suture structures with hierarchical multiple wavelength patterns can also be observed, for instance, in the cranium of white tailed

deer [37] and in the shells of ammonites [38-41], as displayed in Figure 2.1(g). Recently, Li et al. [27] developed an analytical model to investigate the impact of structural hierarchy on the mechanical performance of suture joints quantitatively. Results show that the mechanical properties, e.g., stiffness, strength and fracture toughness, can be amplified nonlinearly over a wide range of amplitude by varying the order of structure hierarchy. Subsequently, they further examined the role of hierarchy through experiments on 3D printed prototypes [42]. It was found that the stiffness of suture structure can be amplified by more than one order of magnitude by increasing the order of hierarchy, and tensile strength can be tuned via hierarchy as well. For higher order hierarchical structures, a graceful failure, i.e., significant interfacial failure and minor teeth breakage before destructive structure failure, could increase the fracture toughness. Such dependence of fracture toughness of suture structures on hierarchy was also disclosed by Li et al. [43] and Zheng et al. [44] via simulation.

Up to now, most studies are focused on the role of suture complexity on the mechanical behaviors, while the effect of suture irregularity attracts little attention. In fact, irregular suture structures can be widely observed in nature, like cranial suture of vertebrate skulls [45-47] (see Figure 2.1(c)), the pelvic suture of armored fish [48], sutures on the carapace of the turtle [49] (see Figure 2.1(b)) and the microscale sutures in the beak of woodpeckers [50]. Recently, Li and coworkers [51] studied the role of suture irregularity on the mechanical behaviors through a combination of

theoretical modelling and FE simulation. Results show that, with the increase of morphological irregularity, the failure strain would increase without sacrificing tensile stiffness, and the fracture energy would increase with a reduced strength to damage initiation. Thus, the morphological irregularity is another important factor governing the mechanical behaviors of suture structure.

Generally, the wave amplitude of suture structure in animal species is much smaller than the size of each tile [52], while much magnified suture amplitude can be observed in plants. As shown in Figure 2.1(h), the seed coats of *Portulaca oleracea* are composed of star-like epidermal cells connecting via suture interface with wave amplitude comparable to the size of constituent tiles. Gao et al. [52] studied the impact of these wavy tessellations with amplitude close to the scale of the building blocks via FE simulation and experimental tests. The waviness of suture interface was found playing an essential role in governing the mechanical responses. Generally, higher suture waviness could contribute to more efficient loading transfer between the hard constituent tiles, thus the overall strength and fracture toughness would be improved. Such impact of waviness can be amplified with higher stiffness ratio between the hard tiles and soft interface.

Due to the exceptional capability in toughening brittle constituents, many researchers attempted to implement interlocking suture interface into brittle material systems for amplifying toughness. For example, Mirkhalaf et al. [53] introduced

suture interface into glass by engraving microcracks which were then infiltrated with polyurethane. In mechanical tests, the weak interface could direct cracks into interlocking configurations and evoke pullout mechanisms, thus resulting in significant enhancement in energy dissipation and toughness. Such glass with suture interface was reported 200 times tougher than intact counterpart [53]. Significant improvement in fracture toughness was also realized in ceramic plates engraved with suture interface via non-linear deformations associated with geometric hardening and frictional pullout [54].

### **2.1.2 Brick and mortar structure**

Nacre, the inner layer of mollusk shells, composites 95 vol.% microscopic aragonite tablets and 5 vol.% protein-rich organics through a delicate brick and mortar structure (see Figure 1.1(c)). The aragonite ‘brick’ is 0.2-0.9  $\mu\text{m}$  in thickness [55] and 2-10  $\mu\text{m}$  in diameter [10], while the thickness of organic ‘mortar’ is in the range of 20-30 nm [55-57]. In three- and four-point bending tests, nacre exhibits 20-30 times higher fracture toughness than pure aragonite, which is intriguing considering the high volume fraction and brittleness of aragonite phase in it. Therefore, enormous studies have been performed to disclose the underlying reinforcing mechanisms. A great number of reinforcing mechanisms at different length scales are proposed, which can be summarized as follows [10]: a) crack blunting and branching [58, 59]; b) tablets pullout [25, 59-62]; c) the nucleation and

coalescence of micro cracks around crack tip [61, 63, 64]; d) bridging effect of organic phase [25, 62, 65]; e) the hierarchical unfolding of biological macromolecules and viscoplastic energy dissipation around crack tip [61, 63, 66]; and f) various strengthening mechanisms on the interface of neighboring layers [55, 57, 62, 63, 67-69], etc. Figure 2.4 schematically displays some experimentally-identified toughening mechanisms around a propagating crack tip in nacre. Among them, the platelets bridging between crack surfaces is considered to be the most significant one accounting for nacre's exceptional fracture toughness [25]. The energy dissipation in the bridging zone hinges on factors like geometric parameters of platelets, mechanical properties of both mineral and organic phases, and the distribution of the mineral platelets, etc. [10]. Therefore, it is of great significance to find out the correlation between the aforementioned micro physical features and toughening effect, so as to provide guidelines for the manufacture of nacreous materials.

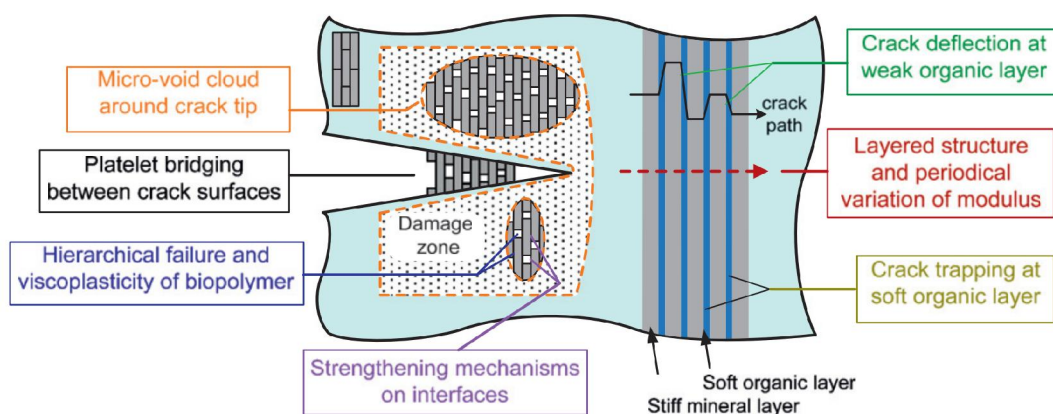


Figure 2.4 Schematic of some toughening mechanisms around a propagating crack tip in nacre. (Adapted from [10])

In the year of 2003, Gao and coworkers [9] investigated the impact of the size of mineral phases on the fracture toughness of biomaterials through a tension-shear chain model. It was found that, when the mineral tablets are downsized to nanoscale, they would become flaw-tolerant with strength approaching the theoretical atomic bonding. Mineral tablets with optimal strength could allow large amount of energy dissipation in protein layers via shear deformation, thus leading to high fracture toughness of bio-composites. Such kind of improvement can be further amplified via the viscoelastic properties of organic layer. Afterwards, a fracture mechanics model based on nacreous microstructure was further established to investigate the toughening effect of mineral crystals [10], and similar size effect of mineral platelets on the fracture toughness was also identified. Specifically, for a greater fracture toughness, the thickness of platelets is required less than one micron but not smaller than tens nanometers to avoid breakage during pullout. In addition, higher strength and energy dissipation in organic layer can also contribute to higher toughness of such bi-material composites.

More recently, Ni et al. [70] investigated the dependence of mechanical performance of nacreous nanocomposites on the constituent properties and arrangements via a nonlinear shear-lag model. Both the elasto-plasticity of the organic layer and the overlapping length of mineral tablets were found having significant impact on the failure path. A parameter selection guideline in terms of two characteristic lengths was provided for the optimal combination of strength and

toughness of the nacre-like composites [70]. Likewise, Begley et al. [71] investigated the uniaxial responses of brick-and-mortar structured composites through micromechanical models. The critical stresses for the rupture of brick and mortar were given as a function of constituent properties and geometries, illustrating trade-offs between stiffness, strength and dissipated work, thus proving guidelines for the development of nacreous composites.

In different shell species, nacreous tablets are arranged in different degrees of randomness. For example, in the shell of *Haliotis Rufescens* and *Trochus Niloticus* and other gastropods, the tablets are stacked in columns across the layers, called as columnar nacre [24]; while for sheet nacre in bivalve species such as oysters or mussels, the arrangement of the tablets is more random [63]. Barthelat and coworkers [72] investigated the effects of random variations in microstructures via both representative volume element (RVE) models and large scale statistical volume element (SVE) models. It was revealed that statistical variations have negative effect on the ductility and energy absorption of nacreous composites, since randomness would facilitate deformation localization. However, such negative effect may vanish when the interfaces have large failure strain as well as strain hardening.

At the platelet-platelet interfaces, there are periodical arrays of nanoscale mineral bridges scattered in the soft organic phase [58, 73], as shown in Figure 2.5(a-b). For different mollusk shell species, interestingly, the diameters of these mineral bridges

were all reported in the range of 10-50 nm [57, 67, 74-76]. To account for this characteristic size, Shao et al. [77] studied the size effect of mineral bridges on the interfacial shear strength. It was found that the optimal strength of interface can be realized only when the diameter of mineral bridges is of tens of nanometers. On the other hand, Kalpana et al. [78, 79] discovered the existence of interlocks between platelets in nacre of abalone (see Figure 2.5(c-d)) and revealed its key role on the high toughness of nacre through FE simulation.

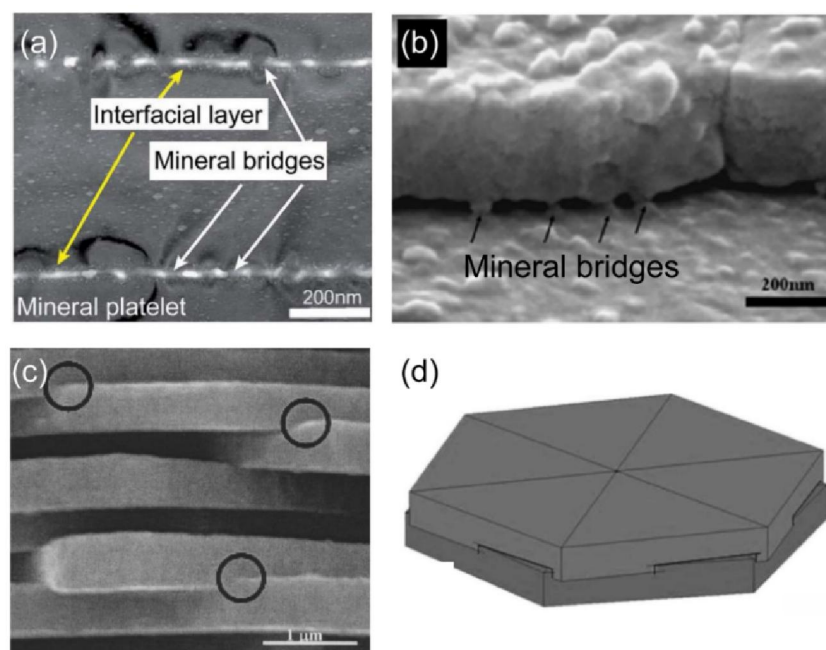


Figure 2.5 (a) STEM and (b) TEM image showing the mineral bridges at the platelet-platelet interface in nacre. ((a) adapted from [77], (b) adapted from [80]) (c) SEM image showing the interlocks between the platelets in nacre; (d) Schematic illustration showing the interlocks between the platelets in nacre. ((c, d) adapted from [78])

Due to the extraordinary mechanical performance of nacre, enormous efforts have been devoted to manufacturing nacre-like structures [80]. For example,

Bouville et al. [81] fabricated layered ceramic materials with submicrometer layer spacings via ice templating, as shown in Figure 2.6(d-f). Compared with natural nacre (see Figure 2.6(a-c)), the packing of platelets shows short-range order while not perfect long-range order (see Figure 2.6(d)). The spacing between the platelets is filled with liquid second phase (see Figure 2.6(e)) containing inorganic bridges and nano-asperities (see Figure 2.6(f)), mimicking the organic layer in nacre. As a result, the nacre-like material possesses a unique combination of high stiffness, high strength and high toughness. Furthermore, their mechanical properties can be retained at high temperature as no organic phase is involved.

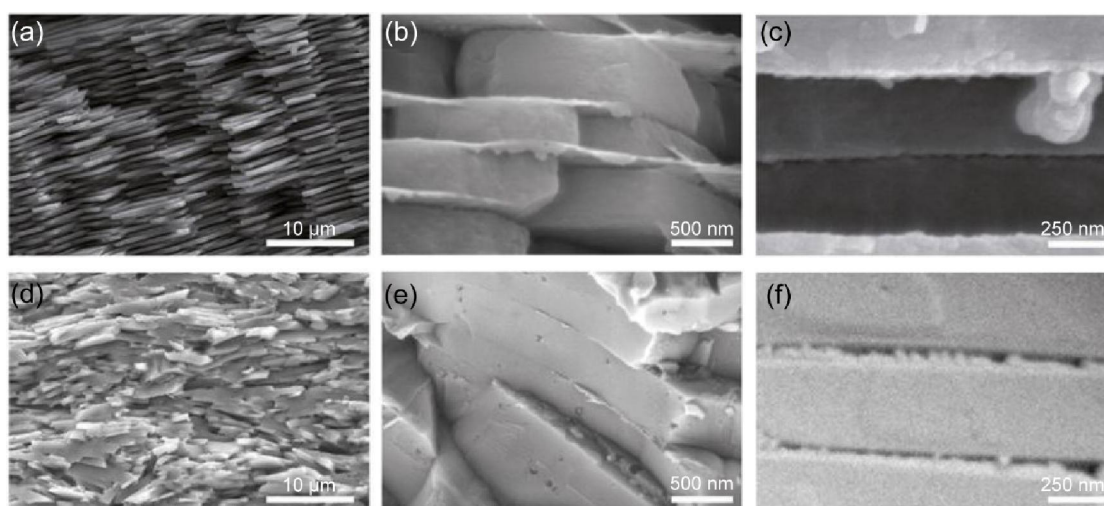


Figure 2.6 Comparison of microstructures of (a-c) natural nacre and (d-f) nacre-like alumina. (a, d) SEM images showing the short and long-range orders of platelets. (b, e) Local stacking of platelets. Liquid phases is presented in (e) mimicking the protein layer in nacre. (c, f) Closer views of the platelet interface. Inorganic bridges and nano-asperities can be observed at the platelets interface in (f). (Adapted from [81])

More recently, Barthelat and coworkers [82] duplicated the three dimensional brick-and-mortar structure with engraved glass sheets and polymeric interlayers (see

Figure 2.7). In their nacre-like glass, good light transmittance was still retained. In addition, tablet sliding mechanism, which enables nonlinear deformation thus increasing toughness, was also reproduced in their material. Compared with laminated glass and tempered glass, their glass with nacreous structure shows two to three times impact resistance while keeping high stiffness and strength.

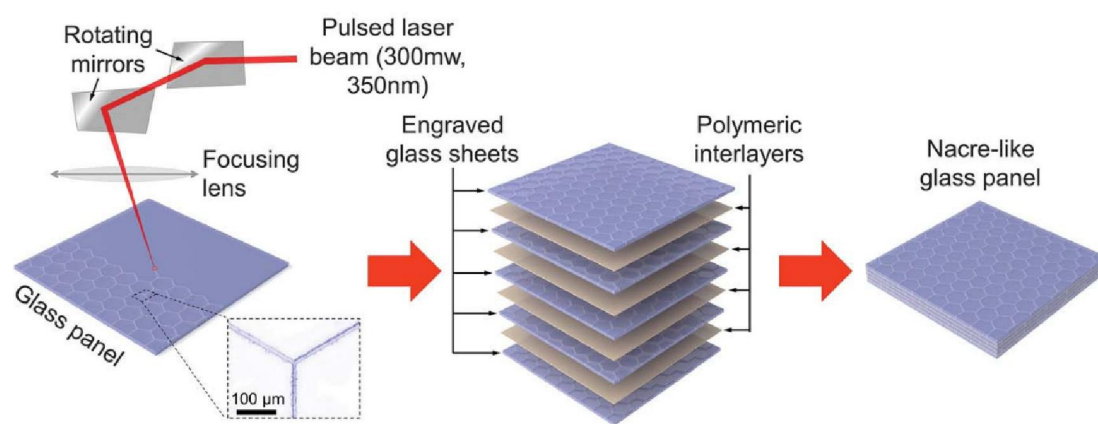


Figure 2.7 Fabrication protocol for nacre-like glass panels. (Adapted from [82])

Although considerable attempts have been made to duplicate the brick and mortar structure in nacre, few of them can simultaneously mimic all the features that are responsible for the reinforcement in natural nacre due to structural complexity. As a result, the duplicated nacre-like structure exhibits higher mechanical properties, e.g., fracture toughness, than monolithic counterparts, while such improvement is far from the achievement in natural nacre.

## 2.2 Strategies to reduce stress concentration on interface

Stress concentration on the interface between the two materials is another important issue to be settled for the development of bi-materials with outstanding

mechanical performance. Abundant studies have been performed to seek solutions from natural materials, and some strategies have been developed to mitigate or eliminate the stress concentration on the interface in bi-materials and structures.

### 2.2.1 Shape optimization

The adhesion between two contacting surfaces have received lots of attention. In the year of 2003, Gao and Yao [83] studied the adhesion between a rigid fiber and an elastic substrate via van der Waals (see Figure 2.8(a)). For such a system, the optimal adhesion force is  $\sigma_{th}A$ , with  $\sigma_{th}$  and  $A$  denoting the theoretical adhesion strength and contact area, respectively. However, such optimal adhesion may be hard to achieve due to the shape sensitivity-induced stress concentration at the interface edge (see Figure 2.8(b)). They demonstrated that the theoretical pull-off force can be obtained when the shape of the fiber tip is precisely optimized so that a uniform adhesive stress can be realized as displayed in Figure 2.8(c-d). Subsequently, they [84] further extended their study to the adhesive bonding between two elastic solids.

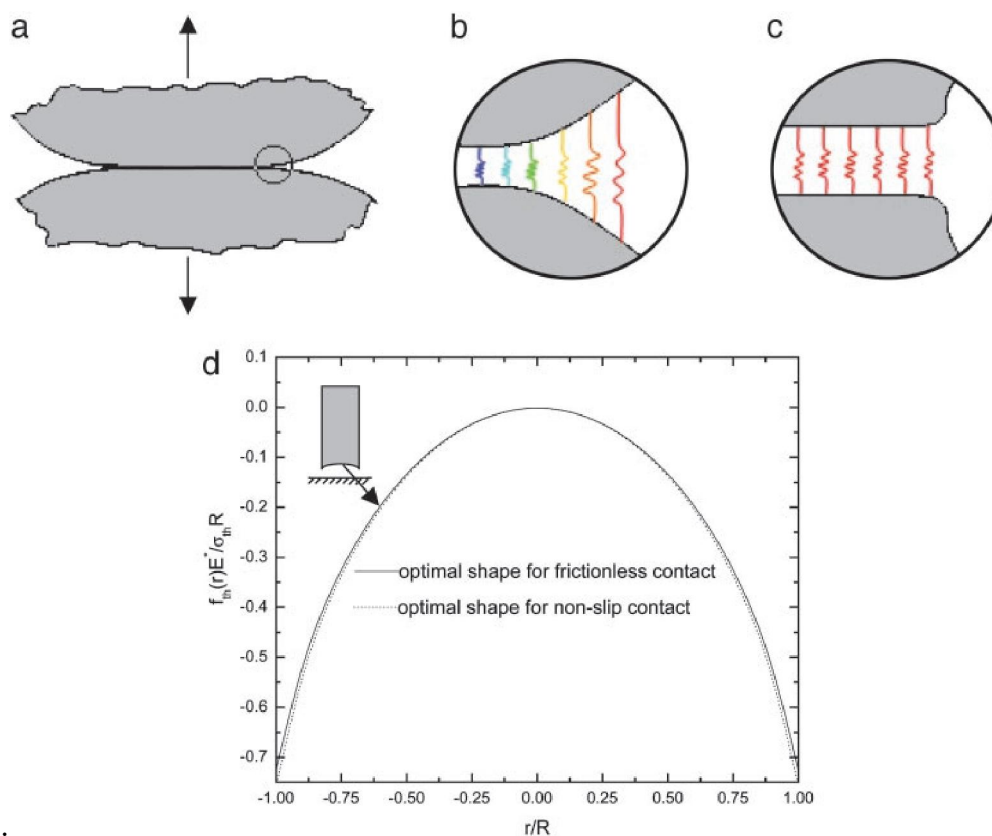


Figure 2.8 (a) Two structures are bonded together and subject to an external load. (b) Stress concentration occurs at interface edge. The spring represents the molecular interaction forces between the contacting surfaces. (c) Uniform tensile stress distribution at interface. (d) The optimal shape profile of a rigid fiber tip for a uniform tensile stress distribution. (Adapted from [83])

Since Gao and Yao's work, a number of studies [85-90] have been conducted to investigate the influence of tip shape in fibers on adhesive stress distribution so as to maximize the adhesion force. For instance, Campo et al. [88] manufactured various PDMS surfaces patterned with micro pillars of different shapes as displayed in Figure 2.9(a-f) and tested their adhesion performance. It was found that the highest adhesion can be realized in mushroom-like terminals with adhesion forces 30 times higher than the flat controls (see Figure 2.9(g)). This can be attributed to, as revealed

by their subsequent numerical analysis [89], the reduced corner stress singularity on the contact interface of mushroom fibrils. Since then, quite a few efforts have been made to seek the optimal geometrical design of the mushroom-like fibrils based on different geometrical models (see Figure 2.10). For example, Balijepalli et al. [89] found that the corner stress singularity on the contact interface can be minimized by small cap thickness and small fibril stalk diameter (see Figure 2.10(a)). Aksak et al. [85] conducted a series of numerical simulations and attained the optimal parameter combinations for maximum pull-off stress: the ratio of the tip radius to the stalk radius equal to 1.1, and the edge angle equal to  $45^\circ$  (see Figure 2.10(b)). Carbone et al. [90] found the best adhesive performance can be achieved when the ratio of the cap thickness and stalk radius is close to 0.2-0.3, and the ratio of the tip radius to the stalk radius is larger than 2 (see Figure 2.10(c)).

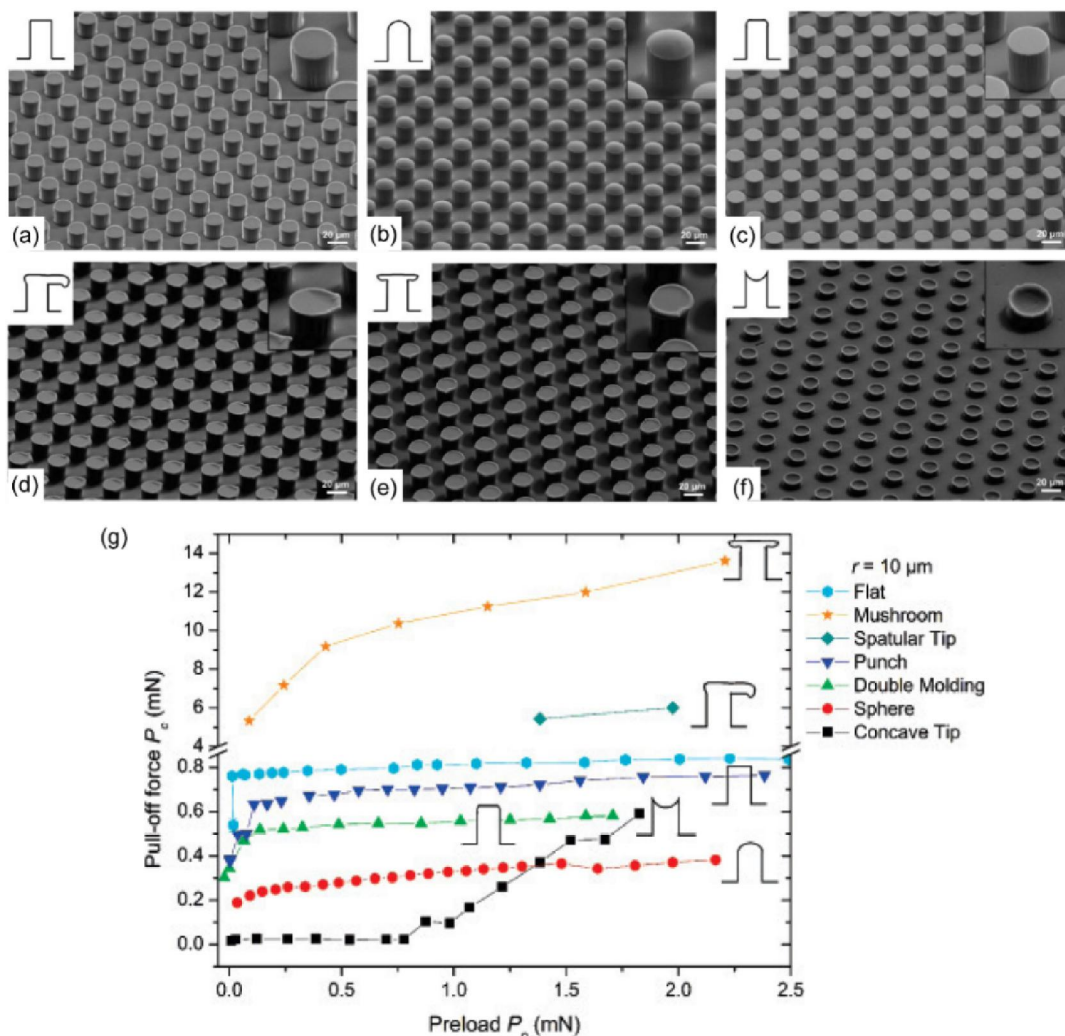


Figure 2.9 SEM images of fibrillar PDMS surfaces with different tip shapes: (a) flat, (b) spherical, (c) flat with rounded edges, (d) spatula, (e) mushroom, (g) concave tips. (f) Comparison of pull-off force for different tip shapes under different preloads. (Adapted from [88]).

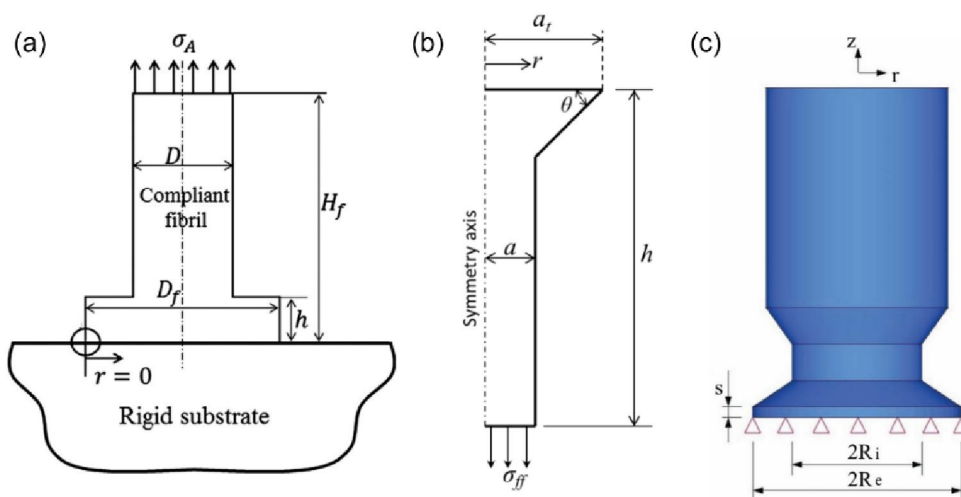


Figure 2.10 Different geometrical models for fibers with mushroom tip. ((a) adapted from [89], (b) adapted from [85], (c) adapted from [90])

### 2.2.2 Size reduction

Size reduction can be another alternative approach to reduce stress concentration on interface. It is interesting to find that natural materials with exceptional mechanical properties, such as bone, teeth and mollusk shells, are all nanocomposites of proteins and minerals. Apart from the manner they are organized, nanometer scale was also found playing an essential role [8] in determining the mechanical behaviors. Gao and coworkers [8] studied the size effect of mineral phase on fracture strength, and disclosed that, when the size of the mineral phase is above a critical length scale (around 30 nm), the material is sensitive to crack-like flaws and would fail by stress concentration at crack tip; while downsized below this value, the mineral would become flaw-tolerant and stress concentration could be evaded with strength approaching its theoretical value. Although this study deals with the stress concentration at the crack tip in a monolithic material, the strategy of size reduction can be extended to bi-materials and structures. For instance, for the anode film-current collector bi-material system in lithium-ion batteries, shear stress concentration would take place on the interface during charge-discharge process, due to the volume variation-induced strain misfit between them. As a result, the anode film would detach from current collector after many charge-discharge cycles (see Figure 1.4(b)). Gao and coworkers [91] downsized the anode film by depositing

patterned silicon islands on the current collector, and found that they would not detach from current collector during charge-discharge cycling if the size is reduced to below a critical value around 7–10  $\mu\text{m}$ .

Similar size effect was also found in adhesion mediated by intermolecular interactions between two contacting surfaces [83, 92]. As mentioned in Subsection 2.2.1, there is an optimal shape for the fiber tip, with which the adhesive stress would be homogeneously distributed along the contact interface at pull-off thus maximizing the pull-off force [83]. However, when the fiber diameter is dropped to the length scale on the order of 100 nm, the adhesion is not sensitive to the tip shape anymore. Even with flat shape on the fiber tip, the adhesive stress can be almost uniformly distributed with adhesion force approaching the theoretical value [83]. This could also account for the ubiquitous hairy attachment systems in biology.

### **2.2.3 Gradient design**

Gradient variation in mechanical properties in either continuous or step-wise manner can be widely found in biological materials. Specific examples include dental-enamel junction (DEJ) in human teeth (see Figure 2.11(a)), and gradient between the hard exterior and tough interior of fish scales (see Figure 2.11(b)). Recent studies on natural biomaterials revealed that gradient interlayers in natural composites play an important role in strengthening the interfaces between distinct materials [93-95].

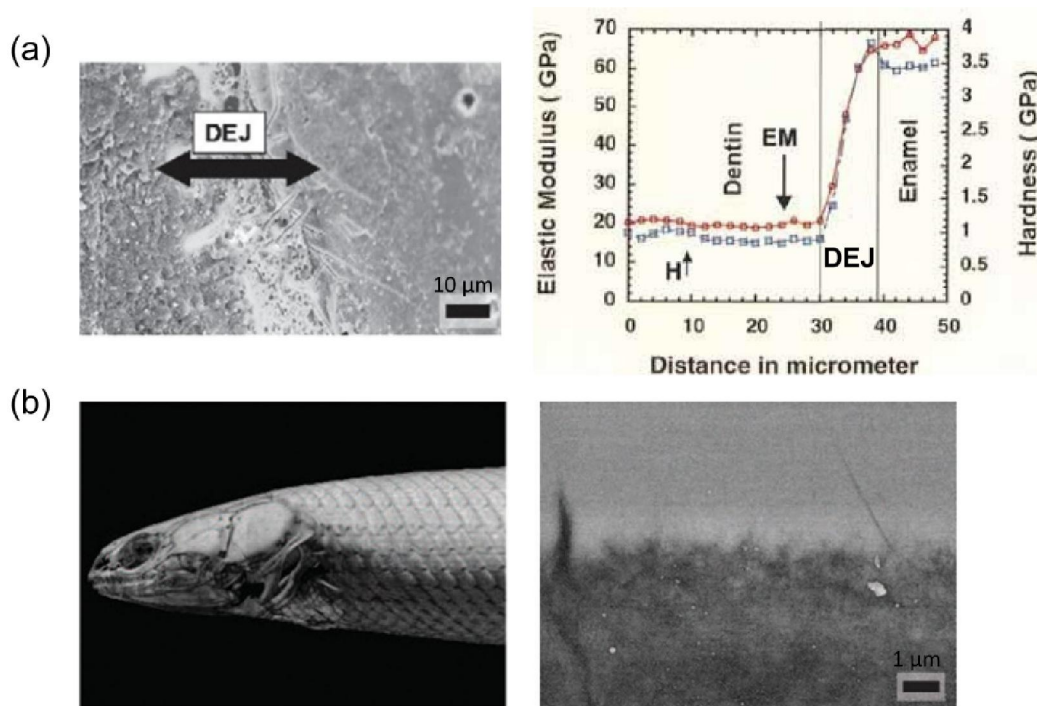


Figure 2.11 (a) Dental-enamel junction (DEJ) of human teeth (Adapted from [26]), and gradient elastic modulus and hardness at DEJ (Adapted from [96]). (b) Fish with gradient scales (Adapted from [26]).

Learning from nature, many material scientists have devoted themselves to the study of functionally graded materials (FGM) for an enhanced mechanical performance. In the year of 1994, Lee et al. [97] conducted a theoretical analysis and revealed that by moderating the transition slope of mechanical property across the interface between coating and substrate, FGM could effectively mitigate the stress concentration on the interface. Recently, Wang et al. [98] fabricated thermal barrier coatings with gradual variation in composition along thickness direction to alleviate the thermal stress-induced interface delamination. Thermal cycling tests show that the functionally graded coating has extended lifetime compared with non-graded counterparts. In addition, to suppress the interface delamination between the anode

material and current collector in lithium-ion batteries, Guo et al. [23] introduced graded Si distribution along thickness direction into the electrode film as shown in Figure 2.12(a). After 500 discharge-charge cycles, the graded electrode film remains firmly attached on current collector without any detachment (see Figure 2.12(c)), as opposed to serious interface delamination occurred in the homogeneous counterpart (see Figure 2.12(b, d)).

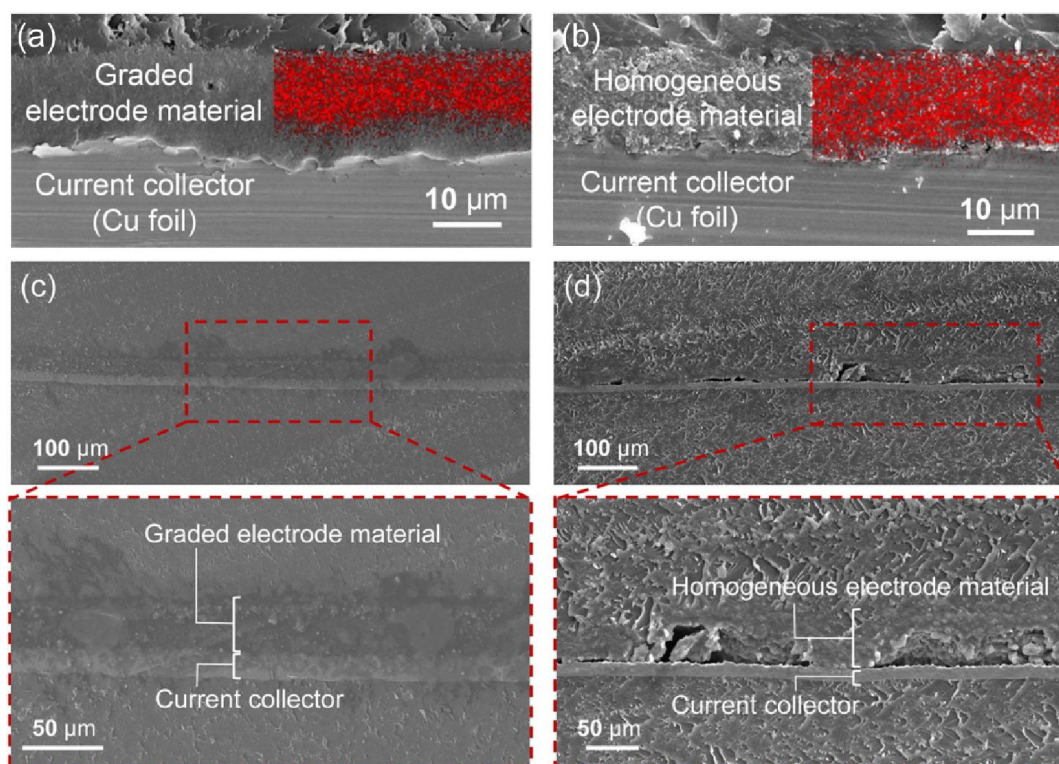


Figure 2.12 EDS mapping of Si element for (a) gradient and (b) homogeneous Si-based anodes. Cross-section of (c) gradient and (d) homogeneous Si-based anodes after 500 discharge-charge cycles. (Adapted from [23])

FGM could also enhance the resistance of protective coatings to contact damages [99]. For example, with Young's modulus increasing by 50% from contact surface to 2 mm depth, the glass-infiltrated alumina becomes far more resistant to sliding

contact damages than homogeneous counterparts due to the reduced principal tensile stresses [99]. Similar enhancement was also found in other material systems, such as glass-infiltrated silicon nitride materials [100], stainless steel [101]. In addition, under normal indentation, gradient elastic modulus in materials such as glass-infiltrated alumina composite, could suppress the formation of cone cracks, as opposed to the formation of cone-crack in bulk glass and alumina [102]. Apart from graded elasticity, the effects of graded plasticity, i.e., yield strength, on the frictional sliding behaviors [103] were also examined through parametric FE analysis. It was suggested that, plasticity-graded materials with improving yield strength below the surface have superior resistance to the onset of plasticity and damages.

Gradient elasticity has also been found on some attachment systems in biology, such as tarsal setae of the ladybird beetle [104]. Yao and Gao [95] reported that materials with designed gradient in elasticity could homogenize the distribution of adhesion stress between two materials and therefore enhance the adhesion strength. Recently, Balijepalli et al. [105] fabricated a fibril comprising a soft tip layer and a stiffer stalk, that is, a fibril with 2-step gradient modulus. Tensile tests [105] show that such gradient structure could reduce the adhesion stress singularity at the interface edge and then realize higher adhesion strength.

## **2.3 Controllable deformation of bi-materials by utilizing strain misfit**

Generally, strain misfit is considered detrimental to bi-material systems since it will cause stress concentration on interface and even interfacial failure. However, strain misfit is not always detrimental and can be beneficial as well. Apart from interface delamination, strain misfit can lead to deformations such as bending and buckling depending on the bi-material dimensions and properties. Such deformations are of a wide range of interest for applications.

### **2.3.1 Bending behaviors of bi-materials**

For bi-materials under strain mismatch, the resulting shear stress on the interface would produce bending moments, making the flat bilayer to curl. Such bi-material systems can be found in many plants to respond to external stimuli like temperature, humidity. For example, the spirally arranged stems of *Selaginella lepidophylla* would curl into a ball shape upon dehydration (see Figure 2.13(a)) to limit possible photoinhibitory and thermal damages in arid environment [106]. Such intelligent response, taking the inner stems as example, is attributed to the asymmetric lignification in cortical tissues towards the abaxial side of the stem, which could alter the hydro-actuation capacity and locally increase stiffness [106]. A similar hydration-driven hierarchical shape transformation was also recently found in *Daucus carota* umbel [107]. These interesting phenomenon inspired scientists to

develop bi-material based sensors and actuators by taking advantage of the strain misfit between the two distinct materials. For this purpose, it is of significant importance to disclose the relationship between strain mismatch and bending curvature.

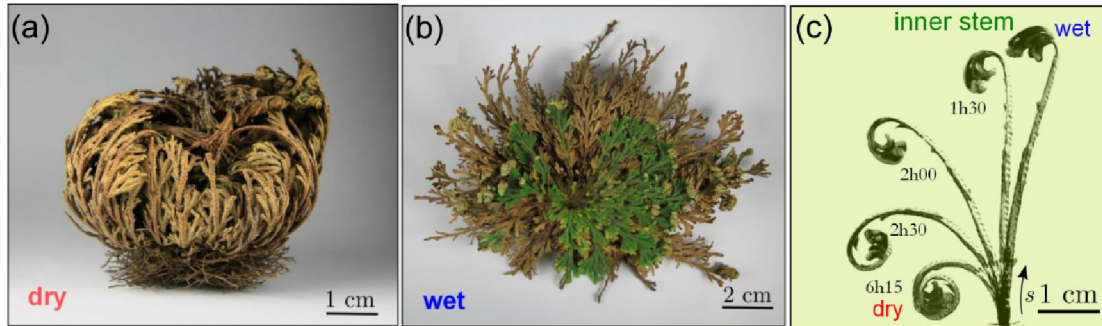


Figure 2.13 Morphology of *Selaginella lepidophylla* under (a) dry and (b) wet state. (c) Curling sequence of fully hydrated inner stems during dehydration. (Adapted from [106])

Timoshenko [108] proposed a general theory of bending of a bi-metal strip subjected to uniform heating (see Figure 2.14), which particularly applies to the operation of bi-metal strip thermostat. This theory is based on some assumptions: constant thermal expansion coefficients in bi-metals during heating, frictionless contact with the supports, and small width in the strip, etc. When the two bonded materials have distinct thermal expansion coefficients (denoted as  $\alpha_1$  and  $\alpha_2$  respectively), uniform heating from  $t_0^\circ\text{C}$  to  $t^\circ\text{C}$  will produce bending of the strip.

The bending curvature can be determined as [108]:

$$\kappa = \frac{1}{\rho} = \frac{(\alpha_2 - \alpha_1)(t - t_0)}{\frac{h}{2} + \frac{2(E_1 I_1 + E_2 I_2)}{h} \left( \frac{1}{E_1 a_1} + \frac{1}{E_2 a_2} \right)}$$

in which  $\rho$  is the radius of curvature of the bilayer strip,  $EI$  represents the flexural rigidity of the material. This equation correlates the thermal misfit and bending curvature of the narrow bi-material strip quantitatively. Certainly, it can be extended to more general cases with strain misfit originating from different sources like moisture absorption, phase transformation and mechanical loading. Through this relationship, the misfit strain in bi-materials can be estimated via measuring the bending curvature. In turn, controllable shape transformation can be achieved by simply introducing mismatch between the two materials.

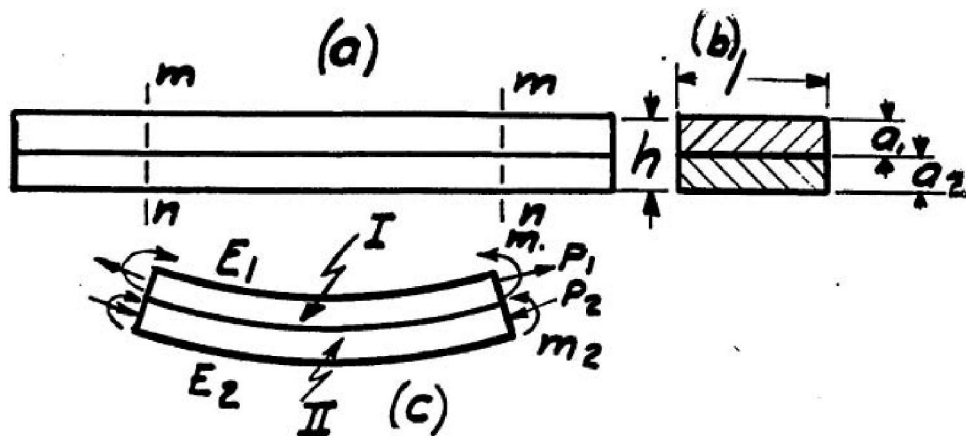


Figure 2.14 Deflection of bi-material strip subject to uniform heating. (Adapted from [108])

More recently, bi-materials have been extensively reported to achieve diverse shape transformations, like bending [109], curling [110], twisting [111], under the control of stimuli such as light [112], heat [113], electricity [114] or humidity [115]. By making use of these diverse deformations, specific functions can be achieved. For example, the repeatable bending-unbending deformation of bi-materials can mimic

the behaviors of hand, arm and joint of human beings, thus they can be developed into robotic arms [113] or grippers. The twisting of bi-materials can mimic the predation of python, so they can be developed into a gripping equipment [116]. In addition, the reversible and cyclic deformations of bi-materials can be used for continuous movement like rolling [109], walking [114, 115], jumping [117] and swimming [118]. For example, Shin et al. [115] reported a bilayer structure composed of a hydro-inactive film and a hygroscopically responsive film which could quickly swell and shrink in response to humidity variation (see Figure 2.15(a)). By attaching legs with asymmetric frictional coefficients, the repeated curling-uncurling motion of the bilayer structure under periodic humidity change can be transformed into continuous directional locomotion (see Figure 2.15(b)). By using liquid crystal elastomer (LCE) bilayers, Kotikian et al. [109] created a passively controlled, untethered soft robot (see Figure 2.15(c)). Upon heating the substrate, it would assemble into a pentagonal prism and then self-propel under thermal stimuli (see Figure 2.15(d, e)). Apart from diverse motions in air, a bilayer film reported by Ma et al. [118] can swim at liquid surface under cyclic UV light. The bilayer structure, consisting of azobenzene-containing LCNs and Kaptonw, could bend upon exposure to UV light while recover to initial flat state immediately after removing UV light. When placed on liquid surface and subjected to a cyclic UV light, the bilayer actuator would propel itself via beating the liquid like a dolphin (see Figure 2.15(f, g)).

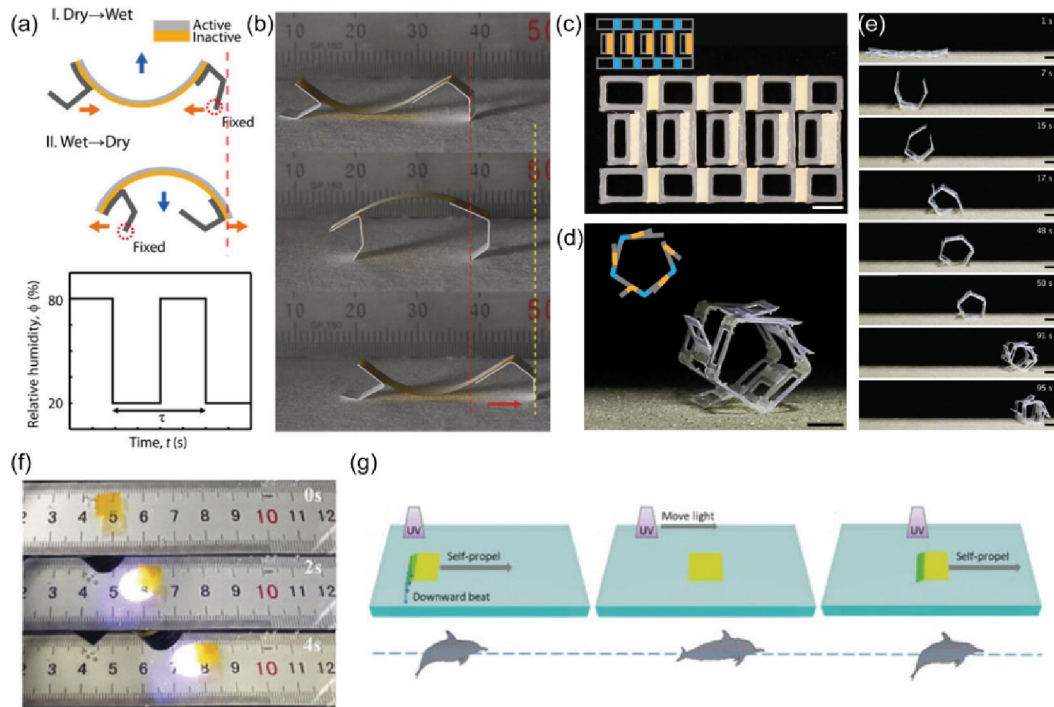


Figure 2.15 (a) Bilayer actuator with two legs attached. The static friction coefficients of the end tips and knees of legs are different. (b) Advance of actuator under periodic humidity variation. ((a, b) adapted from [115].) (c) Self-propelling robot in fabricated configuration. (d) Self-propelling robot in rolling configuration. (e) The self-propelling locomotion process of robot when heated. ((c-e) adapted from [109].) (f) The swimming of a bilayer actuator under cyclic UV light. (g) Schematic of the self-propelling actuator mimicking the dolphin. ((f, g) adapted from [118].)

On the other hand, strain misfit-driven deformation in bi-materials can be applied to manufacture complex shapes. Timber manufacturing industry faces difficulties that structurally efficient curved geometries are easy to be designed yet difficult to be manufactured. Recently, Grönquist et al. [119] proposed to fabricate large-scale curved mass timber via bilayer wood structures by moisture content changes. Some essential problems including shape prediction, sensitivity to variation of natural material properties and drying process, were addressed. Their work implies that such strain misfit-driven self-shaping method could be an efficient way to produce curved

timber structure in a large scale. Besides, Cafferty et al. [120] suggested an easy way to fabricate elastomeric three-dimensional (3D) structure by using strain misfit. The basic idea is to deposit elastomeric inks on a two-dimensional (2D) stretched elastomeric sheet firstly, and then relax the 2D sheet after ink curing to cause it to deform into a 3D shape. This route is capable of creating some shapes with complex curves in a faster way than 3D printing does.

### 2.3.2 Buckling pattern in bi-material systems

For film-substrate bi-material systems, when the film is subjected to compressive stress due to strain misfit, buckling may occur. Bowden et al. [121] established a theoretical model to predict the buckling initiation and their wavelength. As shown in Figure 2.16(a), a bi-material system with metallic stiff film deposited on thermally expanded thick, compliant PDMS substrate was particularly studied. When they are cooled to temperature  $T$  (below the deposition temperature  $T_D$ ) while without buckling initiation, the film would experience a uniform, equi-biaxial compressive stress [121]:

$$\sigma_0 = \frac{E_f(\alpha_s - \alpha_f)(T_D - T)}{1 - \nu_f}$$

Here, the subscripts 'f' and 's' represent film and substrate respectively,  $\nu$  denotes the Poisson's ratio,  $\alpha$  is the thermal expansion coefficient, and  $E$  is the Young's modulus. Such equi-biaxial compressive stress is caused by the misfit of thermal expansion

coefficients between the film and substrate. As cooling continues and compressive stress in the film increases, buckling occurs when the maximum principal compressive stress exceeds a critical value [121]:

$$\sigma_{\text{crit}} \approx 0.52 \left( \frac{E_f}{1-\nu_f^2} \right)^{1/3} \left( \frac{E_s}{1-\nu_s^2} \right)^{2/3}$$

The associated sinusoidal wave has wavelength predicted as [121]:

$$L \approx 4.36t \left[ \frac{E_f(1-\nu_s^2)}{E_s(1-\nu_f^2)} \right]^{1/3}$$

in which  $t$  is the film thickness. Although oversimplified, this model provides a quantitative relationship between buckling characteristics and the dimensions and properties of the bi-materials. Generally, equi-biaxial compressive stress would lead to randomly oriented wrinkles (Figure 2.16(b)). When some steps and edges are present, compressive stress would become highly oriented in the vicinity of the steps or edges and well aligned wrinkles would be formed perpendicular to the direction of maximum compressive stress (see Figure 2.16(c-e)) [121]. Additionally, the morphology of buckling wrinkles could be manipulated by regulating the dimensions and mechanical properties of the film. For instance, Lim et al. [122] found that by designing thickness gradient in the surface film, wrinkle propagation can be directed to form well aligned nanowrinkles, as opposed to the randomly oriented nanowrinkles for uniform film thickness. Feng and coworkers [123] reported that, by modifying the stiffness of soft material on the surface partially via ultraviolet-ozone

treatment, diverse wrinkling morphologies with designable dimensions and positions can be realized including sinusoidal wrinkles, folds, ridges, creases and sawteeth.

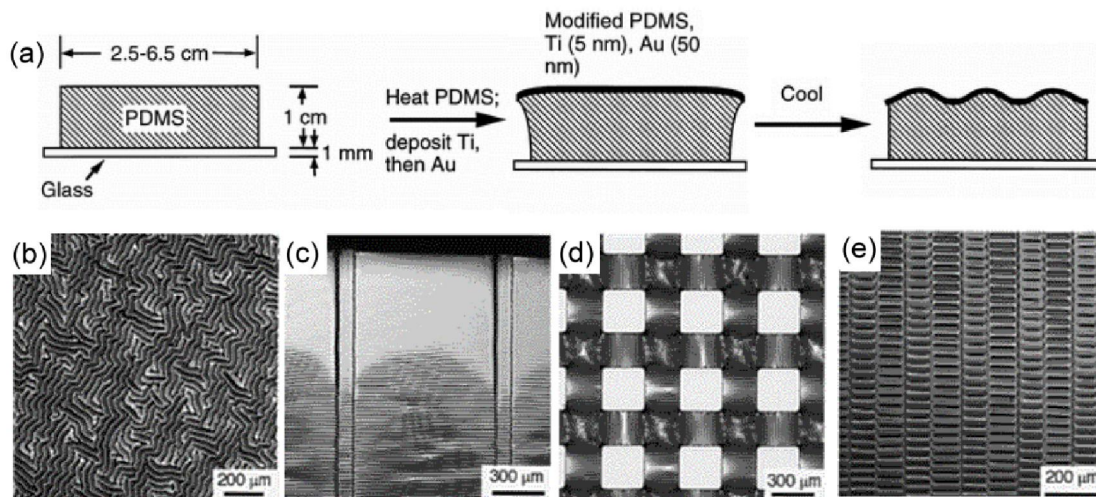


Figure 2.16 (a) The fabrication of buckling wrinkles on metal film-PDMS substrate system. (b-e) Optical micrographs showing the diverse buckling wave patterns. (b) Disordered regions far from any steps or edges. (c) A flat waveless region near edge gradually becomes a system with well aligned waves guided by the rectangular ridges. (d) Flat squares elevated relative to the surface exhibits no buckling on the plateau, but ordered wave patterns on the recessed regions between them. (e) Rectangular ridges directed the waves parallel to the direction of the protruding portion of PDMS. (Adapted from [121])

Buckling patterns on thin films or bilayers are of great interest for diverse applications [124-131]. Chandra et al. [127] proposed to fabricate strain responsive microlens arrays via buckling. As shown in Figure 2.17(a), the concave lens array is manufactured by patterning a hard oxide layer on a biaxial stretched soft elastomer, after which the applied strains are released to induce confined buckling. The focal length of the fabricated concave microlens array was reported capable of varying in a wide range of magnitude upon strain applied. Rogers and coworkers [128] produced

a stretchable silicon with periodical wavelike geometries on an elastomeric substrate via buckling (see Figure 2.17(b)). Such wavy silicon could accommodate deformations like stretching and compression without causing any damage in silicon itself, thus promising to be applied in stretchable electronics [131]. In addition, surface patterns are demonstrated to have great impact on the adhesion and release process, such as the fibrillar structure on the feet of geckos [132, 133] and some insects [134, 135]. Chan et al. [126] and Lin et al. [125] demonstrated that surface buckling wrinkles can be used to control the surface adhesion. Apart from convenient and simple fabrication process, buckling wrinkles exhibit enhanced capability in adhesion control.

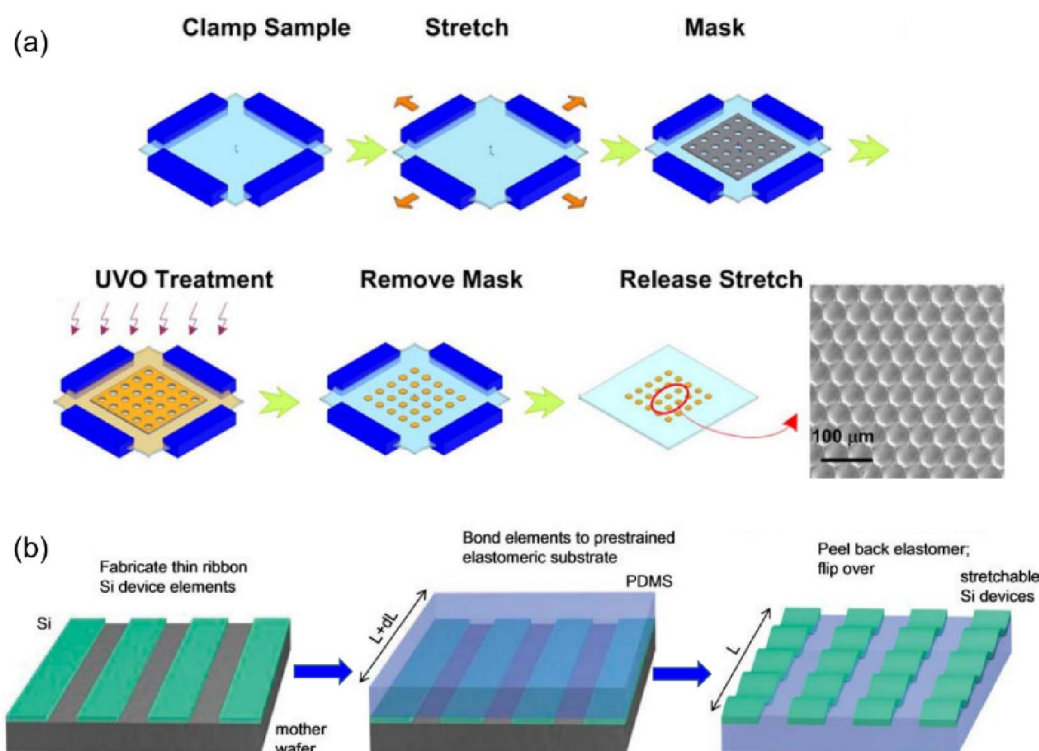


Figure 2.17 (a) Schematic diagram of the fabrication protocol of concave microlens array. (Adapted from [127].) (b) Schematic illustration of the process for building

stretchable Si devices on elastomeric substrate. (Adapted from [128])

On the other hand, buckling-induced delamination test provides an alternative way to measure the interface adhesion between the bi-materials [136-141]. For instance, Goyal et al. [136] designed a thermal-driven patterned buckling delamination test, and the interfacial fracture toughness was estimated based on a theoretical model. Likewise, Cordill et al. [137] employed a tensile test to induce film buckling and delamination. By measuring the buckle dimensions, the interfacial adhesion energy can be estimated by an energy-based model. In addition, Andersons et al. [138] evaluated the interface adhesion in film-substrate systems by modelling the buckling formation process via finite element simulation.

In this chapter, strategies to solve the interface-related problems in bi-materials and structures were reviewed. For the problem of weak interface-induced low mechanical properties, bio-inspired design strategies, including suture structure and brick-and-mortar structure, were found capable of improving the mechanical properties of bi-materials and structures. To mitigate the stress concentration on the interface induced by the strain misfit between the two materials, several strategies, including shape optimization, size reduction and gradient design, were found and discussed. Besides, strain misfit can be beneficial to the bi-materials and structures. By taking advantage of strain misfit between the two materials, controllable deformations including bending and buckling have been realized in various bi-materials systems, which are of great interest for a diversity of applications. Based

on the above introduction, further studies will be carried out to tackle the aforementioned interface-related problems in bi-materials and structures in this thesis.



## Chapter 3. Research methods

### 3.1 Experimental method

#### *Scratching test*

To evaluate the effect of spiral structure on the mechanical properties of the shell, scratching tests were carried out on the specimens (50 mm × 50 mm × 0.5 mm) incised from the central part of *P. placenta* shells with a precision cutting machine (Minitom, Struers). To minimize the effect of surface roughness on the scratching result, the surfaces of specimens were well polished with a series of sand papers from 400 to 7000 grits and lubrication with deionized (DI) water. Subsequently, samples were rinsed with DI water thoroughly and dried in air. Scratching tests were conducted using a diamond conical probe (Universal Mechanical Tester, Bruker). The scratching path was selected with caution so as to make it pass through the center of a micro-screw dislocation ( $\mu$ -SD). To avoid the interference between the adjacent scratches, the inter-scratch spacing was taken as at least 4 mm, which is more than 100 times of the maximum width of the scratch grooves. To verify the repeatability of the results, 10 mm long scratching was repeated on ten different samples with scratching speed taken as 0.04 mm/s. During the scratching processes, the normal force applied on the probe,  $F_n$ , was constantly taken as 0.3 N. The ratio of the measured horizontal resistance force to the fixed normal force,  $F_r/F_n$ , was used to depict the resistance of the material to wear.

## 3.2 Theoretical method

### 3.2.1 Elastic mechanics

For elastic problems, equilibrium equations, constitutive equations and geometric equations are generally involved to solve the displacement, stress and strain fields in the materials. Here, these relationships would be introduced. In Cartesian coordinate system, an infinitesimal element is considered (see Figure 3.1). Force equilibrium along  $x$  and  $y$  directions gives rise to

$$\frac{\partial \sigma_x}{\partial x} + \frac{\partial \tau_{yx}}{\partial y} + X = 0 \quad (3.1a)$$

$$\frac{\partial \sigma_y}{\partial y} + \frac{\partial \tau_{xy}}{\partial x} + Y = 0 \quad (3.1b)$$

in which  $X$  and  $Y$  represent the components of body force per unit volume. Eqs. (3.1) are differential equations of equilibrium for two-dimensional problems. Geometric relationship can be expressed as

$$\varepsilon_x = \frac{\partial u}{\partial x}, \quad \varepsilon_y = \frac{\partial v}{\partial y}, \quad \gamma_{xy} = \frac{\partial u}{\partial y} + \frac{\partial v}{\partial x} \quad (3.2)$$

in which  $u$  and  $v$  denote the displacement components along  $x$  and  $y$  directions, respectively.

For plane stress condition, we have  $\sigma_z=0$ . The constitutive relationship, i.e., Hooke's law, can be written as

$$\varepsilon_x = \frac{1}{E}(\sigma_x - \nu\sigma_y), \quad \varepsilon_y = \frac{1}{E}(\sigma_y - \nu\sigma_x), \quad \gamma_{xy} = \frac{1}{G}\tau_{xy} \quad (3.3)$$

in which  $E$ ,  $G$  and  $\nu$  represent the elastic modulus, shear modulus and Poisson's ratio of the material, respectively, and  $G=E/2(1+\nu)$ .

For plane strain condition, we have

$$\sigma_z = \nu(\sigma_x + \sigma_y) \quad (3.4)$$

Then the constitutive relationship becomes

$$\varepsilon_x = \frac{1+\nu}{E}[(1-\nu)\sigma_x - \nu\sigma_y], \quad \varepsilon_y = \frac{1+\nu}{E}[(1-\nu)\sigma_y - \nu\sigma_x], \quad \gamma_{xy} = \frac{1}{G}\tau_{xy} \quad (3.5)$$

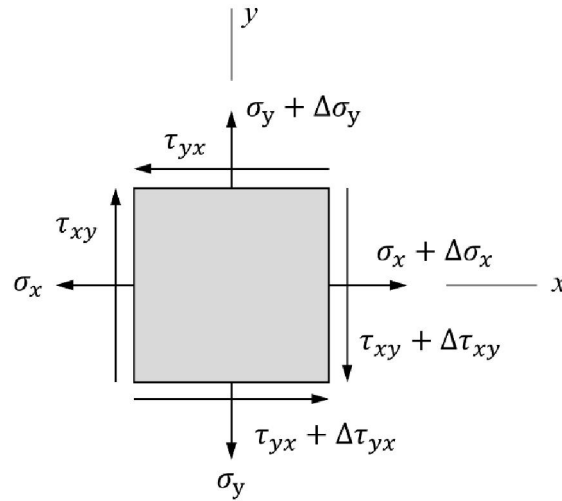


Figure 3.1 Free body diagram of an infinitesimal element in Cartesian coordinate

When discussing stresses in circular rings and disks, using polar coordinate would be more convenient. In polar coordinate system, the position of a point can be described by the distance from the origin  $O$  as well as the angle between  $r$  and a certain axis  $Ox$  fixed on the plane (see Figure 3.2). Here, an infinitesimal element is considered. Force equilibrium along the radial and circumferential directions gives

$$\frac{\partial \sigma_r}{\partial r} + \frac{1}{r} \frac{\partial \tau_{r\theta}}{\partial \theta} + \frac{\sigma_r - \sigma_\theta}{r} + R = 0 \quad (3.6a)$$

$$\frac{1}{r} \frac{\partial \sigma_\theta}{\partial \theta} + \frac{\partial \tau_{r\theta}}{\partial r} + \frac{2\tau_{r\theta}}{r} + S = 0 \quad (3.6b)$$

in which  $\sigma_r$  and  $\sigma_\theta$  denote the normal stresses along radial and circumferential directions respectively,  $\tau_{r\theta}$  denotes the shearing stress, and  $R$  and  $S$  represent the body force per unit volume along radial and circumferential directions, respectively.

If displacement components along radial and circumferential directions are denoted as  $u$  and  $v$ , respectively, the geometric relationships can be written as

$$\varepsilon_r = \frac{\partial u}{\partial r}, \quad \varepsilon_\theta = \frac{u}{r} + \frac{1}{r} \frac{\partial v}{\partial \theta}, \quad \gamma_{r\theta} = \frac{1}{r} \frac{\partial u}{\partial \theta} + \frac{\partial v}{\partial r} - \frac{v}{r} \quad (3.7)$$

It is worth pointing out that the normal strain along the circumferential direction depends on not only the circumferential displacement  $v$  but also the radial displacement  $u$ . For plane stress condition, Hooke's law can be expressed as

$$\varepsilon_r = \frac{1}{E} (\sigma_r - \nu \sigma_\theta), \quad \varepsilon_\theta = \frac{1}{E} (\sigma_\theta - \nu \sigma_r), \quad \gamma_{r\theta} = \frac{1}{G} \tau_{r\theta} \quad (3.8)$$

Combination of equilibrium equations, geometric equations and constitutive equations would give rise to the equilibrium in terms of displacement, which can be solved with specific boundary conditions. With the displacement field determined, the strain and stress fields in the material can then be solved based on geometric equations and constitutive equations.

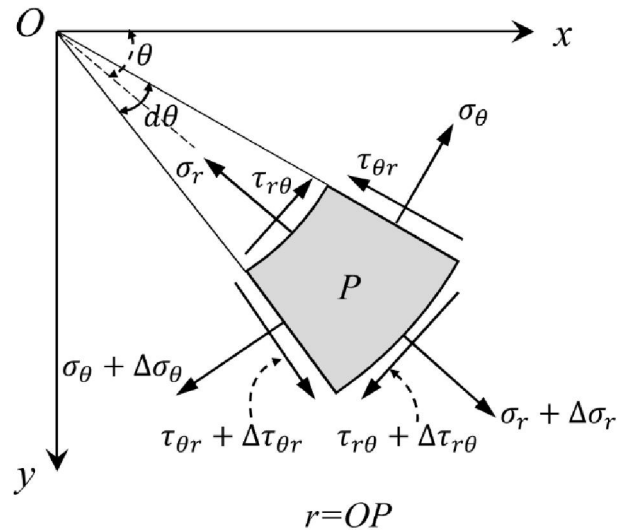


Figure 3.2 Free body diagram of an infinitesimal element in polar coordinate.

### 3.2.2 Fracture mechanics

#### a. Failure criteria

Failure criterion is a function of stress or strain to predict the failure of the material. When this function attains a critical value, which normally is the material strength, failure happens. In view of the complexity of stress state in different situations as well as distinct mechanical properties for different materials, several different failure criteria were exploited.

Maximum stress criterion postulates that failure happens when the maximum tensile stress in the material attains the critical value, i.e., tensile strength. If  $\sigma_1 > \sigma_2 > \sigma_3$ , we have

$$\sigma_1 = \sigma_0 \text{ (tension)} \quad (3.9)$$

in which  $\sigma_0$  denotes the tensile strength of the material. This criterion applies to brittle

materials only. Another criterion for brittle materials is maximum strain criterion, stating that material would fail when the maximum tensile strain in the material attains the critical value.

Maximum shear stress criterion, also known as Tresca yield criterion, postulates that material yields when the maximum shear stress attains the critical value,  $\tau_y$ , which represents the shear strength of the material. If  $\sigma_1 > \sigma_2 > \sigma_3$ , the maximum shear stress in the material can be expressed as

$$\tau_y = \frac{\sigma_1 - \sigma_3}{2} \quad (3.10)$$

This criterion is applicable for ductile materials. Von Mises yield criterion, also known as maximum distortion-energy criterion and  $J_2$  flow theory, is another failure criterion for ductile materials. It suggests that if the von Mises stress of the material under loading reaches the yield strength, yielding happens. This criterion can be expressed as

$$\sigma_v = \frac{\sqrt{2}}{2} \sqrt{(\sigma_1 - \sigma_3)^2 + (\sigma_2 - \sigma_3)^2 + (\sigma_1 - \sigma_2)^2} \geq \sigma_y \quad (3.11)$$

in which  $\sigma_y$  denotes the yield strength of material under uniaxial tension.

#### *b. Fracture mechanics approach*

The aforementioned failure criteria are based on the comparison of two variables, i.e., applied stress and material strength. Fracture mechanics approaches quantify the combination of three variables, including applied stress, flaw size and fracture toughness, to predict material failure [142]. Both energy criterion and stress intensity

approach can be employed to predict crack growth.

According to energy criterion, fracture happens when the energy available for crack growth is sufficient to overcome the resistance of the material, which includes the surface energy, plastic work and other types of energy dissipation associated with crack growth [142]. In linear elastic materials, the energy release rate,  $G$ , defined as the rate of change of potential energy for creating new surfaces, is applied to determine if the preexisting crack would grow or keep stable. When it increases to a critical energy release rate  $G_c$ , i.e., fracture toughness of the material, crack growth happens. For an infinite plate subject to remote tensile stress (see Figure 3.3), the energy release rate at the crack tip is given by

$$G = \frac{\pi\sigma^2 a}{E'} \quad (3.12)$$

in which  $E'=E$  for plane stress, and  $E'=E/(1-\nu^2)$  for plane strain with  $\nu$  denoting the Poisson's ratio of the material. Fracture happens when  $G= G_c$ . The energy release rate  $G$  serves as driving force for crack growth, while  $G_c$  represents materials' resistance.

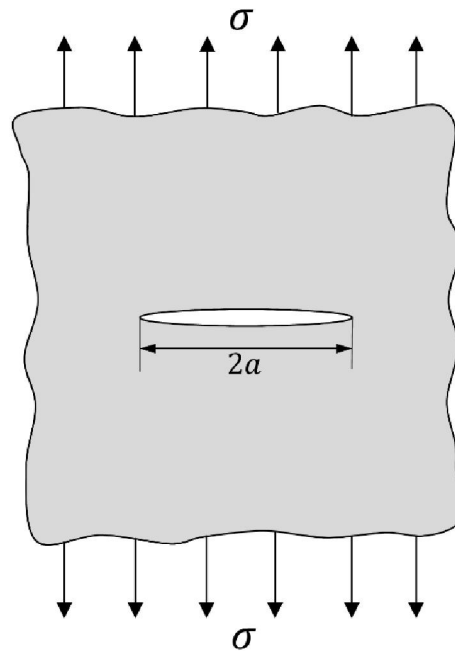


Figure 3.3 An infinite plate with a crack subject to a remote tensile stress

In linear elastic materials, the stress distribution around a crack tip can be characterized by a stress intensity factor,  $K$ . If the material would fail at some critical combinations of stress and strain, such fracture must correspond to a critical stress intensity  $K_c$ . For the plate shown in Figure 3.3, the stress intensity factor at the crack tip is given by

$$K_I = \sigma\sqrt{\pi a} \quad (3.13)$$

in which the subscript 'I' refers to Mode I tensile loading. Failure happens when  $K_I = K_{Ic}$ , in which  $K_I$  serves as the driving force for fracture and  $K_{Ic}$  is another measure of materials' resistance. By comparing Eqs. (3.12) (3.13), the relationship between  $K_I$  and  $G$  can be obtained

$$G = \frac{K_I^2}{E'} \quad (3.14)$$

indicating that for linear elastic materials, energy criterion and stress intensity approach are virtually equivalent. Eq. (3.14) is applicable to Mode I tensile loading only. When all three modes of loading are involved, Eq. (3.14) can be extended to

$$G = \frac{K_I^2}{E'} + \frac{K_{II}^2}{E'} + \frac{K_{III}^2}{2\mu} \quad (3.15)$$

in which  $\mu$  is shear modulus of the material.

### *c. Mixed-mode fracture*

A propagating crack always seeks the path of maximum driving force or the path of least materials' resistance, and may not necessarily be confined to its initial plane. If the material is isotropic and homogeneous, the crack will propagate in a way of maximum energy release rate [142]. Considering an angled crack oriented  $(90-\beta)$  degrees from the applied normal stress (see Figure 3.4(a)), the stress intensity factors for Modes I and II are given by

$$K_I = K_{I(0)} \cos^2 \beta \quad (3.16a)$$

$$K_{II} = K_{I(0)} \cos \beta \sin \beta \quad (3.16b)$$

in which  $K_{I(0)}$  is the Mode I stress intensity when  $\beta=0$ . Then the crack tip stress fields can be characterized by  $K_I$  and  $K_{II}$ . If there is an infinitesimal crack kinking at an angle  $\alpha$  away from the crack plane (see Figure 3.4(b)), the stress intensity at the tip of this

kink would be different from that of the main crack. Under the local  $x$ - $y$  coordinate system at the tip of kink, the Mode I and II stress intensity factors can be calculated by summing up all the normal and shear stress components, respectively, along the direction of  $\alpha$

$$k_I(\alpha) = \sigma_{yy} \sqrt{2\pi r} = C_{11}K_I + C_{12}K_{II} \quad (3.17a)$$

$$k_{II}(\alpha) = \tau_{xy} \sqrt{2\pi r} = C_{21}K_I + C_{22}K_{II} \quad (3.17b)$$

where  $k_I$  and  $k_{II}$  denote the local stress intensity factors at the kink tip. The coefficients are given by

$$\begin{aligned} C_{11} &= \frac{3}{4} \cos\left(\frac{\alpha}{2}\right) + \frac{1}{4} \cos\left(\frac{3\alpha}{2}\right) & C_{12} &= -\frac{3}{4} \left[ \sin\left(\frac{\alpha}{2}\right) + \sin\left(\frac{3\alpha}{2}\right) \right] \\ C_{21} &= \frac{1}{4} \left[ \sin\left(\frac{\alpha}{2}\right) + \sin\left(\frac{3\alpha}{2}\right) \right] & C_{22} &= \frac{1}{4} \cos\left(\frac{\alpha}{2}\right) + \frac{3}{4} \cos\left(\frac{3\alpha}{2}\right) \end{aligned} \quad (3.18)$$

Then the energy release rate for the kinked crack is given by

$$G(\alpha) = \frac{k_I^2(\alpha) + k_{II}^2(\alpha)}{E'} \quad (3.19)$$

Eq. (3.19) actually gives the directional dependence of the energy release rate at the tip of the main crack.  $G(\alpha)$  peaks at the point where  $k_I$  reaches the maximum while  $k_{II} = 0$  [142]. The maximum energy release rate thus is given by

$$G_{\max} = \frac{k_I^2(\alpha^*)}{E'} \quad (3.20)$$

in which  $\alpha^*$  represents the direction at which both  $G$  and  $k_I$  are maximized while  $k_{II} = 0$ .

Therefore, in a homogeneous material, crack kinking would happen along  $\alpha^*$  direction. However, if the material is anisotropic with directional-dependent fracture toughness, crack would kink into the direction that the driving force firstly reaches the materials' resistance.

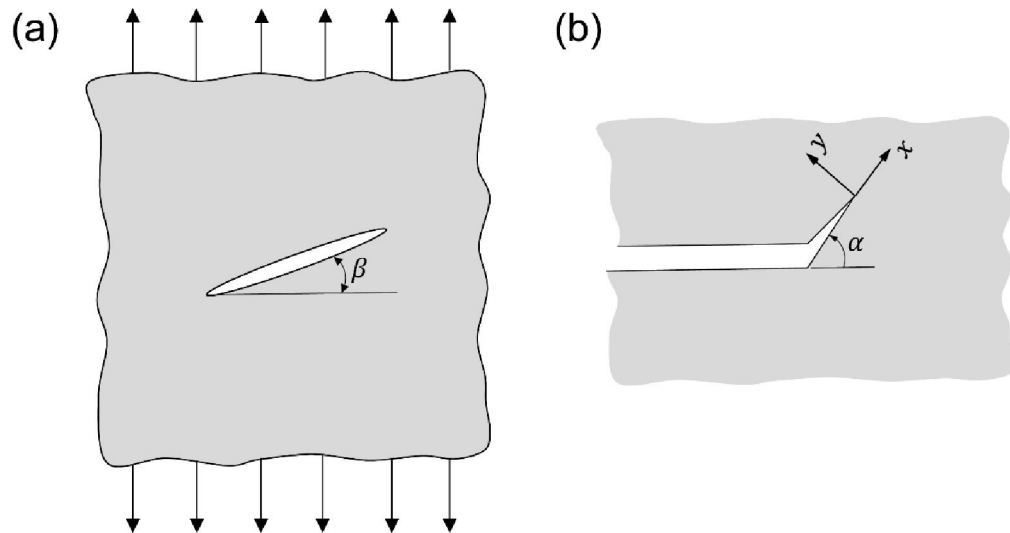


Figure 3.4 (a) An infinite plate with an angled crack subject to a remote tensile loading. (b) Infinitesimal kink at the tip of a macroscopic crack.

### 3.2.3 Finite element method

For some problems, the stress and strain fields in a body can be solved analytically when it is subjected to external force or displacement loading. For example, in Chapter 5, the strain misfit-induced stress and strain fields in film-substrate bi-material systems can be calculated based on the theory of elasticity. For most problems, however, it is difficult to derive the closed-form analytical solutions, especially when non-linear factors like plasticity and fracture are involved. Under such circumstance, finite element (FE) simulation [143] is often employed to give numerical solutions. On the

other hand, theoretical solutions can be verified and visualized via FE analysis, like the simulation work in Chapter 5 and Chapter 6. Here, the basics of finite element method are introduced.

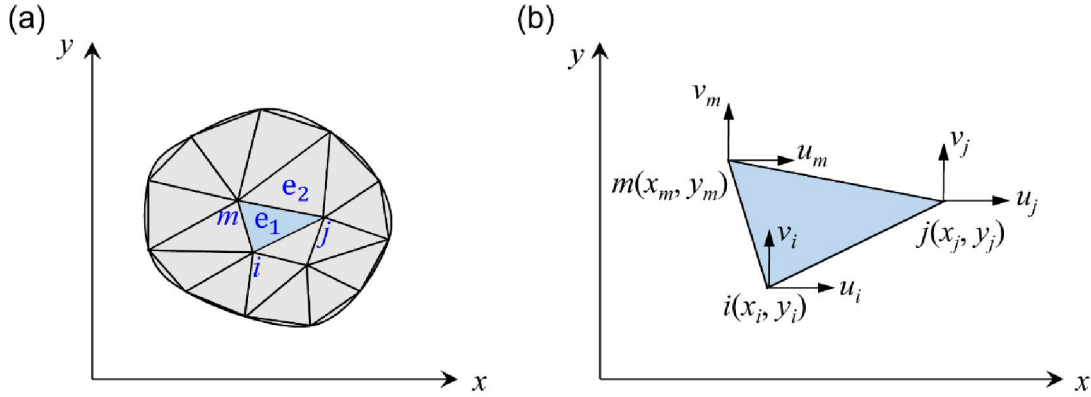


Figure 3.5 (a) Two-dimensional discrete domain, (b) Three-node triangle element

In finite element analysis, the object of interest is divided into a collection of discrete elements (see Figure 3.5(a)). These elements are connected by nodes, on which the displacements are continuous between neighboring elements. The element type should be chosen based on specific analysis requirement. Here, a typical three-node triangular element is taken for illustration (see Figure 3.5(b)). In the element with nodes numbered  $i, j$  and  $m$  in counterclockwise direction, the nodes displacements are

$$\mathbf{a}^e = \begin{pmatrix} \mathbf{a}_i \\ \mathbf{a}_j \\ \mathbf{a}_m \end{pmatrix} = [u_i \quad v_i \quad u_j \quad v_j \quad u_m \quad v_m]^T \quad (3.21)$$

Assuming that the displacement field  $(u, v)$  is a linear function of coordinates, the displacement field of this element can be expressed in the matrix form as

$$\mathbf{u} = \begin{pmatrix} u \\ v \end{pmatrix} = \begin{bmatrix} N_i & 0 & N_j & 0 & N_m & 0 \\ 0 & N_i & 0 & N_j & 0 & N_m \end{bmatrix} \begin{bmatrix} u_i \\ v_i \\ u_j \\ v_j \\ u_m \\ v_m \end{bmatrix} = \mathbf{N}\mathbf{a}^e \quad (3.22)$$

where

$$N_i = \frac{1}{2A}(a_i + b_i x + c_i y) \quad (i, j, m) \quad (3.23)$$

$$a_i = \begin{vmatrix} x_j & y_j \\ x_m & y_m \end{vmatrix}, \quad b_i = -\begin{vmatrix} 1 & y_j \\ 1 & y_m \end{vmatrix}, \quad c_i = -\begin{vmatrix} 1 & x_j \\ 1 & x_m \end{vmatrix} \quad (i, j, m) \quad (3.24)$$

and  $N$  is the shape function of the element,  $A$  is the area of this triangle element. Then the strain field within this element can be determined by

$$\boldsymbol{\varepsilon} = \begin{pmatrix} \varepsilon_x \\ \varepsilon_y \\ \gamma_{xy} \end{pmatrix} = \begin{bmatrix} \frac{\partial}{\partial x} & 0 \\ 0 & \frac{\partial}{\partial y} \\ \frac{\partial}{\partial y} & \frac{\partial}{\partial x} \end{bmatrix} \begin{bmatrix} u \\ v \end{bmatrix} = \mathbf{L}\mathbf{u} = \mathbf{L}\mathbf{N}\mathbf{a}^e = \mathbf{B}\mathbf{a}^e \quad (3.25)$$

where  $\mathbf{L}$  refers to the derivative operator, and  $\mathbf{B}=\mathbf{L}\mathbf{N}$  is the strain matrix. It can be demonstrated that

$$\mathbf{B} = [\mathbf{B}_i \quad \mathbf{B}_j \quad \mathbf{B}_m] = \frac{1}{2A} \begin{bmatrix} b_i & 0 & b_j & 0 & b_m & 0 \\ 0 & c_i & 0 & c_j & 0 & c_m \\ c_i & b_i & c_j & b_j & c_m & b_m \end{bmatrix} \quad (3.26)$$

Then the stress field within this element can be determined by

$$\boldsymbol{\sigma} = \begin{pmatrix} \sigma_x \\ \sigma_y \\ \tau_{xy} \end{pmatrix} = \frac{E_0}{1-\nu_0^2} \begin{bmatrix} 1 & \nu_0 & 0 \\ \nu_0 & 1 & 0 \\ 0 & 0 & \frac{1-\nu_0}{2} \end{bmatrix} \begin{pmatrix} \varepsilon_x \\ \varepsilon_y \\ \gamma_{xy} \end{pmatrix} = \mathbf{D}\boldsymbol{\varepsilon} = \mathbf{DB}\boldsymbol{a}^e = \mathbf{S}\boldsymbol{a}^e \quad (3.27)$$

where  $\mathbf{S} = \mathbf{DB} = [\mathbf{S}_i \quad \mathbf{S}_j \quad \mathbf{S}_m]$  referring to the stress matrix and

$$\mathbf{S}_i = \frac{E_0}{2(1-\nu_0^2)A} \begin{bmatrix} b_i & \nu_0 c_i \\ \nu_0 b_i & c_i \\ \frac{1-\nu_0}{2} c_i & \frac{1-\nu_0}{2} b_i \end{bmatrix} \quad (i, j, m) \quad (3.28)$$

where  $E_0=E$  and  $\nu_0=\nu$  for plane stress condition, and  $E_0=E/(1-\nu^2)$  and  $\nu_0=\nu/(1-\nu)$  for plane strain condition.

For this discrete system, the total potential energy can be calculated by

$$\begin{aligned} \Pi &= \frac{1}{2} \int_V \boldsymbol{\varepsilon}^T \boldsymbol{\sigma} dV - \int_V \mathbf{u}^T \mathbf{f} dV - \int_S \mathbf{u}^T \mathbf{T} dS \\ &= \sum_e \left( \mathbf{a}^{eT} \int_{\Omega_e} \frac{1}{2} \mathbf{B}^T \mathbf{DB} t dx dy \mathbf{a}^e \right) - \sum_e \left( \mathbf{a}^{eT} \int_{\Omega_e} \mathbf{N}^T \mathbf{f} t dx dy \right) - \sum_e \left( \mathbf{a}^{eT} \int_{S_e} \mathbf{N}^T \mathbf{T} t dS \right) \end{aligned} \quad (3.29)$$

in which  $t$  denotes the thickness of the 2D object, and  $\mathbf{f}$  denotes the body force applied on the object, and  $\mathbf{T}$  is the area force applied on the boundary of the object. We denote

$$\begin{aligned} \mathbf{K}^e &= \int_{\Omega_e} \mathbf{B}^T \mathbf{DB} t dx dy & \mathbf{P}_b^e &= \int_{\Omega_e} \mathbf{N}^T \mathbf{f} t dx dy \\ \mathbf{P}_S^e &= \int_{S_e} \mathbf{N}^T \mathbf{T} t dS & \mathbf{P}^e &= \mathbf{P}_b^e + \mathbf{P}_S^e \end{aligned} \quad (3.30)$$

in which  $\mathbf{K}^e$  and  $\mathbf{P}^e$  represent the element stiffness matrix and equivalent nodal loading array, respectively. The element displacement array can be expressed in terms of

global displacement array as

$$\mathbf{a}^e = \mathbf{G}\mathbf{a} \quad (3.31)$$

in which

$$\mathbf{a} = [u_1 \quad v_1 \quad u_2 \quad v_2 \quad \cdots \quad u_i \quad v_i \quad \cdots \quad u_n \quad v_n]^T \quad (3.32)$$

$$\mathbf{G}_{6 \times 2n} = \begin{matrix} & \begin{matrix} 1 & 2 & \cdots & 2i-1 & 2i & \cdots & 2m-1 & 2m & \cdots & 2j-1 & 2j & \cdots & 2n \end{matrix} \\ \begin{bmatrix} 0 & 0 & \cdots & 1 & 0 & \cdots & 0 & 0 & \cdots & 0 & 0 & \cdots & 0 \\ 0 & 0 & \cdots & 0 & 1 & \cdots & 0 & 0 & \cdots & 0 & 0 & \cdots & 0 \\ 0 & 0 & \cdots & 0 & 0 & \cdots & 0 & 0 & \cdots & 1 & 0 & \cdots & 0 \\ 0 & 0 & \cdots & 0 & 0 & \cdots & 0 & 0 & \cdots & 0 & 1 & \cdots & 0 \\ 0 & 0 & \cdots & 0 & 0 & \cdots & 1 & 0 & \cdots & 0 & 0 & \cdots & 0 \\ 0 & 0 & \cdots & 0 & 0 & \cdots & 0 & 1 & \cdots & 0 & 0 & \cdots & 0 \end{bmatrix} & \end{matrix} \quad (3.33)$$

where  $n$  denotes the total node number of the object. Inserting Eqs. (3.30-3.33) into Eq.

(3.29), we have

$$\Pi = \frac{1}{2} \mathbf{a}^T \mathbf{K}\mathbf{a} - \mathbf{a}^T \mathbf{P} \quad (3.34)$$

in which

$$\mathbf{K} = \sum_e \mathbf{G}^T \mathbf{K}^e \mathbf{G} \quad \mathbf{P} = \sum_e \mathbf{G}^T \mathbf{P}^e \quad (3.35)$$

representing global stiffness matrix and global nodal loading array, respectively. In the

light of the principle of minimum potential energy [143], we have

$$\mathbf{K}\mathbf{a} = \mathbf{P} \quad (3.36)$$

By introducing boundary conditions and solving Eq. (3.36), the global and element

displacement array can be obtained. After knowing the element displacement array, displacement, strain and stress fields can then be calculated via Eqs. (3.22) (3.25) and (3.27).

In this chapter, both experimental and theoretical approaches were introduced. These methods will be used to investigate the interfacial mechanics in bi-materials and structures.

## **Chapter 4. Spiral interface reinforced laminated composite**

Spiral or helix is a ubiquitous structural feature that is observed at length scales of wide range, from the double helical DNA [144-146] through the pattern of sunflower seeds [147, 148], all the way up to the Milky Way galaxy [149, 150], implying the essential roles they play in a variety of physical, chemical and biological processes. Recently, a unique microscopic spiral structure in the shells of mollusks of different species has attracted a bunch of attentions from material researchers. For example, the nacre layer of red abalone, which composites the microscopic aragonite tablets and proteins in the well-known “brick-and-mortar” structure [8-11], was found containing some spiral tablets called “screw dislocations” [151]. Similar spiral connections were also observed in the shell of bivalve *Placuna placenta*, which is a laminated composite composed of calcite laminae bonded together by thin layers of organic material [152]. The formation mechanism of such biological spiral structures was early attributed to the effect of atomistic dislocations on the growth of crystals [153]. Preliminary studies on the mechanical functions of these spiral structures indicated that the “screw dislocations” in nacre can enhance the strength by interlocking the vertically adjacent aragonite tablets and therefore constraining their relative motions [151]. For the shell of *P. placenta*, Li et al. demonstrated, from the perspective of energy dissipation and damage localization, that the “dislocation-like connections” can significantly improve

the resistance of the shell to the mechanical penetration [152]. The reinforcement effects of the spiral structures were basically attributed to the role of connection played by the spiral structures. However, if connection is their only function, it may not be necessary for nature to develop such a sophisticated structure. Although the spiral structures introduced above exhibit a quite similar morphology to screw dislocations, they are distinct in length scale. While screw dislocations are atomic defects [154], the spiral connectors are in micrometer scale. For distinction, in this chapter below they are designated as “microscopic screw dislocations” or  $\mu$ -SDs in short.

In this chapter, we first characterized the mechanical reinforcement effect of the  $\mu$ -SDs in the shell of *P. placenta* by microscopic scratching tests. Finite element-based simulation was subsequently performed to disclose the reinforcing mechanism of  $\mu$ -SDs. Theoretical modeling indicated that such reinforcing mechanism is not a spontaneous feature of the spiral interface. The condition for it to operate was explored and found dependent on the competition between the fracture toughness of the interface and substantial solid phase.

#### **4.1 Characterization of mechanical reinforcement**

Figure 4.1(a) shows the shells of *P. placenta* obtained from Shui Dong Bay, South China Sea, which are laminated composites composed of 99 wt% calcite and a small amount of organic material. The thickness of each calcite lamina and organic interlayer are 0.2-0.9  $\mu\text{m}$  [55] and 20-30 nm [55-57], respectively. Different from the

laminae in the traditional laminated composites [155], the mineral platelets in the shell of *P. placenta* are vertically interconnected through  $\mu$ -SDs [152]. These  $\mu$ -SDs exhibit either right-handed or left-handed helicity. Normally,  $\mu$ -SDs with opposite helicity appear in pairs, as shown in Figure 4.1(b) [156].

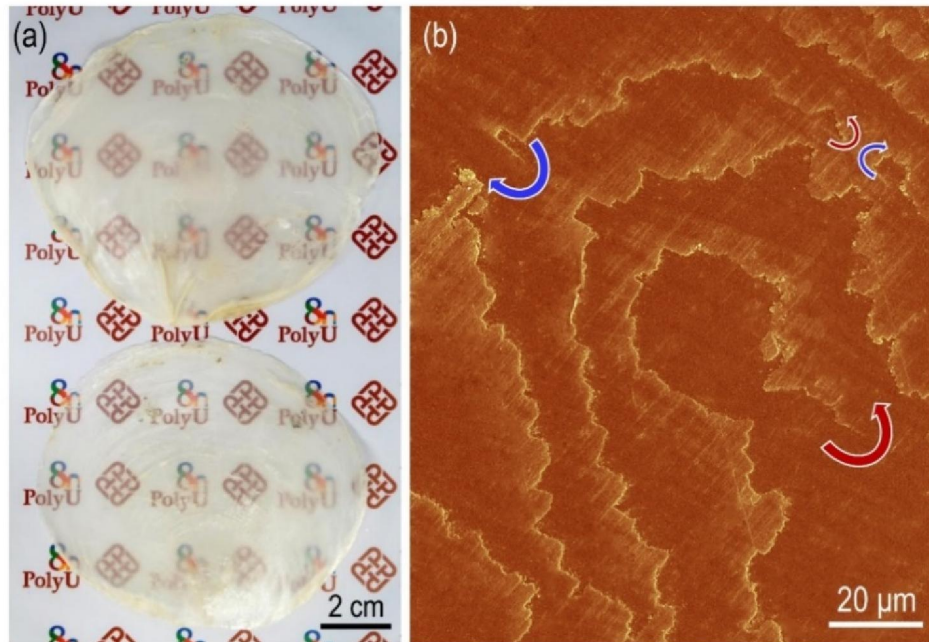


Figure 4.1 (a) Translucent shells of *P. placenta*. (b) False-colored SEM image of  $\mu$ -SDs in the shell of *P. placenta* with opposite helicity.

To evaluate the effect of spiral structure on the mechanical properties of the shell, scratching tests were carried out on the specimens incised from the central part of *P. placenta* shells. A typical scratch groove is shown in Figure 4.2(a) along with the corresponding wear resistance  $F_r/F_n$  with  $F_n$  denoting the constant normal force and  $F_r$  denoting the measured horizontal resistance force. As expected, the scratch groove passes through the center of a  $\mu$ -SD. The wear resistance, which is characterized by  $F_r/F_n$ , reaches the maximum around 0.8 near the  $\mu$ -SD center and exhibits relatively

lower value in the region distant from the  $\mu$ -SD. Since the sample surface has been well polished and the average groove depth ( $>15\mu\text{m}$  see Figure 4.2(b)) is much larger than the thickness of laminae (0.2-0.9  $\mu\text{m}$ ) [55], such elevated wear resistance near the center of the  $\mu$ -SD should not be attributed to the difference of altitude, if available, between the laminae. A plausible factor accounting for the higher resistance near the  $\mu$ -SD center is the spiral interfaces between laminae. For a laminated composite under in-plane scratching, cracks (mode-II dominant) form in the front of the probe and propagate as the scratching proceeds. Near a  $\mu$ -SD, the inter-lamina interface, which normally is weak compared to the lamina material, is no longer planar but spiral. When reaching a  $\mu$ -SD, cracks have the preference in energy to propagate along the spiral interface rather than directly penetrating through the lamina. The prolonged pathway of crack propagation along the spiral interface defers the failure of  $\mu$ -SD, giving rise to more energy consumption and higher resistance force. Such reinforcing mechanism of the spiral interface, if works in the scratching tests, is believed also functional in the fracture processes caused by the other mechanical loadings such as uniaxial tension. To verify this hypothesis, finite element analysis (FEA) is carried out to make a comparative study on the behaviors of the laminated composites with and without  $\mu$ -SDs.

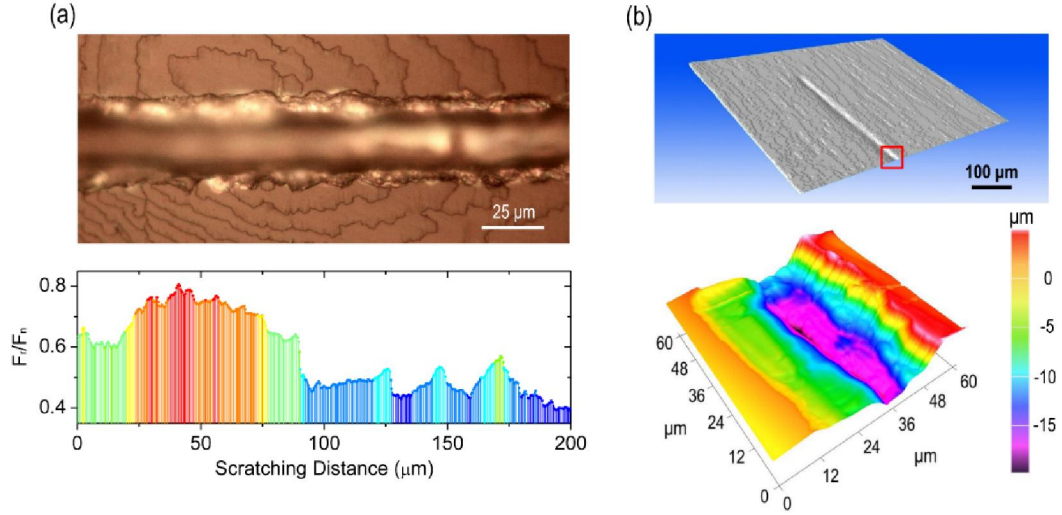


Figure 4.2 (a) A scratch groove passing through a  $\mu$ -SD and the corresponding real-time resistance force experienced by the probe. (b) The three-dimensional reconstruction of  $\mu$ -CT model of the scratched surface and the depth contour of the scratch groove obtained by surface scanning (Hysitron Ti 900).

## 4.2 Numerical verification of the reinforcement of spiral interface

A virtual model of  $\mu$ -SD is constructed by embedding a spiral interface (in green) into a cylinder (in gray), as shown in Figure 4.3(a). In the accompanying Cartesian coordinate system  $(x, y, z)$ , the spiral interface is described by parametric equations with respect to the polar coordinates  $(r, \beta)$  as

$$\begin{cases} x = r \cos \beta \\ y = r \sin \beta \quad (r \in [0, D/2] \text{ and } \beta \in [0, 2\pi l/p]) \\ z = p\beta/2\pi \end{cases} \quad (4.1)$$

where  $p$  is the spiral pitch,  $D$  and  $l$  denote the diameter and length of the specimen as indicated in Figure 4.3(a). For comparison, a model of conventional laminated composite is also constructed by embedding parallel planar interfaces separated by distance  $p$  into a similar cylinder, as shown in Figure 4.3(b). Take  $D=18 \mu\text{m}$ ,  $l=15 \mu\text{m}$

and  $p=1 \mu\text{m}$ . It can be demonstrated that the relative difference between the interface area in both models is less than 0.2 %, implying much alike compositions in both composites. Displacement-controlled uniaxial tension was simulated with commercial FEA package ABAQUS (Version 6.13, Dassault Systèmes). In our simulations, the laminae were depicted as linear elastic solid with elastic modulus  $E_{\text{la}} = 100 \text{ GPa}$  [57, 157] and Poisson's ratio being 0.33. As the organic layer is normally much thinner than the mineral lamina in the shell of mollusks, cohesive element (COH3D8 in ABAQUS) with zero initial thickness was applied to describe the interface between laminae. By referring to the reported properties of the organic material in the biological laminated composites [158], the characteristic parameters of the cohesive element in our simulation are taken as typical values shown in Table 4.1.

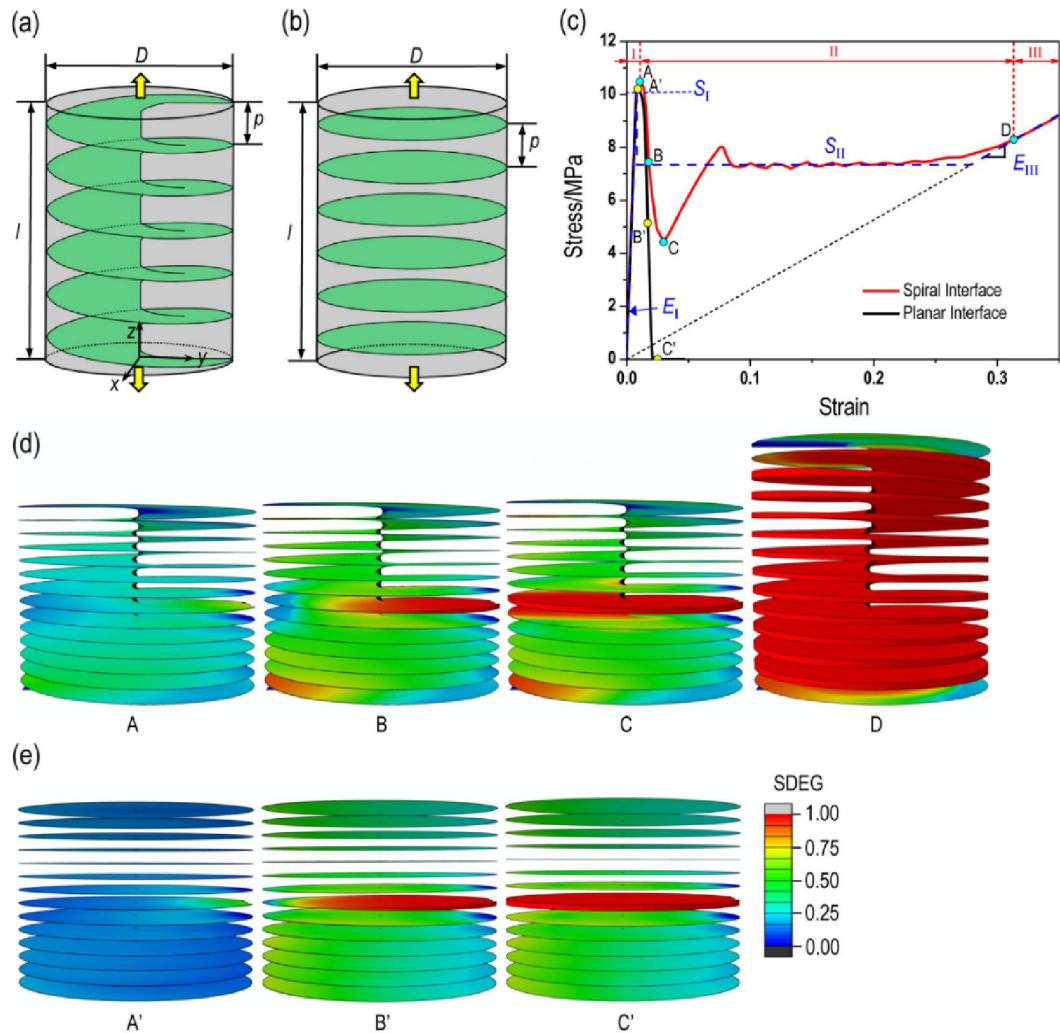


Figure 4.3 Schematics of finite element models for laminated composites with (a) spiral and (b) parallel planar interfaces.  $D=18 \mu\text{m}$ ,  $l=15 \mu\text{m}$  and  $p=1 \mu\text{m}$ ; (c) Calculated stress-strain curves for two models under uniaxial tension.  $S_I$ ,  $S_{II}$ ,  $E_I$  and  $E_{III}$  are the characteristic mechanical properties of  $\mu$ -SD predicted by theory; (d, e) Snapshots of the SDEG (scalar stiffness degradation variable) field at different moments as indicated on the stress-strain curves in (c) showing the evolution of the interface damage. The deep blue color (SDEG=0) represents zero damage while the deep red color (SDEG=1.0) stands for the complete damage. For clarity, the lamina phase is hidden here.

Table 4.1 Characteristic parameters of cohesive elements (COH3D8 in ABAQUS) adopted in the finite element simulations

Stiffness $K_{in}$ (GPa/ $\mu\text{m}$ )	Fracture energy $G_{in}$ (J/m <sup>2</sup> )	Strength $S_{in}$ (MPa)
1.25	1.0	10

Figure 4.3(c-e) shows the calculated stress-strain curves in company with the snapshots of the interface degradation at several important moments. For the composite with spiral interface ( $\mu$ -SD), the stress-strain curve exhibits three characteristic stages (see Figure 4.3(c)). In stage I when the deformation is relatively small, the stress increases linearly with the strain. Such linear elasticity ends when the strain reaches a value around 1% at point A, giving rise to the strength of  $\sim 10.5$  MPa. After reaching the summit A, the stress drops quickly to  $\sim 4.4$  MPa. An in-depth investigation into the status of cohesive elements indicates that such a drop of load-carrying capacity is basically due to the yielding and subsequent delamination of the interface, as shown in Figure 4.3(d). With the growth of the delaminated spiral interface, the stress is maintained almost at a steady level even though small oscillation is present. With the increase of deformation, eventually the spiral interface is completely damaged at point D. From then on, deformation enters into stage III, in which linear elasticity returns. Such linear elasticity in stage III lasts all along until the damage of the lamina material, which has not been considered in our analysis.

In contrast, for the composite with planar interfaces, the calculated stress-strain curve in Figure 4.3(c) exhibits a much more brittle behavior. Firstly, when the strain is

smaller than 1%, a linear elasticity is also observed. After reaching the peak at point A', the stress drops abruptly to zero (point C'). Such catastrophic failure of the material is basically due to the propagation of the crack throughout a planar interface, as shown in Figure 4.3(e). The distinct mechanical behaviors of laminated composites with spiral and planar interfaces in Figure 4.3(c) confirm the reinforcing mechanism of  $\mu$ -SD.

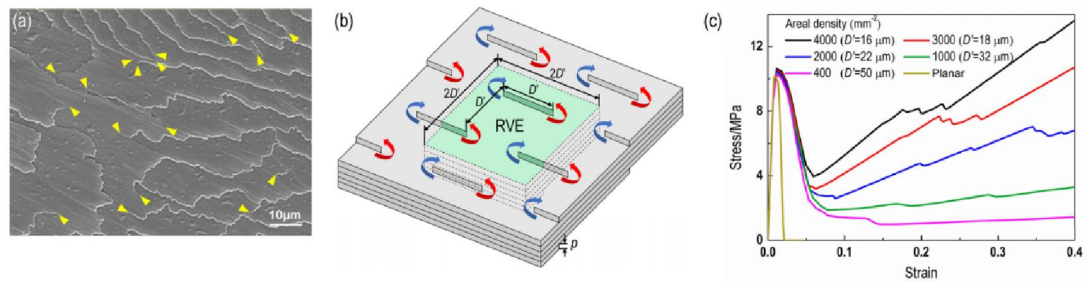


Figure 4.4 (a) SEM image of an area ( $90 \mu\text{m} \times 70 \mu\text{m}$ ) on shell of *P. Placenta* containing 17  $\mu$ -SDs as marked by the yellow arrows. The areal density is estimated to be  $\approx 2,700 \text{ mm}^{-2}$ . (b) Schematics of an idealized composite model containing periodically distributed  $\mu$ -SD couples. A representative volume element (RVE) with dimensions of  $2D' \times 2D'$  is highlighted in green. (c) Calculated stress-strain curves for composites with  $\mu$ -SDs of different areal densities using the RVE model shown in (b).

Above analysis demonstrated the reinforcement of an individual  $\mu$ -SD. To shed light on the effect of multiple  $\mu$ -SDs on the mechanical behavior of laminated composites, the density of  $\mu$ -SDs should be considered. An earlier study [152] indicated that the areal density of  $\mu$ -SDs in the shell of *P. Placenta* is about 100-400  $\text{mm}^{-2}$ . However, our reexamination indicated that this might be the average density of  $\mu$ -SDs over a relatively large area. For a smaller region, the local density of  $\mu$ -SDs could reach 1,000-4,000  $\text{mm}^{-2}$ , which is one order of magnitude higher than the above

mean value. Figure 4.4(a) shows a region containing 17  $\mu$ -SDs. The local density is estimated to be 2,700 mm<sup>-2</sup>. For simplicity, our study on the effect of density was carried out by using an idealized model in which the distribution of  $\mu$ -SDs was assumed periodical (see Figure 4.4(b)). A RVE model with dimensions of  $2D' \times 2D'$  was selected for analysis with periodical boundary conditions applied on four lateral sides. By applying uniaxial tension on the top and bottom sides, the mechanical behavior of a composite with  $\mu$ -SD density of  $1/D'^2$  is simulated. The calculated stress-strain curves for composites with different areal densities of  $\mu$ -SD are shown in Figure 4.4(c). As in the case of individual  $\mu$ -SD (Figure 4.3(c)), three characteristic stages can be observed in the cases with high densities (e.g., 2,000, 3,000, 4,000 mm<sup>-2</sup>), implying the operation of the reinforcing mechanism of  $\mu$ -SDs. In contrast, for the case with density as low as 400 mm<sup>-2</sup>, the stress drops abruptly from the maximum to a quite low value. Recovery of stress to a higher level does not happen as in the cases with high densities, implying little reinforcement as in the case with planar interfaces. Therefore, the reinforcement of the spiral interface in the laminated composites depends on the  $\mu$ -SD density very much. The higher the density the higher the reinforcement.

### 4.3 Theoretical prediction of mechanical behaviors of $\mu$ -SD

The preceding FEA simulation results disclose the reinforcing mechanism of  $\mu$ -SD. In this section, theoretical models will be further established to predict the mechanical

behaviors of  $\mu$ -SD under uniaxial tension. A  $\mu$ -SD can be taken as a composite of a spiral lamina and interfacial adhesive. We assume lamina is elastic solid and interface can be described by a traction-separation law as shown in Figure 4.5(a). According to the FE simulation result, a  $\mu$ -SD under uniaxial tension is believed to experience three distinct stages of deformation as depicted by three characteristic segments on a schematic stress-strain plot (see Figure 4.5(b)). At stage I, both the spiral lamina and interface deform elastically, leading to the elastic behavior of the composite characterized by the effective elastic modulus  $E_I$ . With the increase of deformation, such elasticity continues until the interfacial traction reaches its maximum allowable value  $S_{in}$  (see Figure 4.5(a)), giving rise to the strength  $S_I$  of the  $\mu$ -SD at stage I (see Figure 4.5(b)). From then on, interfacial delamination starts, resulting in a drop of load-bearing capacity of the  $\mu$ -SD. However, due to the spiral morphology of the interface, interfacial delamination will not propagate thoroughly across the  $\mu$ -SD as that in the regular laminated composite. Instead, it will grow progressively along a spiral path under stress  $S_{II}$  which gives rise to the strength of the  $\mu$ -SD at stage II. Once the spiral interface delaminates completely, the  $\mu$ -SD turns to be a monolithic spiral structure. Afterward, the  $\mu$ -SD is expected to deform elastically with effective elastic modulus being  $E_{III}$ . In the following, theoretical estimations of  $E_I$ ,  $S_I$ ,  $S_{II}$  and  $E_{III}$  are carried out.

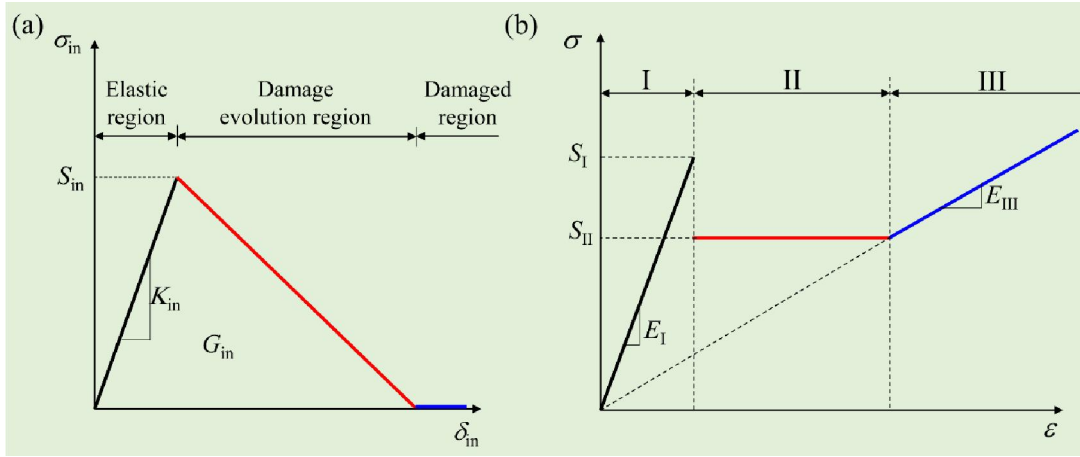


Figure 4.5 (a) Schematics of traction-separation law for bilinear cohesive elements modelling adhesive interface, (b) Schematic stress-strain curve of  $\mu$ -SD under uniaxial tension.

The effective elastic modulus of a  $\mu$ -SD with intact interface ( $E_I$ ) should be a function of the effective elastic modulus of interface ( $K_{in}p$ , see Eq. (4.16)), the effective modulus of the plain spiral structure ( $E_{III}$ , see Eq. (4.12) for deviation), and the elastic modulus of lamina materials ( $E_{la}$ ). To shed light on the form of this function, discussion on its asymptotic values is helpful. Clearly, if the interface stiffness is quite large ( $K_{in} \rightarrow \infty$ ), no separation is allowed before the initiation of damage. Therefore, the  $\mu$ -SD behaves like a monolithic cylinder made of the lamina material, implying that  $E_I$  approaches  $E_{la}$  as  $K_{in} \rightarrow \infty$ . On the other hand, if  $K_{in} \rightarrow 0$ ,  $E_I$  must approach to the effective elastic modulus of  $\mu$ -SD with completely failed interface ( $E_{III}$ ). These two asymptotic properties of  $E_I$  in combination with the basic mixture laws of composites [159, 160] inspire us to write  $E_I$  in the following form

$$E_I = \left( \frac{1}{E_{la}} + \frac{1}{E_{III} + K_{in}p} \right)^{-1} \quad (4.2)$$

It can be verified from Eq. (4.2) that  $E_I \rightarrow E_{la}$  as  $K_{in} \rightarrow \infty$ , and  $E_I \rightarrow \left( \frac{1}{E_{la}} + \frac{1}{E_{III}} \right)^{-1}$  as  $K_{in} \rightarrow 0$ . Considering  $p/D \ll 1$ , the expression of  $E_{III}$  (see Eq. (4.12)) implies that  $E_{III} \ll E_{la}$ . Therefore,  $E_I \rightarrow E_{III}$  as  $K_{in} \rightarrow 0$ . Two asymptotic values of  $E_I$  are both confirmed. Inserting the expression of  $E_{III}$  (see Eq. (4.12)) into Eq. (4.2),  $E_I$  can be rewritten as

$$E_I = \left( \frac{1}{E_{la}} + \frac{1}{2E_{la}p^2 / (Q\pi D \sqrt{\pi^2 D^2 + p^2}) + K_{in}p} \right)^{-1} \quad (4.3)$$

where  $Q$  is a correction factor determined to be around 2.4 from our simulation.

The maximum stress that a  $\mu$ -SD can sustain before the initiation of damage of the included spiral interface contains two portions. One is the portion to overcome the maximum interfacial traction, which is equal to the strength of interface ( $S_{in}$ ). The other portion is to deform the spiral solid to such an extent that makes the interfacial traction reach its maximum  $S_{in}$ . Since the interfacial separation at the maximum traction is  $S_{in}/K_{in}$  (see Figure 4.5(a)), the effective strain of the spiral solid with effective modulus  $E_{III}$  is  $S_{in}/K_{in}p$ , implying that the stress required for such deformation is  $S_{in}E_{III}/K_{in}p$ . Therefore, we have

$$S_I = S_{in} + \frac{S_{in}E_{III}}{K_{in}p} = S_{in} \left( 1 + \frac{E_{III}}{K_{in}p} \right) \quad (4.4)$$

Since  $E_{\text{III}} = \frac{2p^2}{Q\pi D\sqrt{\pi^2 D^2 + p^2}} E_{\text{Ia}}$  (see Eq. (4.12)),  $S_{\text{I}}$  can be rewritten as

$$S_{\text{I}} = S_{\text{in}} \left( 1 + \frac{2pE_{\text{Ia}}}{Q\pi DK_{\text{in}}\sqrt{\pi^2 D^2 + p^2}} \right) \quad (4.5)$$

which gives  $S_{\text{I}} = 10.2$  MPa according to the associated parameters we selected, showing good consistence with the FEA result (see Figure 4.3(c)).

In stage II, the spiral interface of  $\mu$ -SD delaminates progressively under the tensile loading of  $S_{\text{II}}$ . From the point of view of energy equilibrium, during this process the energy required to fracture the interface should be equal to the released strain energy of a unit segment of  $\mu$ -SD transforming from intact state to delaminated state. We therefore have

$$G_{\text{in}} = \left( \frac{S_{\text{II}}^2}{2E_{\text{III}}} - \frac{S_{\text{II}}^2}{2E_{\text{I}}} \right) p \quad (4.6)$$

where  $G_{\text{in}}$  is the fracture energy of interface. From Eq. (4.6), the strength of  $\mu$ -SD in stage II ( $S_{\text{II}}$ ) is thus given by

$$S_{\text{II}} = \sqrt{\frac{2G_{\text{in}}E_{\text{I}}E_{\text{III}}}{p(E_{\text{I}} - E_{\text{III}})}} \quad (4.7)$$

By inserting Eq. (4.3) and  $E_{\text{III}}$  (see Eq. (4.12)) into Eq. (4.7),  $S_{\text{II}}$  can be given as

$$S_{\text{II}} = \sqrt{\frac{2G_{\text{in}}}{\frac{Q\pi DK_{\text{in}}\sqrt{\pi^2 D^2 + p^2}}{2pE_{\text{Ia}}} / (2pE_{\text{Ia}}) - \frac{p}{E_{\text{Ia}}}}} \quad (4.8)$$

By substituting the values of associated parameters into Eq. (4.8), we have  $S_{\text{II}} = 7.3$

MPa which is in good agreement with the simulation result, as shown in Figure 4.3(c). The ratio of  $S_{II}/S_I$ , which can be used to assess the reinforcement of a  $\mu$ -SD, is shown in Figure 4.6. For a given ratio  $D/p$ ,  $S_{II}/S_I$  decreases with increasing  $D$ , implying strong size dependence of the reinforcement. The smaller the  $\mu$ -SD, the higher the reinforcement.

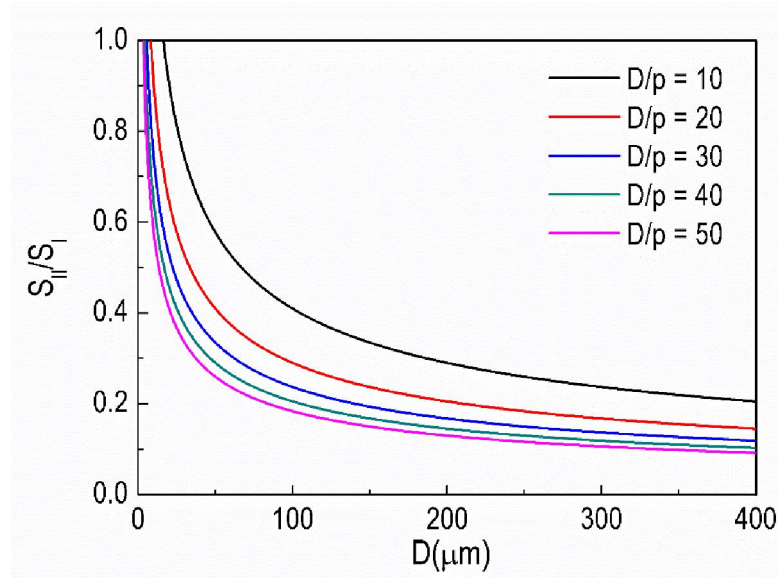


Figure 4.6 Dependence of  $S_{II}/S_I$  of a  $\mu$ -SD on the length scale characterized by  $D$ . Here, following representative values are taken:  $G_{in}=1.0 \text{ J/m}^2$ ,  $K_{in}=1.25 \text{ GPa}/\mu\text{m}$ ,  $S_{in}=10 \text{ MPa}$ ,  $E_{la}=100 \text{ GPa}$  and  $Q=2.4$ .

Once the spiral interface fails completely, the  $\mu$ -SD turns to be a monolithic solid with spiral structure. To estimate its effective elastic modulus,  $E_{III}$ , a unit segment is considered as shown in Figure 4.7(a), from which we select an annular element with infinitesimal thickness  $dr$  for analysis. The free body diagram is shown in Figure 4.7(b). Considering the analogy of this problem in mechanics to a clamped beam under transverse loading (see Figure 4.7(b)), the correlation between the force,  $dF$ ,

and the resulting deflection  $\delta$  can be easily established as

$$\delta = Q \frac{L^3 dF}{12E_{\text{la}} I} \quad (4.9)$$

where  $Q$  is the correction factor to be determined by simulation,  $I = p^3 dr/12$  and

$L = \sqrt{p^2 + (2\pi r)^2}$  are the moment of inertia and length of the analogic beam with  $p$

being the pitch of the spiral structure. Eq. (4.9) thus can be rewritten as

$$dF = \frac{\delta E_{\text{la}} p^3}{Q [p^2 + (2\pi r)^2]^{3/2}} dr \quad (4.10)$$

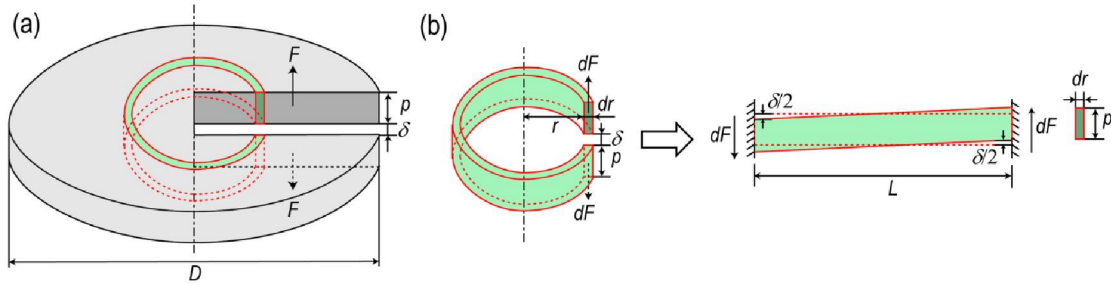


Figure 4.7 (a) Schematics of a unit segment of  $\mu$ -SD with failed interface. (b) Free body diagram of an annular element for analysis and its analogy.

Taking integration on both sides of Eq. (4.10) gives rise to

$$F = \frac{E_{\text{la}} p^3 \delta}{Q} \int_0^{D/2} [p^2 + (2\pi r)^2]^{-3/2} dr = \frac{E_{\text{la}} D p \delta}{2Q \sqrt{\pi^2 D^2 + p^2}} \quad (4.11)$$

where  $D$  is the diameter of the unit segment of  $\mu$ -SD (see Figure 4.7(a)). The effective

modulus of  $\mu$ -SD with completely failed interface can be determined as

$$E_{\text{III}} = \frac{4F/(\pi D^2)}{\delta/p} = \frac{2p^2}{Q\pi D \sqrt{\pi^2 D^2 + p^2}} E_{\text{la}} \quad (4.12)$$

By inserting the values of the associated parameters into Eq. (4.12),  $E_{\text{III}}$  is estimated to

be around 26.1 MPa, which is in good consistency with the simulation result, as shown in Figure 4.3(c). Thus, the mechanical behaviors of an individual  $\mu$ -SD under uniaxial tension are well predicted. When  $D \gg p$ , Eq. (4.12) can be further simplified as

$$E_{III} \approx \frac{2p^2}{Q\pi^2 D^2} E_{la} \quad (4.13)$$

In addition, the effective elastic modulus of laminated composite with planar interface is also predicted here (see Figure 4.3(b)). Similarly, we assume that the constitutive behavior of the adhesive interface between laminae can also be described by a traction-separation law as shown in Figure 4.5(a). Under external uniaxial loading  $\sigma$ , the axial elongation of a unit segment consisting of one lamina and one layer of adhesive interface is given by

$$\delta = \frac{\sigma}{E_{la}} \cdot p + \delta_{in}(\sigma) \quad (4.14)$$

where  $E_{la}$  and  $p$  are the elastic modulus and thickness of the lamina, respectively;  $\delta_{in}(\sigma)$  is the interfacial separation of the adhesive under traction  $\sigma$ . The effective strain of the segment or the composite is thus given by

$$\varepsilon = \frac{\delta}{p} = \frac{\sigma}{E_{la}} + \frac{\delta_{in}(\sigma)}{p} \quad (4.15)$$

Here, the original thickness of the adhesive interface is neglected. The effective elastic modulus of the laminated composite with planar interfaces thus can be given by

$$E_{\text{planar}} = \frac{\sigma}{\varepsilon} = \left( \frac{1}{E_{\text{la}}} + \frac{\delta_{\text{in}}(\sigma)}{p\sigma} \right)^{-1} = \left( \frac{1}{E_{\text{la}}} + \frac{1}{K_{\text{in}}p} \right)^{-1} \quad (4.16)$$

where  $K_{\text{in}}$  denotes the initial slope of the traction-separation curve for the interface (see Figure 4.5(a)). In the light of Eq. (4.16), it can be seen that  $K_{\text{in}}p$  represents the effective elastic modulus of the interface material. Comparing Eq. (4.16) with Eq. (4.3), it is found that when  $D \gg p$ , the effective elastic modulus of spiral structure ( $E_I$ ) and planar structure ( $E_{\text{planar}}$ ) is quite close.

#### 4.4 Working condition for the reinforcing mechanism of $\mu$ -SD

The enhancement of  $\mu$ -SDs to the mechanical properties of laminated composites shown above is mainly attributed to the spiral interface which could guide the crack to propagate along a prolonged helical path. Clearly, this is not always the case because if the interface is much tougher compared to the lamina material, most likely a growing interfacial crack will deviate from the interface and penetrate into the laminae. Preventing the deviation of a growing interfacial crack from the spiral interface is crucial for ensuring the operation of the underlying reinforcing mechanism. For this purpose, a theoretical model was developed by analogizing the frontier of a spiral interfacial crack (see Figure 4.8(a)) to a 2D (plane strain) crack under mixed mode loading (see Figure 4.8(b)). The problem now comes down to finding the condition for ensuring the propagation of an interfacial crack along the interface under any external mixed-mode loading.

For a mixed-mode crack shown in Figure 4.8(b), the directional dependence of the energy release rate at the crack tip is given by [161]

$$G(\theta) = \frac{1}{2\mu} \cos^2 \frac{\theta}{2} \left\{ \frac{\kappa + 1}{8} [K_I^2(1 + \cos \theta) - 4K_I K_{II} \sin \theta + K_{II}^2(5 - 3 \cos \theta)] + K_{III}^2 \right\} \quad (4.17)$$

where  $\theta$  denotes the direction angle with respect to the preexisting crack plane,  $\mu$  is the shear modulus, and  $\kappa = 3 - 4\nu$  for plane strain with  $\nu$  being the Poisson's ratio of the material.  $K_i$  represents the stress intensity factor of mode  $i$  ( $i = I, II, III$ ).

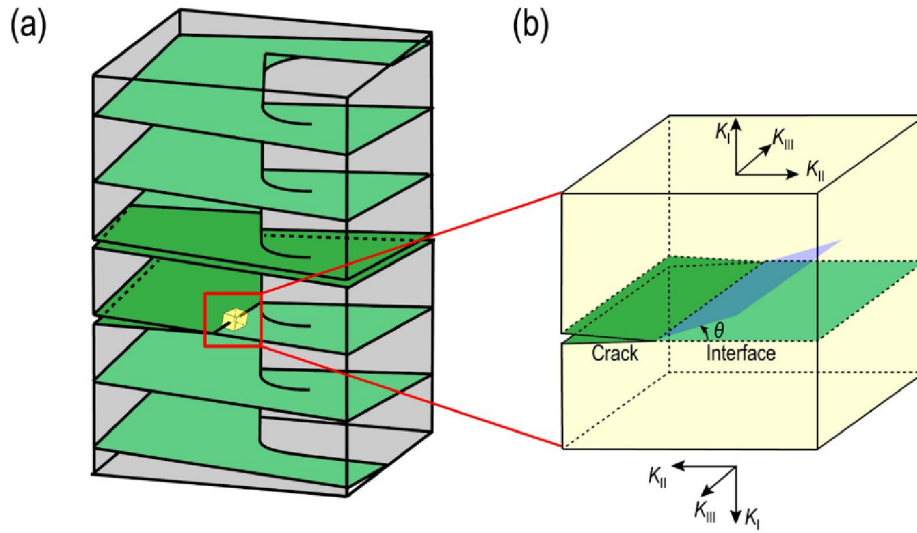


Figure 4.8 The crack frontier of a spiral interface in (a) is equated to a 2D (plane strain) mixed-mode crack shown in (b).

Introduce two *mode ratio angles* defined as  $\alpha = \tan^{-1}(K_{II}/K_I)$  and  $\phi = \tan^{-1}(K_{III}/\sqrt{K_I^2 + K_{II}^2})$  to correlate the loadings of different modes. Then the stress intensity factors can be expressed in terms of  $\alpha$  and  $\phi$  as

$$\begin{aligned} K_I &= K_{\text{all}} \cos \alpha \cdot \cos \phi \\ K_{II} &= K_{\text{all}} \sin \alpha \cdot \cos \phi \\ K_{III} &= K_{\text{all}} \sin \phi \end{aligned} \quad (4.18)$$

where  $K_{\text{all}} = \sqrt{K_I^2 + K_{II}^2 + K_{III}^2}$ . Thus, Eq. (4.17) can be rewritten in terms of  $K_{\text{all}}$ ,  $\alpha$  and  $\phi$  as

$$\begin{aligned} G(\theta) &= \left\{ \frac{\kappa+1}{8} \left[ (1+\cos\theta)\cos^2\alpha - 2\sin 2\alpha \sin\theta + \sin^2\alpha(5-3\cos\theta) \right] \cos^2\phi + \sin^2\phi \right\} \\ &\quad \times \frac{K_{\text{all}}^2 \cos^2(\theta/2)}{2\mu} \end{aligned} \quad (4.19)$$

Assume crack propagates along the interface ( $\theta=0$ ). According to the Griffith criterion [162], crack propagation happens when  $K_{\text{all}}$  reaches the critical value  $K_{\text{all-in}}$  satisfying the following condition:

$$G(\alpha, \phi, \theta=0, K_{\text{all-in}}) = \frac{K_{\text{all-in}}^2}{2\mu} \left( \frac{\kappa+1}{4} \cos^2\phi + \sin^2\phi \right) = G_{\text{in}} \quad (4.20)$$

where  $G_{\text{in}}$  represents the fracture toughness of the interface.

If the crack deflects and penetrates into the lamina material, according to the maximum energy release rate criterion [161], the fracture angle  $\theta^*$  is determined by following conditions:

$$\left. \frac{\partial G(\theta)}{\partial \theta} \right|_{\theta=\theta^*} = 0 \quad \left( \text{with } \left. \frac{\partial^2 G(\theta)}{\partial \theta^2} \right|_{\theta=\theta^*} < 0 \right) \quad (4.21)$$

In accordance with the Griffith criterion, crack propagation along  $\theta^*$  direction happens when the load  $K_{\text{all}}$  reaches the critical value  $K_{\text{all-la}}$  satisfying following

condition

$$\begin{aligned}
 & G(\alpha, \phi, \theta^*(\alpha, \phi), K_{\text{all-la}}) \\
 & = \left\{ \frac{\kappa+1}{8} \left[ (1 + \cos\theta^*) \cos^2\alpha - 2\sin 2\alpha \sin\theta^* + \sin^2\alpha (5 - 3\cos\theta^*) \right] \cos^2\phi + \sin^2\phi \right\} \\
 & \quad \times \frac{K_{\text{all-la}}^2 \cos^2(\theta^*/2)}{2\mu} = G_{\text{la}}
 \end{aligned} \tag{4.22}$$

where  $G_{\text{la}}$  represents the fracture toughness of the lamina material. Preference of crack propagation along the interface requires

$$K_{\text{all-in}}^2 / K_{\text{all-la}}^2 < 1 \tag{4.23}$$

Substituting Eqs. (4.20) and (4.22) into (4.23) gives rise to

$$\frac{K_{\text{all-in}}^2}{K_{\text{all-la}}^2} = \frac{G_{\text{in}}}{G_{\text{la}}} \cdot \frac{G(\alpha, \phi, \theta^*(\alpha, \phi))}{G(\alpha, \phi, \theta = 0)} < 1 \tag{4.24}$$

To satisfy the above condition for arbitrary  $\alpha$  and  $\phi$ , the maximum value of function

$$f(\alpha, \phi, \theta^*(\alpha, \phi)) = \frac{G(\alpha, \phi, \theta^*(\alpha, \phi))}{G(\alpha, \phi, \theta = 0)} \tag{4.25}$$

is expected, which can be determined by solving equations

$$\begin{aligned}
 \frac{\partial f}{\partial \alpha} &= f'_\alpha(\alpha, \phi, \theta^*(\alpha, \phi)) + f'_{\theta^*}(\alpha, \phi, \theta^*(\alpha, \phi)) \cdot \frac{\partial \theta^*}{\partial \alpha} = 0 \\
 \frac{\partial f}{\partial \phi} &= f'_\phi(\alpha, \phi, \theta^*(\alpha, \phi)) + f'_{\theta^*}(\alpha, \phi, \theta^*(\alpha, \phi)) \cdot \frac{\partial \theta^*}{\partial \phi} = 0
 \end{aligned} \tag{4.26}$$

Since Eq. (4.21) implies that

$$f'_{\theta^*}(\alpha, \phi, \theta^*(\alpha, \phi)) = \frac{G'_{\theta^*}(\alpha, \phi, \theta^*(\alpha, \phi), K_{\text{all}})}{G(\alpha, \phi, \theta = 0, K_{\text{all}})} = 0 \quad (4.27)$$

Eq. (4.26) can be further simplified to be

$$\begin{aligned} \frac{\partial f}{\partial \alpha} &= f'_{\alpha}(\alpha, \phi, \theta^*(\alpha, \phi)) = 0 \\ \frac{\partial f}{\partial \phi} &= f'_{\phi}(\alpha, \phi, \theta^*(\alpha, \phi)) = 0 \end{aligned} \quad (4.28)$$

Solving Eqs. (4.21) and (4.28) for  $\alpha$ ,  $\phi$  and  $\theta^*$ , we have  $\alpha = 60^\circ$ ,  $\phi = 0^\circ$  and  $\theta^* = -60^\circ$ . The maximum value of function  $f$  thus is given by

$$f_{\text{max}} = f(\alpha = 60^\circ, \phi = 0^\circ, \theta^* = -60^\circ) \approx 1.69 \quad (4.29)$$

Therefore, Eq. (4.24) always holds as long as

$$\frac{G_{\text{in}}}{G_{\text{la}}} < \frac{1}{f_{\text{max}}} \approx 0.6 \quad (4.30)$$

That is, if the ratio of the fracture toughness of the interface to that of the lamina is less than 0.6, crack initiated on the interface will always grow along the interface irrespective of the direction of external loading. The operation of the enhancing mechanism of spiral interface and  $\mu$ -SD thus is ensured.

## 4.5 Summary

In this chapter, the mechanical behavior of  $\mu$ -SD, a type of helical structure in biological laminated composites, was systematically studied. Finite element analysis on an individual  $\mu$ -SD showed that the failure of the  $\mu$ -SD under tension involves the

delamination of the prolonged spiral interface, giving rise to much higher toughness compared to those of the planar counterpart. Moreover, the cooperation of multiple  $\mu$ -SDs was investigated by studying the effect of  $\mu$ -SD density on the mechanical reinforcement. It was found that the reinforcing effect was highly dependent on the density of  $\mu$ -SDs. Theoretical modelling was further performed to predict the mechanical behaviors of  $\mu$ -SD under uniaxial tension, which are well consistent with the FE analysis. The operation of such reinforcing mechanism of  $\mu$ -SD requires the delamination of spiral interface, which is not spontaneous but conditional. Theoretical analysis revealed that the proclivity of crack propagation along the spiral interface can be ensured if the fracture toughness of the interface is less than 60% of that of the matrix material. These findings not only uncover the reinforcing mechanisms of the  $\mu$ -SDs in biological materials but also imply promising application of  $\mu$ -SDs in reinforcing the synthetic laminated composites in engineering.



## **Chapter 5. Homogenizing interfacial shear stress in bi-materials via thickness gradient**

Interfaces in bi-materials such as film-substrate systems are often subjected to shear stress due to the distinct deformation responses of two bonded materials to the external stimuli such as mechanical loading, change of temperature or humidity, or variation of internal structure induced by for example phase transformation. The distribution of such shear stress over the interface normally exhibits high concentration, which tends to initiate crack and evoke interface delamination. In such a crack propagation-mediated process of failure, the load-carrying capacity of interface has not been fully exerted as most of the interface bears little stress. To enhance the interface's resistance to delamination in bi-materials, homogenizing interfacial shear stress becomes a matter of necessity.

Over the past few decades, a lot of efforts have been devoted to the study on interfacial stress in bi-materials, yielding various strategies for homogenizing interfacial stress. For example, by moderating the transition slope of mechanical property across the interface between coating and substrate, functionally graded materials (FGM) were found effective in mitigating the stress concentration on the interface [97]. Moreover, materials with designed gradient in elasticity were also found to homogenize distribution of adhesion stress between materials and therefore enhance the adhesion strength [95]. In addition to FGM, size reduction is an

alternative approach to mitigating the concentration of adhesion stress mediated by intermolecular interactions between two contacting surfaces [83, 92]. It is noteworthy that the interfacial stress in bi-materials caused by strain misfit is shearing-dominant while the adhesion between two contacting surfaces is primarily normal traction. For the inter-surface adhesion, previous study indicated that the traction distribution over the contacting region can also be homogenized by optimizing the profile shapes of the surfaces [83, 84]. Whether such strategy of shape optimization is capable of homogenizing the shear stress caused by strain misfit in bi-materials remains an open question. In this chapter, theoretical analysis will be carried out to explore the feasibility of shape/geometry optimization as a novel strategy to homogenize the interfacial shear stress in bi-materials. Two sorts of bi-material systems will be considered, including continuous film on disk-like substrate and island film on half-space substrate. Our objective is to find the optimal design of the film thickness in each case, whereby the shear stress induced by strain misfit between the film and substrate, if developed, is uniformly distributed over the whole interface.

## **5.1 Theoretical modelling**

### **5.1.1 Continuous film on disk-like substrate**

We first consider a bi-material consisting of a continuous thin-film coating perfectly bonded on a disk-like substrate with radius  $R$  and thickness  $t_s$ , as

schematically shown in Figure 5.1(a). The thickness of the film, which may not necessarily be uniform, is to be determined to achieve such an optimal scenario that uniform shear stress ( $\tau_{de}$ ) is developed over the interface upon strain misfit ( $\epsilon_{mis}$ ) in between them. In other words, if such optimal thickness profile of the film, designated as  $t_f(r)$ , is found and adopted, the shear stress on the interface should be uniform and equal to  $\tau_{de}$ . Determination of  $t_f(r)$  can be made based on the equilibrium conditions and deformation compatibility between the film and substrate, as illustrated below. Such reverse approach for problem solving will also be applied to find the optimal thickness profile for other bi-material configurations.

Figure 5.1(b) and (c) show the free body diagrams of infinitesimal elements in the substrate and film, respectively. For the substrate, equilibrium condition along the radial direction requires

$$\frac{\partial \sigma_r^{(s)}}{\partial r} + \frac{\sigma_r^{(s)} - \sigma_\theta^{(s)}}{r} + \frac{\tau_{de}}{t_s} = 0 \quad (5.1)$$

where  $\sigma_r^{(s)}$  and  $\sigma_\theta^{(s)}$  denote the normal stresses along the radial and circumferential directions, respectively. In Eq. (5.1), variables with super- or subscript 's' pertain to the substrate.

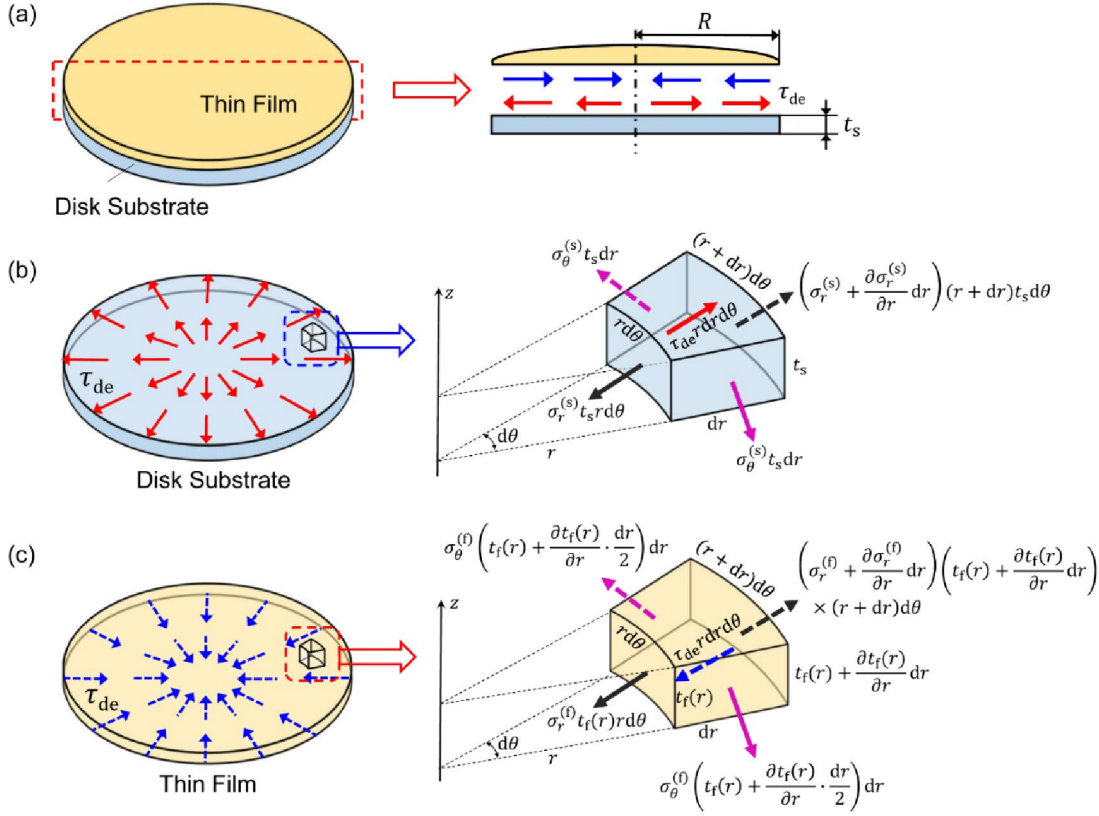


Figure 5.1 (a) Schematics of a bi-material consisting of a circular film on a disk-like substrate. The nonuniform thickness of the film is to be determined so that the interfacial shear stress induced by strain misfit, if available, is uniform and equal to  $\tau_{de}$ . Here, the direction of the shear stress plotted is based on the assumption that  $\varepsilon_{\theta 0} > \varepsilon_{s0}$ . If  $\varepsilon_{\theta 0} < \varepsilon_{s0}$ , the direction of the shear stress should be opposite or  $\tau_{de} < 0$ . (b, c) Free body diagrams of infinitesimal elements in the substrate and film, respectively.

For an axisymmetric problem, the normal strains in the substrate can be expressed in terms of displacement as

$$\varepsilon_r^{(s)} = \frac{\partial u_r^{(s)}}{\partial r}, \quad \varepsilon_\theta^{(s)} = \frac{u_r^{(s)}}{r} \quad (5.2)$$

where  $u_r^{(s)}$  denotes the radial displacement of the substrate. Eq. (5.2) implies an important correlation between  $\varepsilon_r^{(s)}$  and  $\varepsilon_\theta^{(s)}$ , namely

$$\varepsilon_r^{(s)} = \varepsilon_\theta^{(s)} + r \cdot \frac{\partial \varepsilon_\theta^{(s)}}{\partial r} \quad (5.3)$$

The total strain of the substrate contains two parts. One is the intrinsic, equiaxed strain ( $\varepsilon_{s0}$ ) caused by volume change due to factors such as thermal expansion, phase transformation or moisture absorption. The other is the strain caused by stress applied on it. This part of strain can be calculated by Hooke's law if the materials are elastic as we assume here. Therefore, strains of the substrate in the radial and circumferential directions are given by

$$\varepsilon_r^{(s)} = \frac{1}{E_s} (\sigma_r^{(s)} - \nu_s \sigma_\theta^{(s)}) + \varepsilon_{s0}, \quad \varepsilon_\theta^{(s)} = \frac{1}{E_s} (\sigma_\theta^{(s)} - \nu_s \sigma_r^{(s)}) + \varepsilon_{s0} \quad (5.4)$$

where  $E_s$  and  $\nu_s$  stand for the Young's modulus and Poisson's ratio of the substrate, respectively. In Eq. (5.4), the normal stress along  $z$  direction is neglected due to the thin thickness and free surface of the substrate. Rearrangement of Eq. (5.4) yields the stresses in terms of strains as

$$\sigma_r^{(s)} = \frac{E_s}{1-\nu_s^2} (\varepsilon_r^{(s)} + \nu_s \varepsilon_\theta^{(s)}) - \frac{E_s \varepsilon_{s0}}{1-\nu_s}, \quad \sigma_\theta^{(s)} = \frac{E_s}{1-\nu_s^2} (\varepsilon_\theta^{(s)} + \nu_s \varepsilon_r^{(s)}) - \frac{E_s \varepsilon_{s0}}{1-\nu_s} \quad (5.5)$$

Substituting Eq. (5.3) into Eq. (5.5) to eliminate  $\varepsilon_r^{(s)}$  leads to

$$\sigma_r^{(s)} = \frac{E_s}{1-\nu_s} \cdot (\varepsilon_\theta^{(s)} - \varepsilon_{s0}) + \frac{E_s r}{1-\nu_s^2} \cdot \frac{\partial \varepsilon_\theta^{(s)}}{\partial r}, \quad \sigma_\theta^{(s)} = \frac{E_s}{1-\nu_s} \cdot (\varepsilon_\theta^{(s)} - \varepsilon_{s0}) + \frac{E_s \nu_s r}{1-\nu_s^2} \cdot \frac{\partial \varepsilon_\theta^{(s)}}{\partial r} \quad (5.6)$$

Inserting Eq. (5.6) into Eq. (5.1), the equilibrium equation can be rewritten in terms of

circumferential strain  $\varepsilon_\theta^{(s)}$  as

$$r \cdot \frac{\partial^2 \varepsilon_\theta^{(s)}}{\partial r^2} + 3 \cdot \frac{\partial \varepsilon_\theta^{(s)}}{\partial r} + \frac{\tau_{de}(1-\nu_s^2)}{E_s t_s} = 0 \quad (5.7)$$

Solving Eq. (5.7) for  $\varepsilon_\theta^{(s)}$  yields

$$\varepsilon_\theta^{(s)} = -\frac{\tau_{de}(1-\nu_s^2)}{3E_s t_s} \cdot r + C_1$$

where constant  $C_1$ , according to Eq. (5.6) and boundary condition of  $\sigma_r^{(s)}|_{r=R} = 0$ , is

determined as  $C_1 = \varepsilon_{s0} + \frac{(2+\nu_s)(1-\nu_s)\tau_{de}R}{3E_s t_s}$ . Consequently, the circumferential strain

$\varepsilon_\theta^{(s)}$  is given by

$$\varepsilon_\theta^{(s)} = k \cdot r + b + \varepsilon_{s0} \quad (5.8)$$

where  $k \equiv -\frac{\tau_{de}(1-\nu_s^2)}{3E_s t_s}$ , and  $b \equiv \frac{(2+\nu_s)(1-\nu_s)\tau_{de}R}{3E_s t_s}$ .

On the other hand, for the thin film, force equilibrium along the radial direction (see Figure 5.1(c) for the free body diagram) implies

$$\frac{\partial \sigma_r^{(f)}}{\partial r} \cdot t_f(r) + \sigma_r^{(f)} \cdot \frac{\partial t_f(r)}{\partial r} + \frac{(\sigma_r^{(f)} - \sigma_\theta^{(f)})t_f(r)}{r} - \tau_{de} = 0 \quad (5.9)$$

where  $\sigma_r^{(f)}$  and  $\sigma_\theta^{(f)}$  represent the normal stresses along the radial and circumferential directions respectively. In Eq. (5.9), variables with super- or subscript ‘f’ pertain to the film. The opposite signs of  $\tau_{de}$  in Eqs. (5.9) and (5.1) are due to the opposite direction of the shear stresses applied on the film and substrate.

Similarly, for this axisymmetric problem, the normal strains in the film can be expressed in terms of displacement as

$$\varepsilon_r^{(f)} = \frac{\partial u_r^{(f)}}{\partial r}, \quad \varepsilon_\theta^{(f)} = \frac{u_r^{(f)}}{r} \quad (5.10)$$

where  $u_r^{(f)}$  denotes the radial displacement of the film. According to Eq. (5.10), the correlation between  $\varepsilon_r^{(f)}$  and  $\varepsilon_\theta^{(f)}$  can be written as

$$\varepsilon_r^{(f)} = \varepsilon_\theta^{(f)} + r \cdot \frac{\partial \varepsilon_\theta^{(f)}}{\partial r} \quad (5.11)$$

Likewise, the total strain of the film contains both volume change-induced intrinsic, equiaxed strain ( $\varepsilon_{f0}$ ) and the strain caused by stress applied on it. Therefore, strains of the film in the radial and circumferential directions are given by

$$\varepsilon_r^{(f)} = \frac{1}{E_f} (\sigma_r^{(f)} - \nu_f \sigma_\theta^{(f)}) + \varepsilon_{f0}, \quad \varepsilon_\theta^{(f)} = \frac{1}{E_f} (\sigma_\theta^{(f)} - \nu_f \sigma_r^{(f)}) + \varepsilon_{f0} \quad (5.12)$$

where  $E_f$  and  $\nu_f$  represent the Young's modulus and Poisson's ratio of the film, respectively. In Eq. (5.12), the normal stress along  $z$  direction is also neglected due to the thin thickness and free surface of the film. Rearrangement of Eq. (5.12) yields the stresses in terms of strains as

$$\sigma_r^{(f)} = \frac{E_f}{1-\nu_f^2} (\varepsilon_r^{(f)} + \nu_f \varepsilon_\theta^{(f)}) - \frac{E_f \varepsilon_{f0}}{1-\nu_f}, \quad \sigma_\theta^{(f)} = \frac{E_f}{1-\nu_f^2} (\varepsilon_\theta^{(f)} + \nu_f \varepsilon_r^{(f)}) - \frac{E_f \varepsilon_{f0}}{1-\nu_f} \quad (5.13)$$

Substituting Eq. (5.11) into Eq. (5.13) to eliminate  $\varepsilon_r^{(f)}$  leads to

$$\sigma_r^{(f)} = \frac{E_f}{1-\nu_f} \cdot (\varepsilon_\theta^{(f)} - \varepsilon_{\theta 0}) + \frac{E_f r}{1-\nu_f^2} \cdot \frac{\partial \varepsilon_\theta^{(f)}}{\partial r}, \quad \sigma_\theta^{(f)} = \frac{E_f}{1-\nu_f} \cdot (\varepsilon_\theta^{(f)} - \varepsilon_{\theta 0}) + \frac{E_f \nu_f r}{1-\nu_f^2} \cdot \frac{\partial \varepsilon_\theta^{(f)}}{\partial r} \quad (5.14)$$

Assume that the film and substrate are perfectly bonded during deformation. No slip between them implies that  $u_r^{(f)} = u_r^{(s)}$  or  $\varepsilon_\theta^{(f)} = \varepsilon_\theta^{(s)}$  on the interface. Substituting  $\varepsilon_\theta^{(f)} = \varepsilon_\theta^{(s)} = k \cdot r + b + \varepsilon_{s0}$  into Eq. (5.14), we have

$$\sigma_r^{(f)} = \frac{E_f(kr + b + \varepsilon_{s0} - \varepsilon_{\theta 0})}{1-\nu_f} + \frac{E_f kr}{1-\nu_f^2}, \quad \sigma_\theta^{(f)} = \frac{E_f(kr + b + \varepsilon_{s0} - \varepsilon_{\theta 0})}{1-\nu_f} + \frac{E_f \nu_f kr}{1-\nu_f^2} \quad (5.15)$$

Defining strain misfit between the film and substrate as  $\varepsilon_{\text{mis}} \equiv \varepsilon_{\theta 0} - \varepsilon_{s0}$ , Eq. (5.15)

thus can be rewritten as

$$\sigma_r^{(f)} = \frac{E_f(kr + b - \varepsilon_{\text{mis}})}{1-\nu_f} + \frac{E_f kr}{1-\nu_f^2}, \quad \sigma_\theta^{(f)} = \frac{E_f(kr + b - \varepsilon_{\text{mis}})}{1-\nu_f} + \frac{E_f \nu_f kr}{1-\nu_f^2} \quad (5.16)$$

From Eq. (5.16), it is easy to see that the radial normal stress  $\sigma_r^{(f)}$  in the thin film increases linearly from the center to the edge. This distribution of the normal stress is quite different from the uniform-thickness case, in which the radial normal stress is almost uniform along the radial direction. For the gradient thin film, therefore, failure such as fracture or buckling is prone to happen near the edge.

Inserting Eq. (5.16) into Eq. (5.9), the equilibrium equation becomes

$$\frac{\partial t_f(r)}{\partial r} + \frac{3k \cdot t_f(r)}{(2 + \nu_f)kr + (b - \varepsilon_{\text{mis}})(1 + \nu_f)} - \frac{\tau_{\text{de}}(1 - \nu_f^2)/E_f}{(2 + \nu_f)kr + (b - \varepsilon_{\text{mis}})(1 + \nu_f)} = 0 \quad (5.17)$$

Solving Eq. (5.17) for  $t_f(r)$  gives rise to

$$t_f(r) = C_2 \left[ (2 + \nu_f)kr + (b - \varepsilon_{\text{mis}})(1 + \nu_f) \right]^{\frac{3}{2 + \nu_f}} + \frac{\tau_{\text{de}}(1 - \nu_f^2)}{3kE_f}$$

where  $C_2$  is a constant to be determined. Stress-free condition at the edge of the film requires

$$\sigma_r^{(f)} \Big|_{r=R} = \frac{E_f}{1 - \nu_f} \cdot \left[ \frac{(1 - \nu_s)\tau_{\text{de}}R}{3E_s t_s} - \varepsilon_{\text{mis}} \right] - \frac{\tau_{\text{de}}E_f R(1 - \nu_s^2)}{3E_s t_s(1 - \nu_f^2)} = 0 \quad (5.18)$$

As the intrinsic strains of the film and substrate  $\varepsilon_{f0}$  and  $\varepsilon_{s0}$  represent their deformation at stress-free state, the interfacial stress should affect their deformation in an either positive or negative way, depending on the direction of the interfacial stress. Without loss of generality, we assume that  $\varepsilon_{f0} > \varepsilon_{s0}$  or  $\varepsilon_{\text{mis}} \equiv \varepsilon_{f0} - \varepsilon_{s0} > 0$ . Such strain misfit causes opposite shear tractions on the film and substrate as shown in Figure 5.1(a), resulting in contracting and expanding additional displacements in the film and substrate, respectively. Since  $\varepsilon_\theta = u_r/r$ , we have  $\varepsilon_{f0} > \varepsilon_\theta^{(f)} = \varepsilon_\theta^{(s)} > \varepsilon_{s0}$ , which implies  $\varepsilon_\theta^{(s)} - \varepsilon_{s0} < \varepsilon_{f0} - \varepsilon_{s0} = \varepsilon_{\text{mis}}$ . Recalling Eq. (5.8), we have

$$0 < \frac{\tau_{\text{de}}}{\varepsilon_{\text{mis}}} < \frac{3E_s t_s}{(\nu_s + 2)(1 - \nu_s)R} \quad (5.19)$$

which unveils the implicit upper limit of the ratio of  $\tau_{\text{de}}/\varepsilon_{\text{mis}}$  in the design. This limit also exists in the case with  $\varepsilon_{f0} < \varepsilon_{s0}$ . Eq. (5.19) implies that  $\sigma_r^{(f)} \Big|_{r=R} \neq 0$ , namely the boundary condition of Eq. (5.18) is unrealistic and can hardly be satisfied. Alternatively, a weak-form boundary condition is thus proposed that the radial force per unit length  $\sigma_r^{(f)}t_f$  or  $t_f$ , rather than stress  $\sigma_r^{(f)}$ , vanishes at the edge  $r=R$ . In

doing so, constant  $C_2$  is determined as

$$C_2 = -\frac{\tau_{de}(1-\nu_f^2)}{3kE_f} \cdot [(2+\nu_f)kR + (b-\varepsilon_{mis})(1+\nu_f)]^{\frac{3}{2+\nu_f}}$$

Eventually, the analytical solution to the optimal thickness profile is given by

$$t_f(r) = \frac{E_s t_s (1-\nu_f^2)}{E_f (1-\nu_s^2)} \left\{ \frac{\left[ (\nu_f+2)(1-\nu_s^2) + \left[ \frac{3E_s t_s \varepsilon_{mis}}{R \tau_{de}} - (\nu_s+2)(1-\nu_s) \right] (\nu_f+1) \right]^{\frac{3}{\nu_f+2}}}{(\nu_f+2)(1-\nu_s^2) \cdot \frac{r}{R} + \left[ \frac{3E_s t_s \varepsilon_{mis}}{R \tau_{de}} - (\nu_s+2)(1-\nu_s) \right] (\nu_f+1)} - 1 \right\} \quad (5.20)$$

By taking  $E_f=100$  GPa,  $\nu_f=0.3$ ,  $E_s=200$  GPa,  $\nu_s=0.25$ ,  $R=10$  mm,  $t_s=10$   $\mu\text{m}$ ,  $\varepsilon_{mis}=1\%$  and  $\tau_{de}=1$  MPa, the thickness profile of the nonuniform film given above is plotted in Figure 5.2(a), which appears like a cone.

Finite element analysis was carried out to examine the shear stress developed on the interface between a film with thickness given by Eq. (5.20) and a disk-like substrate. In simulation, both the film and substrate were depicted as linear elastic materials, while the interface between them was modelled by zero-thickness cohesive element. The intrinsic strain was equivalently implemented by thermal expansion with expansion coefficient misfit between the film and substrate taken as  $\varepsilon_{mis}$ . The simulated results at different levels of strain misfit, which were implemented by applying different temperature increments, are displayed in Figure 5.2(b). As expected, the shear stress, except that in the vicinity of the central symmetric point, displays a

uniform distribution over the interface. The magnitude of the uniform shear stress is linearly proportional to the applied strain misfit with slope being  $\tau_{de}/\varepsilon_{mis}$ , which stands for the shear stress developed by unit strain misfit.

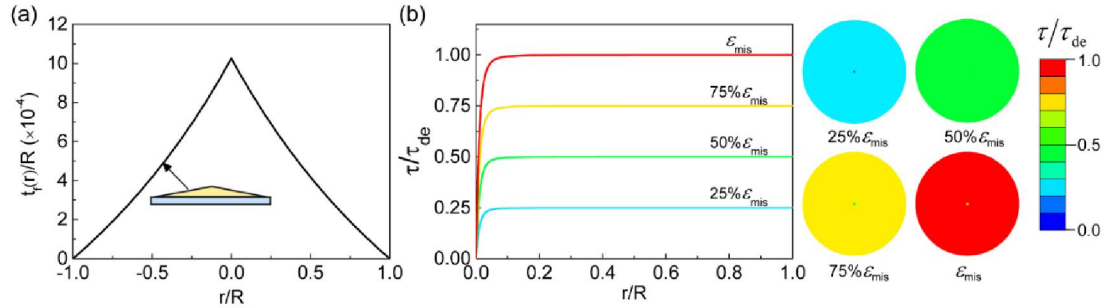


Figure 5.2 (a) Profile of the optimal gradient film thickness. (b) The simulated shear stress field on the interface between the thin film and substrate at different degrees of strain misfit. Parameters adopted:  $E_f=100$  GPa,  $\nu_f=0.3$ ,  $E_s=200$  GPa,  $\nu_s=0.25$ ,  $R=10$  mm,  $t_s=10$   $\mu$ m,  $\varepsilon_{mis}=1\%$  and  $\tau_{de}=1$  MPa. The stiffness of the cohesive interface is taken as 100 GPa/mm.

It is worth pointing out that in the above analysis, the bending effect has not been taken into account since in many cases of bi-material, such as the electrode-current collector system in lithium-ion batteries, the out-of-plane deformation is firmly constrained. But for free-standing bi-materials, the strain misfit would result in curved configuration which in return affects the interfacial shear stress distribution. In that case, the above solution to the optimal gradient thickness for homogenizing the shear stress may not be applicable anymore. Separate analysis is needed to shed light on the effect of bending on the interfacial shear stress distribution.

### 5.1.2 Island film on half-space substrate

Above solution to the optimal thickness profile applies to bi-material systems in

which the film continuously and fully covers the substrate. In some circumstances, however, film and substrate may have quite distinct sizes in plane and/or thickness. Examples include discontinuous wear-resistant coating on cutting tools [163-166] and silicon islands on current collector in electrodes of lithium-ion batteries [91, 167-169]. To extend our conception of stress homogenization to these cases, we keep on exploring the optimal thickness profile for an island film attached on a half-space substrate, as schematically shown in Figure 5.3(a). Similarly, we designate the optimal thickness profile of the film as  $t_f(r)$ , whereby uniform shear stress  $\tau_{de}$  is developed over the interface when strain misfit of  $\varepsilon_{mis}$  takes place between the film and substrate. The determination of function  $t_f(r)$  is made as follows.

For the half-space substrate, when a uniform shear stress with magnitude of  $\tau_{de}$  is applied over a circular region of radius  $R$  (see Figure 5.3(b)), the resulting radial displacement in this region is given by [170]

$$u_r^{(s)}(r) = \frac{4R^2 \tau_{de} (1 - \nu_s^2)}{E_s \pi r} \int_0^{r/R} \frac{\lambda^2 \cdot [\ln(1 + \sqrt{1 - \lambda^2}) - \ln \lambda]}{\sqrt{(r/R)^2 - \lambda^2}} d\lambda$$

where  $E_s$  and  $\nu_s$  represent the Young's modulus and Poisson's ratio of the substrate, respectively. Here, super- and subscript 's' pertain to the substrate. The corresponding circumferential strain is given by

$$\tilde{\varepsilon}_\theta^{(s)} = \frac{u_r^{(s)}}{r} = \frac{4R^2 \tau_{de} (1 - \nu_s^2)}{E_s \pi r^2} \int_0^{r/R} \frac{\lambda^2 \cdot [\ln(1 + \sqrt{1 - \lambda^2}) - \ln \lambda]}{\sqrt{(r/R)^2 - \lambda^2}} d\lambda$$

Thus, the total circumferential strain, including the intrinsic portion, can be expressed

as

$$\varepsilon_{\theta}^{(s)} = \varepsilon_{s0} + \tilde{\varepsilon}_{\theta}^{(s)} = \varepsilon_{s0} + \frac{4R^2 \tau_{de} (1 - \nu_s^2)}{E_s \pi r^2} \int_0^{r/R} \frac{\lambda^2 \cdot [\ln(1 + \sqrt{1 - \lambda^2}) - \ln \lambda]}{\sqrt{(r/R)^2 - \lambda^2}} d\lambda \quad (5.21)$$

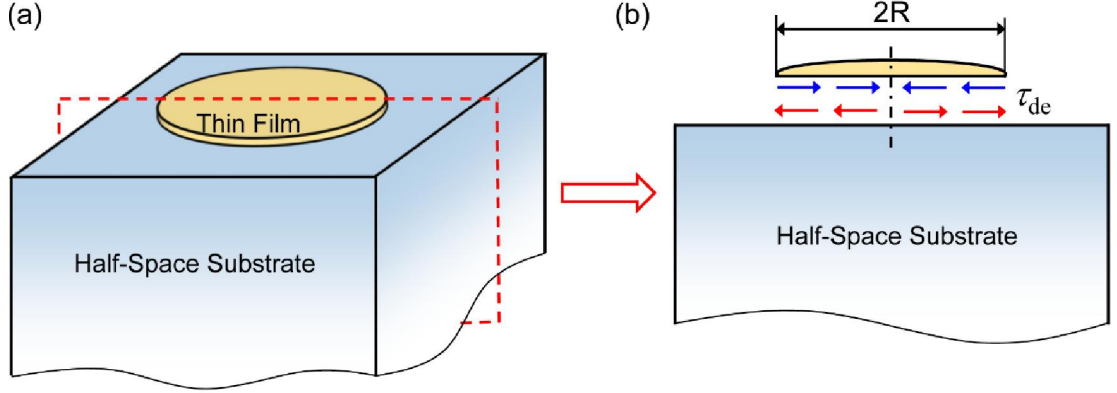


Figure 5.3 (a) Schematics of a bi-material consisting of a circular island film on a half-space substrate. The thickness of the film is to be optimized so that the interfacial shear stress induced by strain misfit, if available, is uniform and equal to  $\tau_{de}$  as shown in (b).

For the circular island film, Eqs. (5.9) and (5.14) still apply. We therefore have

$$\frac{\partial \sigma_r^{(f)}}{\partial r} \cdot t_f(r) + \sigma_r^{(f)} \cdot \frac{\partial t_f(r)}{\partial r} + \frac{(\sigma_r^{(f)} - \sigma_{\theta}^{(f)}) t_f(r)}{r} - \tau_{de} = 0 \quad (5.22)$$

$$\sigma_r^{(f)} = \frac{E_f}{1 - \nu_f} \cdot (\varepsilon_{\theta}^{(f)} - \varepsilon_{\theta 0}) + \frac{E_f r}{1 - \nu_f^2} \cdot \frac{\partial \varepsilon_{\theta}^{(f)}}{\partial r}, \quad \sigma_{\theta}^{(f)} = \frac{E_f}{1 - \nu_f} \cdot (\varepsilon_{\theta}^{(f)} - \varepsilon_{\theta 0}) + \frac{E_f \nu_f r}{1 - \nu_f^2} \cdot \frac{\partial \varepsilon_{\theta}^{(f)}}{\partial r} \quad (5.23)$$

Assuming that the island film and substrate are perfectly bonded during deformation, we have  $\varepsilon_{\theta}^{(f)} = \varepsilon_{\theta}^{(s)} = \tilde{\varepsilon}_{\theta}^{(s)} + \varepsilon_{s0}$ . Substitution of this relationship into Eq. (5.23) to eliminate  $\varepsilon_{\theta}^{(f)}$  gives

$$\begin{aligned}\sigma_r^{(f)} &= \frac{E_f}{1-\nu_f} \cdot (\tilde{\varepsilon}_\theta^{(s)} - \varepsilon_{\text{mis}}) + \frac{E_f r}{1-\nu_f^2} \cdot \frac{\partial \tilde{\varepsilon}_\theta^{(s)}}{\partial r} \\ \sigma_\theta^{(f)} &= \frac{E_f}{1-\nu_f} \cdot (\tilde{\varepsilon}_\theta^{(s)} - \varepsilon_{\text{mis}}) + \frac{E_f \nu_f r}{1-\nu_f^2} \cdot \frac{\partial \tilde{\varepsilon}_\theta^{(s)}}{\partial r}\end{aligned}\quad (5.24)$$

where  $\varepsilon_{\text{mis}} \equiv \varepsilon_{f0} - \varepsilon_{s0}$ . Substituting Eq. (5.24) into (5.22) yields

$$\frac{\partial t_f(r)}{\partial r} + P(r) \cdot t_f(r) = Q(r) \quad (5.25)$$

where

$$\begin{aligned}P(r) &= \frac{3 \cdot \frac{\partial \tilde{\varepsilon}_\theta^{(s)}}{\partial r} + r \cdot \frac{\partial^2 \tilde{\varepsilon}_\theta^{(s)}}{\partial r^2}}{(1+\nu_f)\tilde{\varepsilon}_\theta^{(s)} + r \cdot \frac{\partial \tilde{\varepsilon}_\theta^{(s)}}{\partial r} - \varepsilon_{\text{mis}}(1+\nu_f)}, \\ Q(r) &= \frac{\tau_{\text{de}}(1-\nu_f^2)/E_f}{(1+\nu_f)\tilde{\varepsilon}_\theta^{(s)} + r \cdot \frac{\partial \tilde{\varepsilon}_\theta^{(s)}}{\partial r} - \varepsilon_{\text{mis}}(1+\nu_f)}\end{aligned}$$

The mathematical complexity of Eq. (5.25) implies the difficulty of finding the analytical solution to the function  $t_f(r)$ . Finite difference method was adopted to solve the equation numerically. For this purpose, the stress-free boundary condition in the film, i.e.,  $\sigma_r^{(f)}|_{r=R} = 0$ , needs to be examined. We denote  $\tilde{\varepsilon}_\theta^{(s)}$  as

$$\tilde{\varepsilon}_\theta^{(s)} = \frac{4\tau_{\text{de}}(1-\nu_s^2)}{E_s \pi} \cdot f(\bar{r}) \quad (5.26)$$

where  $f(\bar{r}) = \frac{1}{\bar{r}^2} \int_0^{\bar{r}} \frac{\lambda^2 \cdot [\ln(1+\sqrt{1-\lambda^2}) - \ln \lambda]}{\sqrt{\bar{r}^2 - \lambda^2}} d\lambda$ ,  $\bar{r} = r/R \in [0,1]$ . Substituting Eq.

(5.26) into Eq. (5.24), we have

$$\sigma_r^{(f)} = \frac{E_f}{1-\nu_f} \cdot \left[ \frac{4\tau_{\text{de}}(1-\nu_s^2)}{E_s \pi} \cdot f(\bar{r}) - \varepsilon_{\text{mis}} \right] + \frac{4\tau_{\text{de}} E_f (1-\nu_s^2)}{E_s \pi (1-\nu_f^2)} \cdot \bar{r} f'(\bar{r})$$

Stress-free boundary condition requires  $\sigma_r^{(f)}|_{\bar{r}=1} = 0$ , that is, when  $\bar{r} = 1$ ,

$$f(\bar{r}) + \frac{1}{1+\nu_f} \cdot \bar{r}f'(\bar{r}) - \frac{\pi E_s \varepsilon_{\text{mis}}}{4\tau_{\text{de}}(1-\nu_s^2)} = 0 \quad (5.27)$$

Since  $f(\bar{r}=1) \approx 0.416$ ,  $\bar{r}f'(\bar{r})|_{(\bar{r} \rightarrow 1)} \rightarrow -\infty$  and  $\frac{\pi E_s \varepsilon_{\text{mis}}}{4\tau_{\text{de}}(1-\nu_s^2)} > 0$ , Eq. (5.27)

cannot be satisfied, namely, the stress-free boundary condition of  $\sigma_r^{(f)} = 0$  at the edge ( $r=R$ ) is unrealistic. Thus, alternative weak-form boundary condition of  $\sigma_r^{(f)}t_f = 0$  or  $t_f = 0$  at  $r=R$  is adopted to determine the profile function  $t_f(r)$ . If we take  $E_f=100$  GPa,  $\nu_f=0.3$ ,  $E_s=200$  GPa,  $\nu_s=0.25$ ,  $R=10$  mm,  $\varepsilon_{\text{mis}}=1\%$  and  $\tau_{\text{de}}=1$  MPa, the calculated solution to the thickness profile of the optimal island film is displayed in Figure 5.4(a). Likewise, finite element analysis was carried out to examine the shear stress distribution over the interface between an island film with thickness profile shown in Figure 5.4(a) and a substrate of sufficiently large size. As shown in Figure 5.4(b), the shear stress on the interface, except that in the area very close to the symmetric center, keeps uniform under different levels of strain misfit with magnitude growing at a rate of  $\tau_{\text{de}}/\varepsilon_{\text{mis}}$ . Therefore, the validity of the numerical result is confirmed.

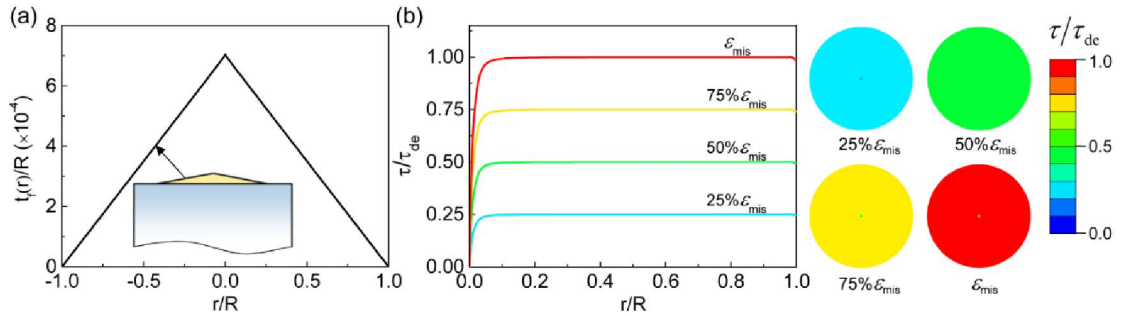


Figure 5.4 (a) Profile of the optimal nonuniform island film thickness. (b) The simulated shear stress field on the interface between the thin film and substrate at different degrees of strain misfit. Parameters adopted:  $E_f=100$  GPa,  $\nu_f=0.3$ ,  $E_s=200$  GPa,  $\nu_s=0.25$ ,  $R=10$  mm,  $\varepsilon_{\text{mis}}=1\%$  and  $\tau_{\text{de}}=1$  MPa. The stiffness of the cohesive interface is taken as 100 GPa/mm.

It is observed from Figure 5.4(a) that  $t_f(r)$  is very close to a linear function, implying the possible presence of a linear approximation of  $t_f(r)$  at least under some proper conditions. Suppose the thickness profile function can be approximated by a linear function as

$$t_f(r) = m(r - R) \quad (5.28)$$

where  $R$  is the radius of the island film and  $m$  is the slope to be determined.

Substituting Eq. (5.28) into Eq. (5.25), we have

$$m = \frac{\tau_{\text{de}}(1 - \nu_f^2)/E_f}{(4r - 3R) \cdot \frac{\partial \tilde{\varepsilon}_\theta^{(s)}}{\partial r} + r(r - R) \cdot \frac{\partial^2 \tilde{\varepsilon}_\theta^{(s)}}{\partial r^2} + (1 + \nu_f) \tilde{\varepsilon}_\theta^{(s)} - \varepsilon_{\text{mis}}(1 + \nu_f)} \quad (5.29)$$

Inserting Eq. (5.26) into Eq. (5.29) to eliminate  $\tilde{\varepsilon}_\theta^{(s)}$  gives

$$m = \frac{E_s(1 - \nu_f^2)/E_f(1 - \nu_s^2)}{g(\bar{r}) - \varphi} \quad (5.30)$$

where

$$g(\bar{r}) = \frac{4}{\pi} [(1 + \nu_f)f(\bar{r}) + (4\bar{r} - 3)f'(\bar{r}) + \bar{r}(\bar{r} - 1)f''(\bar{r})] \quad (5.31a)$$

$$f(\bar{r}) = \frac{1}{\bar{r}^2} \int_0^{\bar{r}} \frac{\lambda^2 \cdot [\ln(1 + \sqrt{1 - \lambda^2}) - \ln \lambda]}{\sqrt{\bar{r}^2 - \lambda^2}} d\lambda \quad (5.31b)$$

$$\varphi \equiv \frac{E_s \varepsilon_{\text{mis}} (1 + \nu_f)}{\tau_{\text{de}} (1 - \nu_s^2)} \quad (5.31c)$$

Numerical integration was adopted to calculate  $f(\bar{r})$  and  $g(\bar{r})$  above. Figure 5.5 shows the calculated variation of  $g(\bar{r})$  with  $\bar{r}$ . As  $\bar{r}$  varies from 0 to 1.0, it can be seen that function  $g(\bar{r})$  takes finite value except in the vicinity of  $\bar{r} = 0$ . Further analysis indicated that as  $\bar{r} \rightarrow 0$ ,  $g(\bar{r})$  asymptotically approaches  $2/\bar{r}$  which is also plotted in Figure 5.5 for comparison. Considering that the Young's modulus of the substrate ( $E_s$ ) is more than 4-5 orders of magnitude higher than the design shear stress ( $\tau_{\text{de}}$ ) and the strain mismatch ( $\varepsilon_{\text{mis}}$ ) is around a few percent, the value of  $\varphi$  in Eq. (5.31c) should be on the order of magnitude of 1000. In most of the region of  $\bar{r} \in [0,1]$ ,  $g(\bar{r}) \ll \varphi$  except in the vicinity of  $\bar{r} = 0$ . Therefore,  $m$  in Eq. (5.30) can be

approximated as a constant of  $m \cong -\frac{\tau_{\text{de}}(1-\nu_f)}{E_f \varepsilon_{\text{mis}}}$ . Therefore, when the

nondimensional parameter  $\varphi = \frac{E_s \varepsilon_{\text{mis}} (1 + \nu_f)}{\tau_{\text{de}} (1 - \nu_s^2)}$  is large enough, the thickness profile

can be approximated by a linear function as

$$t_f(r) \cong \frac{\tau_{\text{de}}(1-\nu_f)}{\varepsilon_{\text{mis}} E_f} (R-r) \quad (5.32)$$

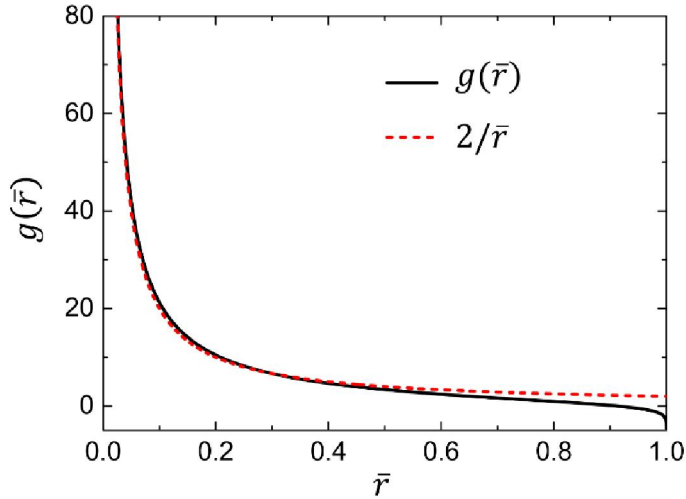


Figure 5.5 Variation of  $g(\bar{r})$  with  $\bar{r}$  in comparison with its asymptotic form of  $2/\bar{r}$ . Here, the Poisson's ratio of the film is taken as  $\nu_f=0.3$ .

which describes a cone with included angle of  $2\arctan\frac{E_f\varepsilon_{\text{mis}}}{\tau_{\text{de}}(1-\nu_f)}$ . It is worth noting that the ratio  $\tau_{\text{de}}/\varepsilon_{\text{mis}}$  in Eq. (5.32) also represents the interfacial shear stress developed by unit strain misfit. The validity of this approximation and its dependence on the nondimensional parameter  $\varphi$  were examined by finite element analysis. Figure 5.6 displays the linear approximations of the optimal thickness profiles (namely Eq. (5.32)) for cases with different  $\varphi$  and the corresponding calculated shear stress distribution on the interface under strain misfit of  $\varepsilon_{\text{mis}}$ . As can be observed, if  $\varphi$  is on the order of magnitude of  $10^3$  or above, the stress field, except that in the vicinity of the central symmetric point, is uniform throughout the interface. When  $\varphi$  is on the order of magnitude of  $10^2$  or below, the stress field exhibits nonuniform distribution, implying the significant deviation of Eq. (5.32) from the actual solution to the optimal thickness.

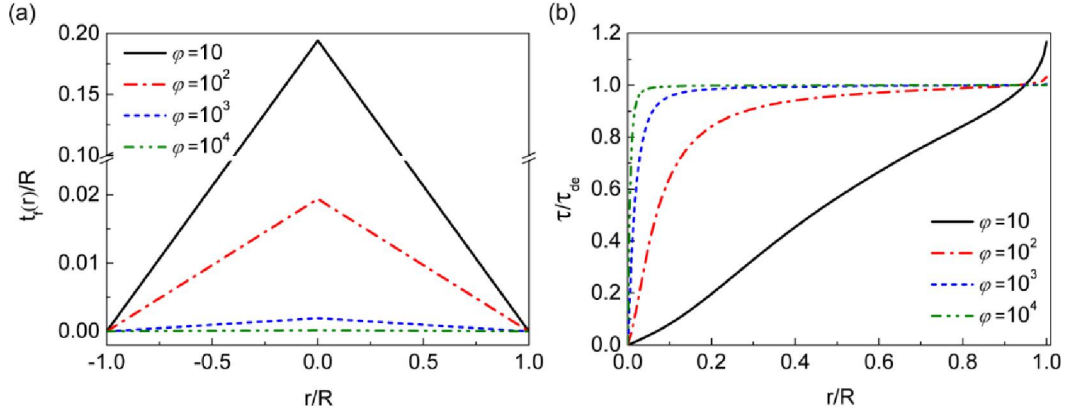


Figure 5.6 (a) Linear approximations of the optimal thickness profiles of island film for different  $\phi$ . (b) The simulated shear stress field on the interface between the island film and substrate under the strain misfit  $\varepsilon_{\text{mis}}$ . Here,  $E_f=100$  GPa,  $\nu_f=0.3$ ,  $E_s=200$  GPa,  $\nu_s=0.25$ ,  $R=10$  mm,  $\varepsilon_{\text{mis}}=1\%$  and  $\tau_{de}=0.277, 2.773, 27.733$  or  $277.333$  MPa. The stiffness of the cohesive interface is taken as 100 GPa/mm.

### 5.1.3 Solutions to plane-strain configurations

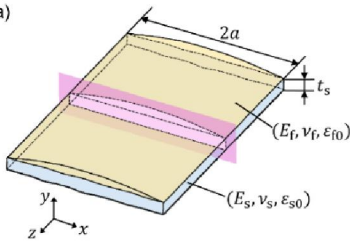
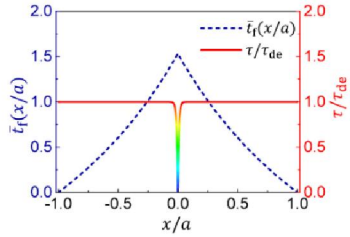
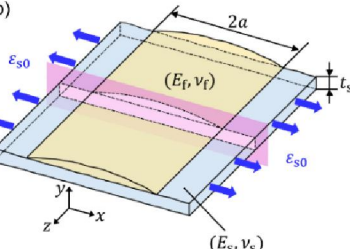
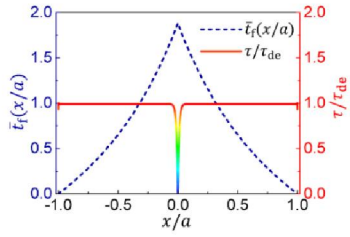
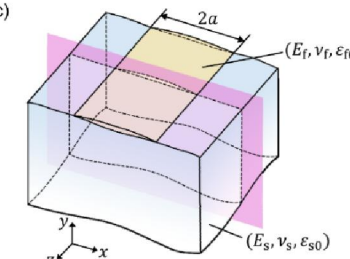
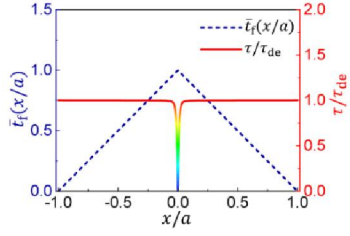
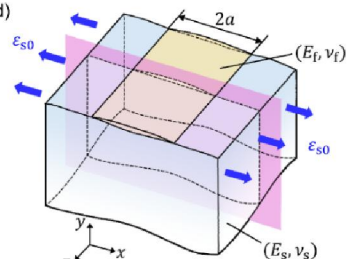
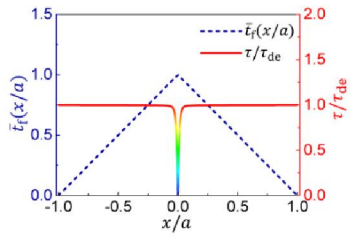
In addition to the above axisymmetric configurations of bi-material, thin film strips bonded on substrate have also been widely used. Typical examples include metal conduction lines in microelectronic devices [171] and optical waveguides in photonic devices [171]. To tackle the stress concentration problem in these configurations, we further extend our study to the configuration of a thin film strip attached on a substrate (see Table 5.1), where plane-strain condition prevails. Similarly, we aim to find the optimal thickness profile  $t_f(x)$  for the film strips, whereby a uniform shear stress field  $\tau_{de}$  will be developed on the interface when strain misfit  $\varepsilon_{\text{mis}}$  takes place between them.

The approach to solving  $t_f(x)$  for the plane-strain configurations is similar to that applied in the preceding axisymmetric cases. Firstly, we need to determine the

strain field of the substrate  $\varepsilon_x^{(s)}$  which can be obtained based on equilibrium conditions or by referring to existing solutions in contact mechanics [170]. Then with the assumption that film and substrate are perfectly bonded, the strain field in the film ( $\varepsilon_x^{(f)}$ ) and substrate ( $\varepsilon_x^{(s)}$ ) should be equal. Knowing the strain field in the film  $\varepsilon_x^{(f)}$ , the film thickness  $t_f(x)$  can be determined based on equilibrium conditions. This method was repeatedly used here to determine the optimal film thickness under different plane-strain configurations.

Table 5.1 lists the analytical solutions to  $t_f(x)$  (in normalized form) for different plane-strain configurations. Case (a) describes a bi-material consisting of a strip film and substrate which have comparable sizes in plane and thickness. The film and substrate have different intrinsic deformation. In case (b), no intrinsic deformation occurs in the film, while the substrate deforms along transverse direction under uniaxial loading. Both cases (c) and (d) depict a strip film attached on a half-space substrate. In case (c), the film and half-space substrate have different intrinsic deformation, while in case (d) only the substrate deforms due to the external mechanical loading along the transverse direction. For each case, the theoretical solution to the optimal thickness of the film was well verified via finite element simulation, as shown in Table 5.1. It is worth pointing out that the solutions for cases (c) and (d) provided in Table 5.1 are the asymptotic solutions under conditions as indicated.

Table 5.1 The optimal film thickness for different plane-strain configurations

Plane-strain configuration	Analytical solution to $t_f(x)$	Profile of optimal thickness of the film and shear stress distribution*
(a) 	$\bar{t}_f(x/a) = \frac{t_f(x)}{a} \cdot \frac{E_f[(1+v_f)\epsilon_{f0} - (1+v_s)\epsilon_{s0}]}{\tau_{de}(1-v_f^2)}$ $= \frac{1}{\frac{1-x/a}{E_s t_s} - \frac{\alpha \tau_{de}(1-v_s^2)}{E_s t_s [(1+v_f)\epsilon_{f0} - (1+v_s)\epsilon_{s0}]}}$	
(b) 	$\bar{t}_f(x/a) = \frac{t_f(x)}{a} \cdot \frac{\epsilon_{s0} E_f}{(-\tau_{de})(1-v_f^2)}$ $= \frac{1}{\frac{1-x/a}{E_s t_s} + \frac{\alpha \tau_{de}(1-v_s^2)}{E_s t_s \epsilon_{s0}}}$	
(c) 	Asymptotic solution to $\bar{t}_f(x/a)$ as $\frac{E_s[(1+v_f)\epsilon_{f0} - (1+v_s)\epsilon_{s0}]}{\tau_{de}(1-v_f^2)} \rightarrow \infty$ : $\bar{t}_f(x/a) = \frac{t_f(x)}{a} \cdot \frac{E_f[(1+v_f)\epsilon_{f0} - (1+v_s)\epsilon_{s0}]}{\tau_{de}(1-v_f^2)} \cong 1 - x/a$	
(d) 	Asymptotic solution to $\bar{t}_f(x/a)$ as $\frac{E_s \epsilon_{s0}}{(-\tau_{de})(1-v_s^2)} \rightarrow \infty$ : $\bar{t}_f(x/a) = \frac{t_f(x)}{a} \cdot \frac{\epsilon_{s0} E_f}{(-\tau_{de})(1-v_f^2)} \cong 1 - x/a$	

\*Profiles of optimal thickness of the film and corresponding simulation results are taken as examples with parameters adopted as follows:  $E_f = 100$  GPa,  $v_f = 0.3$ ,  $E_s = 200$  GPa,  $v_s = 0.25$ ,  $a = 10$  mm,  $t_s = 10$   $\mu$ m,  $\epsilon_{s0} = 1\%$ ,  $\epsilon_{f0} = 2\%$ ,  $\tau_{de} = 1$  MPa for (a)(c) and  $\tau_{de} = -1$  MPa for (b)(d). The cohesive interface stiffness is taken as 100 GPa/mm.

## 5.2 Experimental validation

The preceding section gives the theoretical solutions to the optimal film thickness, whereby the shear stress field on the interface of bi-material is expected to be homogenized. In this section, experimental validation of this strategy was carried

out. For the sake of simplicity, we choose the plane-strain configuration displayed in Table 5.1(b) for illustration, namely, a substrate expands by strain  $\varepsilon_{s0}$  along  $x$  direction under a tensile loading  $\sigma_t$ . Based on Hooke's law and plane-strain condition, it is easy to demonstrate that  $\varepsilon_{s0} = \frac{\sigma_t(1-\nu_s^2)}{E_s}$ . Thus, the optimal film

thickness can be rewritten in terms of  $\sigma_t$  as

$$t_f(x) = \frac{t_s(1-\nu_f^2)E_s/(1-\nu_s^2)E_f}{t_s\sigma_t/(x-a)\tau_{de} - 1}. \quad (5.33)$$

To verify this solution to the optimal thickness, acrylonitrile butadiene styrene (ABS) and Al 6061-T6 were employed to produce film-substrate bi-materials. Taking  $E_f = 2.2$  GPa,  $\nu_f = 0.35$  [172], and  $E_s = 68.9$  GPa,  $\nu_s = 0.33$  [173],  $|\sigma_t/\tau_{de}| = 300$ ,  $a = 30$  mm and  $t_s = 5$  mm, the optimal film thickness can be calculated as displayed in Figure 5.7(a). The gradient films were manufactured by 3D printing ( $\mu$ Print SE Plus, Stratasys) using ABS (ABSplus-P430, Stratasys) and adhered onto the substrate surface with all-purpose superglue (Aron Alpha), as schematically shown in Figure 5.7(b). For comparison, uniform films were also prepared with thickness profile shown in Figure 5.7(a). Since direct measurement of stress field is challenging, the shear strain field, which is believed proportional to the shear stress field for elastic deformation, was measured instead by using Digital Image Correlation technology (DIC) [174]. For this purpose, before the experiment the side surfaces to be tracked were spray-painted with uniform random speckle pattern as schematically shown in

Figure 5.7(b). Tensile loading was then applied on the substrate with a universal testing machine (GP-TS2000M, Gopoint) at a crosshead speed of 2 mm/min. During deformation, digital images of speckle pattern were captured every 10 s using a digital camera (Sony  $\alpha$ 57) with resolution of 31-33 pixels/mm. Based on the obtained images, DIC analysis was carried out with Ncorr [175], an open-source subset-based 2D DIC software package, to gain the shear strain field.

Figure 5.7(c) shows the obtained shear strain field of the side surface under tensile loading of  $\sigma_t = 173.3$  MPa, from which the shear strain along the interface was extracted and displayed in Figure 5.7(d). As expected, in the case with gradient film, the shear strain field developed along the bonded interface is almost uniform despite of some fluctuations which might be mainly attributed to the limitation of experimental conditions. In contrast, in the control case with uniform-thickness film, severe strain concentration occurred at interface edge. It is confirmed that gradient film thickness in bi-materials could effectively homogenize the shear stress on the interface, and consequently improve their resistance to interfacial crack initiation. As the shear stress along the interface is homogenized, the whole interface, upon sufficiently high loading, would fail simultaneously if the interfacial strength is uniform everywhere. In reality, however, interfacial crack would be firstly initiated at the weakest point on the interface. Once the crack is initiated, the distribution of shear stress along the interface is changed and becomes non-uniform. After that, gradient thickness would not be too much different from a uniform counterpart in resisting

crack propagation.

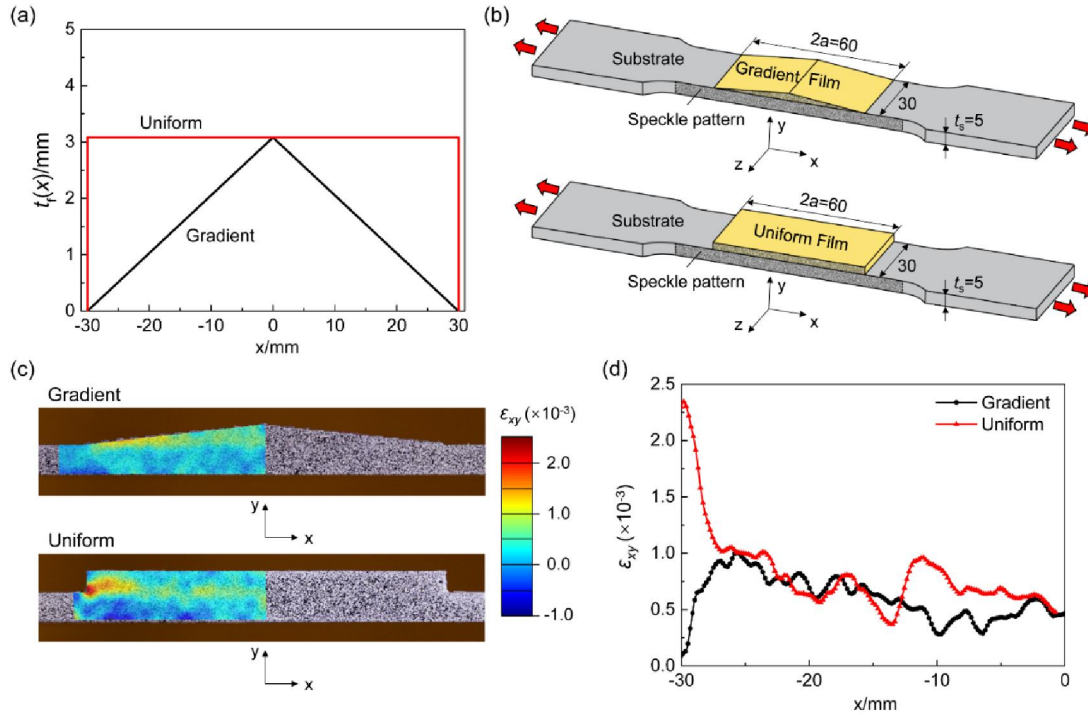


Figure 5.7 (a) Thickness profiles of the optimal gradient film and uniform control. (b) Schematics of the experimental setups (units: mm). (c) Shear strain field ( $\epsilon_{xy}$ ) on the side surface under a tensile loading  $\sigma = 173.3$  MPa, which was obtained by DIC analysis using software Nccor with the subset size, subset spacing and strain radius being taken as 40 pixels, 1 pixel and 15 pixels, respectively. (d) Shear strain ( $\epsilon_{xy}$ ) distribution along the interface between film and substrate under tensile loading  $\sigma = 173.3$  MPa.

### 5.3 Summary

In summary, in this paper we proposed to homogenize interfacial shear stress in bi-materials caused by strain misfit via thickness gradient. The solutions to the gradient thickness were obtained and the effectiveness of this strategy was demonstrated based on two typical bi-material systems: continuous film on disk-like substrate and island film on half-space substrate. The results in this paper are

believed to be of great value to the enhancement of resistance to interface delamination, either instant or fatigue-caused, in a variety of thin films such as thermal barrier coating [176], wear-resistant coating [177], electrode film on current collector in batteries [178] and discontinuous islands coating on biomedical devices [179]. In practice, however, there might be some occasions in which the film thickness has to be uniform due to some specific functional requirement. Under such kind of circumstances, adopting gradient stiffness (*i.e.*, elastic modulus) would be an alternative strategy, because it is easy to see from our theoretical solutions that gradient stiffness actually plays an equivalent role in homogenizing the interfacial shear stress distribution as gradient thickness does. Different from the traditional FGMs with stiffness gradient along thickness direction, here stiffness varies in a designed manner along the direction parallel to the interface. Implementation of such gradient stiffness is more challenging in manufacturing compared to that of the gradient thickness. On the other hand, limitations remain present in our work. First, our analysis assumed that both the film and substrate are elastic. This might not be always the case as the mechanical properties of a material may change in service as exemplified by the electrode of lithium-ion battery in process of lithiation and delithiation [180]. Additionally, in our theoretical analysis for determining the optimal gradient thickness of film, the possible buckling of the film caused by compressive stress has not been considered. Further investigations are needed to take these issues into account.



## **Chapter 6. Controllable morphing behavior of SAG/PE bi-material by utilizing strain misfit**

Strain mismatch is widely present in bi-material systems due to distinct deformation responses of the bonded materials to the external stimuli such as change of temperature or humidity. Generally, such strain misfit is considered detrimental to bi-materials since it will cause stress concentration on interface, and then lead to crack initiation and subsequent interface delamination. Therefore, quite a few strategies [23, 91, 97] have been developed to mitigate or eliminate the strain misfit-induced stress concentration on interface. On the other hand, strain misfit can be exploited instead to achieve controllable morphing behaviors, such as bending, for a wide range of applications. In 1925, Timoshenko [108] developed a theoretical model to predict the bending curvature of bi-metal strip thermostat when being uniformly heated, with the assumption that both the two materials are elastic solids. This model has been extensively employed to predict the bending curvature of diverse bi-materials and structures under various stimuli such as electricity [117] and moisture [107].

Recently, a stacked assembly of graphene (SAG)/polyethylene (PE) bi-material was developed by our collaborators [181]. Interestingly, the SAG/PE bilayer was found exhibiting abnormal morphing behaviors under thermal variations. When the SAG/PE bilayer is being heated, it will curl into a roll with SAG being wrapped inside, which is basically attributed to the misfit of thermal strain between the two layers.

However, when the SAG/PE bilayer is pretreated by a heating and subsequent cooling process under constrained condition, which is quite similar to the tempering treatment in metallurgy, it will curl spontaneously after releasing the constraint. Surprisingly, now the PE layer is wrapped inside by the SAG layer, which is opposite to that of the as-prepared sample without tempering. Clearly, such abnormal morphing behaviors in SAG/PE bi-material cannot be predicted by Timoshenko's model [108] directly. We suspect such abnormal morphing behaviors might be attributed to SAG, which was found exhibiting asymmetric elastoplastic properties under tension and compression. In this chapter, by considering the asymmetric elastoplasticity in SAG layer, the morphing behaviors of SAG/PE bilayer in response to thermal variations were systematically studied via a combination of theoretical modelling and finite element simulation. The obtained results are expected to provide explanation for the abnormal morphing behaviors of SAG/PE observed in experiment, and also guidelines for the application of SAG/PE and other alike bilayer materials in the field of sensors, actuators and soft robotics, etc.

## **6.1 Deformation of SAG/PE bi-material driven by thermal misfit**

Through molecular dynamics (MD) simulation, the SAG layer was found exhibiting asymmetric elastoplastic properties under tension and compression, namely, elastic and ideally plastic under tension and purely elastic under compression, as schematically shown in Figure 6.1 [181]. Thus, the mechanical behavior of SAG layer

can be described by four independent parameters including tensile elastic modulus ( $E_{SAG}^t$ ), tensile strength ( $S_{SAG}^t$ ), compressive elastic modulus ( $E_{SAG}^c$ ) and Poisson's ratio ( $\nu_{SAG}$ ) if it is assumed to be an isotropic continuum material. While PE layer can be taken as an elastic solid described by elastic modulus ( $E_{PE}$ ) and Poisson's ratio ( $\nu_{PE}$ ). In the following, theoretical modelling (plane strain assumption) was carried out to predict the bending curvature of SAG/PE bilayer when subject to thermal variations.

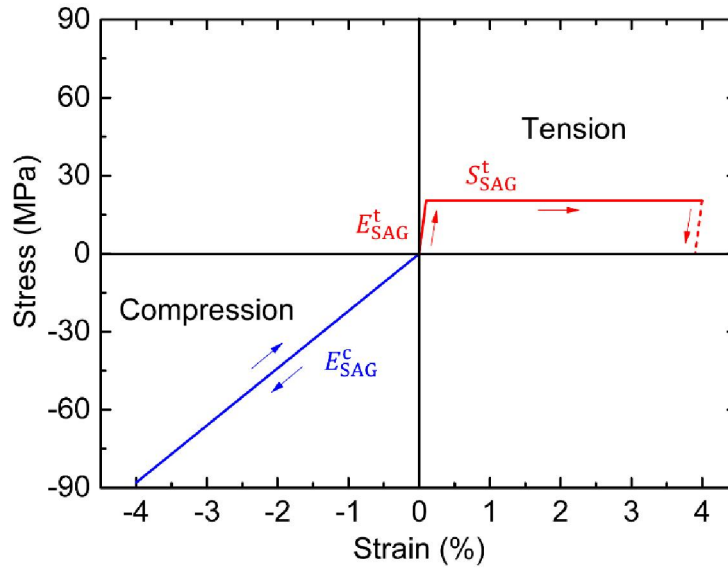


Figure 6.1 Asymmetric mechanical properties of SAG layer under tension and compression. (Adapted from [181])

Consider an SAG/PE bilayer (see Figure 6.2(a)). The thermal expansion coefficient of graphene is almost negligible [182] in comparison to that of PE ( $4 \times 10^{-4}/^{\circ}\text{C}$ ) [183]. When temperature increases, the resulting shear stress on the SAG/PE interface produces bending moments, making the bilayer film to curl with the SAG layer being wrapped inside the PE layer. Under such condition, the stress along

lateral direction is tension dominant in SAG layer, while compression dominant in PE layer. We assume that the whole SAG layer is in tensile elastic deformation along the lateral direction. Consider a segment cut out from the strip by two cross-sections  $mn$  and  $m_1n_1$ . All the forces acting on the cross section of bilayer can be equivalently represented by axial forces  $F$  and a bending moment  $M$  (see Figure 6.2(b)). Perfect bonding along the interface implies that

$$\alpha\Delta T(1 + \nu_{PE}) - \frac{F}{E'_{PE}t_{PE}b} = \frac{F}{E''_{SAG}t_{SAG}b} \quad (6.1)$$

in which  $E'_{PE} = E_{PE}/(1 - \nu_{PE}^2)$ ,  $E''_{SAG} = E_{SAG}^t/(1 - \nu_{SAG}^2)$ ,  $\alpha$  and  $t_{PE}$  are the thermal expansion coefficient and thickness of PE layer respectively, and  $t_{SAG}$  denotes the thickness of the SAG layer, and  $b$  is the width of the bilayer strip. From Eq. (6.1),  $F$  can be solved as

$$F = \alpha\Delta T(1 + \nu_{PE}) \left( \frac{1}{E'_{PE}t_{PE}b} + \frac{1}{E''_{SAG}t_{SAG}b} \right)^{-1} \quad (6.2)$$

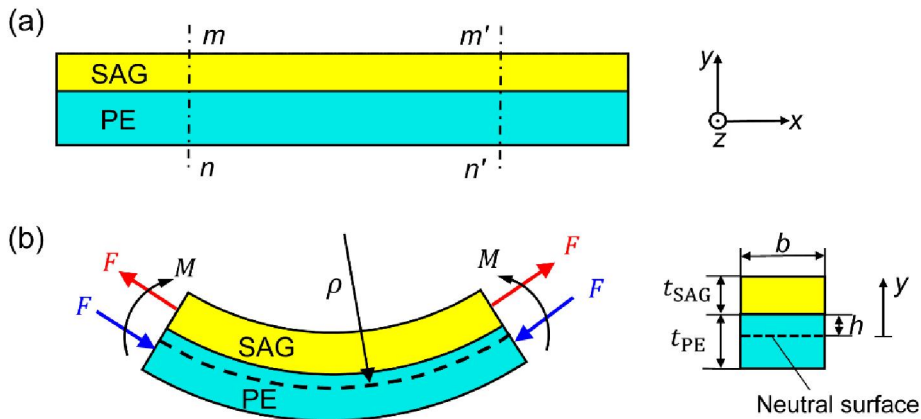


Figure 6.2 Bending of SAG/PE bilayer under uniform heating

Denote the radius of curvature of the neutral surface as  $\rho$ , as shown in Figure 6.2(b).

Then the bending-induced strain is given by

$$\varepsilon_{x\text{-bend}} = -\frac{y}{\rho} \quad (h - t_{\text{PE}} \leq y \leq h + t_{\text{SAG}}) \quad (6.3)$$

where  $h$  denotes the distance from the SAG/PE interface to the neutral surface. The stresses along lateral direction caused by axial force and bending moment in both SAG and PE layers are given by

$$\sigma_x^{(\text{SAG})} = \sigma_{x\text{-bend}}^{(\text{SAG})} + \sigma_{x\text{-axial}}^{(\text{SAG})} = -E_{\text{SAG}}' \frac{y}{\rho} + \frac{F}{bt_{\text{SAG}}} \quad (h \leq y \leq h + t_{\text{SAG}}) \quad (6.4a)$$

$$\sigma_x^{(\text{PE})} = \sigma_{x\text{-bend}}^{(\text{PE})} + \sigma_{x\text{-axial}}^{(\text{PE})} = -E_{\text{PE}}' \frac{y}{\rho} - \frac{F}{bt_{\text{PE}}} \quad (h - t_{\text{PE}} \leq y \leq h) \quad (6.4b)$$

In Eq. (6.4a), the whole SAG layer is assumed under tensile elastic deformation along the lateral direction, which will be discussed later.

The resultant force on the entire cross-section of the bilayer is zero, which implies

$$\int_h^{h+t_{\text{SAG}}} \sigma_x^{(\text{SAG})} b dy + \int_{h-t_{\text{PE}}}^h \sigma_x^{(\text{PE})} b dy = 0 \quad (6.5)$$

Substituting Eq. (6.4) into Eq. (6.5) determines  $h$  as

$$h = \frac{1}{2} \cdot \frac{E_{\text{PE}}' t_{\text{PE}}^2 - E_{\text{SAG}}' t_{\text{SAG}}^2}{E_{\text{PE}}' t_{\text{PE}} + E_{\text{SAG}}' t_{\text{SAG}}} \quad (6.6)$$

The resultant moment on the entire cross-section is also zero, giving rise to

$$\int_h^{h+t_{\text{SAG}}} \sigma_x^{(\text{SAG})} y dy + \int_{h-t_{\text{PE}}}^h \sigma_x^{(\text{PE})} y dy = 0 \quad (6.7)$$

Inserting Eq. (6.4) into Eq. (6.7) yields

$$\frac{E'_{SAG}}{3\rho} \left[ (h + t_{SAG})^3 - h^3 \right] + \frac{E'_{PE}}{3\rho} \left[ h^3 - (h - t_{PE})^3 \right] = \frac{F}{2b} (t_{PE} + t_{SAG}) \quad (6.8)$$

Combining Eqs. (6.2) (6.6) and (6.8) gives the curvature of the bilayer strip,  $\kappa$ , as

$$\kappa = \frac{1}{\rho} = \frac{6\alpha\Delta T(1 + \nu_{PE})(t_{PE} + t_{SAG})}{4(t_{PE}^2 + t_{SAG}^2) + 6t_{SAG}t_{PE} + \frac{E'_{PE}t_{PE}^3}{E'_{SAG}t_{SAG}} + \frac{E'_{SAG}t_{SAG}^3}{E'_{PE}t_{PE}}} \quad (6.9)$$

which is consistent with the prediction by Timoshenko [108]. Here, it should be noted that the curvature of SAG/PE bilayer is predicted based on the assumption that the whole SAG layer is under tensile elastic deformation along lateral direction, which, according to Eq. (6.4a), requires tensile stress at  $y = h + t_{SAG}$  while not yielding at  $y=h$ . Firstly, the stress in SAG layer at  $y = h + t_{SAG}$  should satisfy

$$\sigma_x^{(SAG)} \Big|_{y=h+t_{SAG}} = -E'_{SAG} \frac{h + t_{SAG}}{\rho} + \frac{F}{bt_{SAG}} > 0 \quad (6.10)$$

By recalling Eqs. (6.2) and (6.9), Eq. (6.10) can be rewritten as

$$4(t_{PE}^2 + t_{SAG}^2) + 6t_{SAG}t_{PE} + \frac{E'_{PE}t_{PE}^3}{E'_{SAG}t_{SAG}} + \frac{E'_{SAG}t_{SAG}^3}{E'_{PE}t_{PE}} - 6(t_{PE} + t_{SAG})(h + t_{SAG}) \left( 1 + \frac{E'_{SAG}t_{SAG}}{E'_{PE}t_{PE}} \right) > 0 \quad (6.11)$$

By taking  $E'_{SAG} = 20.7 \text{ GPa}$  ,  $\nu_{SAG} = 0.19$  ,  $E'_{PE} = 300 \text{ MPa}$  ,  $\nu_{PE} = 0.46$  and  $t_{PE} = 10 \mu\text{m}$ , the satisfaction of above inequality requires  $t_{SAG} \leq 0.75 \mu\text{m}$  . Secondly, the stress in SAG layer at  $y=h$  is

$$\sigma_x^{(SAG)} \Big|_{y=h} = -E_{SAG}' t \frac{h}{\rho} + \frac{F}{bt_{SAG}} \quad (6.12)$$

According to Hooke's law and plane strain condition, it is readily to demonstrate that the stress along  $z$  direction is  $\sigma_z^{(SAG)} = \nu_{SAG} \sigma_x^{(SAG)}$ . The normal stress along  $y$  direction is neglected due to the thin thickness and free surface of SAG layer, i.e.,  $\sigma_y^{(SAG)} = 0$ . Based on von Mises criterion, yielding will not happen in SAG layer until

$$\begin{aligned} \sigma_v &= \sqrt{\frac{1}{2} \left[ \left( \sigma_x^{(SAG)} - \sigma_y^{(SAG)} \right)^2 + \left( \sigma_x^{(SAG)} - \sigma_z^{(SAG)} \right)^2 + \left( \sigma_y^{(SAG)} - \sigma_z^{(SAG)} \right)^2 \right]} \\ &= \sigma_x^{(SAG)} \sqrt{1 - \nu_{SAG} + \nu_{SAG}^2} = S_{SAG}^t \end{aligned} \quad (6.13)$$

in which  $S_{SAG}^t$  is the yield strength of SAG under tension. By combining Eqs. (6.2) (6.6) (6.9) (6.12) and (6.13), the maximum temperature increment ( $\Delta T_e$ ) without causing plastic deformation in SAG layer can be determined as

$$\Delta T_e = \frac{S_{SAG}^t}{\sqrt{1 - \nu_{SAG} + \nu_{SAG}^2}} \times \left[ \frac{\alpha(1 + \nu_{PE})}{t_{SAG}/E_{PE}' t_{PE} + 1/E_{SAG}' t_{SAG}} - \frac{E_{SAG}' t}{2} \times \frac{E_{PE}' t_{PE}^2 + E_{SAG}' t_{SAG}^2}{E_{PE}' t_{PE} + E_{SAG}' t_{SAG}} \times \frac{6\alpha(1 + \nu_{PE})(t_{PE} + t_{SAG})}{4(t_{PE}^2 + t_{SAG}^2) + 6t_{SAG} t_{PE} + \frac{E_{PE}' t_{PE}^3}{E_{SAG}' t_{SAG}} + \frac{E_{SAG}' t_{SAG}^3}{E_{PE}' t_{PE}}} \right]^{-1} \quad (6.14)$$

This result was then examined via finite element simulation. In our modelling, a two-dimensional (2D) plane strain model was employed. The PE layer was modeled as a purely elastic solid with Young's modulus  $E_{PE} = 300$  MPa [184], Poisson's ratio  $\nu_{PE} = 0.46$  [185]. The SAG layer was assumed to be an isotropic continuum

material with asymmetric elastoplastic properties under tension and compression, which were adopted from the MD simulation results as displayed in Table 6.1. The thicknesses of PE and SAG were taken as  $t_{PE} = 10 \mu\text{m}$  and  $t_{SAG} = 0.1 - 0.6 \mu\text{m}$  (satisfying the requirement of Eq. (6.10)), respectively. The thermal expansion coefficients of PE and SAG were taken as  $\alpha = 4 \times 10^{-4} / ^\circ\text{C}$  [183] and zero, respectively. The interface between them was assumed perfectly bonded. 4-node plane strain thermally coupled quadrilateral elements (CPE4RT) were employed for analysis. Self-contact of the bilayer was neglected to avoid over complicated calculation. Figure 6.3 shows both the simulation results and theoretical estimations (by Eq. (6.14)) on the maximum temperature increment ( $\Delta T_e$ ) without causing plastic deformation in SAG layer, and a good agreement can be found. Therefore, for SAG/PE bilayer with  $t_{SAG} \leq 0.75 \mu\text{m}$ , its deformation can be predicted by Eq. (6.9) when the temperature increment  $\Delta T \leq \Delta T_e$ . Under such condition, reversible curling-uncurling process can be realized in SAG/PE bilayer with the application of cyclic thermal loadings.

Table 6.1 Mechanical properties of SAG layer obtained from MD simulation (Adapted from [181])

$E_{SAG}^t$	$S_{SAG}^t$	$E_{SAG}^c$	$\nu_{SAG}$
20.7 GPa	20.4 MPa	2.2 GPa	0.19

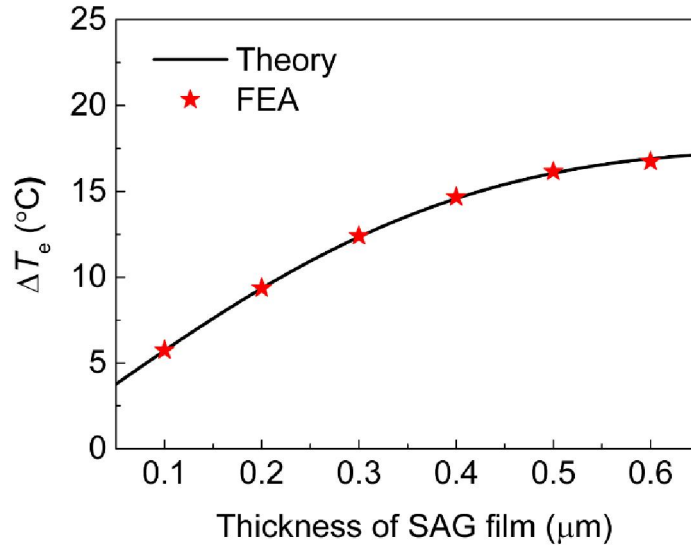


Figure 6.3 Maximum temperature increment ( $\Delta T_e$ ) for SAG/PE bilayer without triggering plastic deformation in SAG layer. Parameters adopted:  $E_{PE}=300$  MPa,  $\nu_{PE}=0.46$ ,  $t_{PE}=10$   $\mu\text{m}$ ,  $\alpha=4\times 10^{-4}/^\circ\text{C}$ ,  $E_{SAG}^t=20.7$  GPa,  $S_{SAG}^t=20.4$  MPa,  $E_{SAG}^c=2.2$  GPa,  $\nu_{SAG}=0.19$ .

## 6.2 Deformation of SAG/PE bi-material driven by plastic strain

With asymmetric elastoplastic properties in SAG layer, plastic deformation might be triggered in SAG through a tempering-like treatment and cause the SAG/PE bilayer to curl, as schematically shown in Figure 6.4. Firstly, the as-prepared SAG/PE bilayer is sandwiched by two rigid plates to constrain its possible out-of-plane deformation (Figure 6.4(a)). Then a tempering-like treatment, i.e., heating and subsequent cooling process (Figure 6.4(b, c)), is applied. During the heating stage, the PE layer expands laterally, resulting in tensile force in SAG layer and compressive force in PE layer. If the temperature increment ( $\Delta T$ ) is large enough, plastic deformation might occur in SAG. Then during the cooling stage, PE would return to its initial configuration, while the deformation in SAG layer cannot be fully recovered due to the presence of plastic deformation. This will result in residual compressive force in SAG layer and residual

tensile force in PE layer. Consequently, after releasing the constraint (Figure 6.4(d)), the SAG/PE bilayer will curl spontaneously with PE layer being wrapped inside the SAG due to the residual internal force. This process can be well reproduced via finite element simulation, as shown in Figure 6.5. Therefore, by considering the asymmetric elastoplasticity in SAG layer, the abnormal morphing behaviors of SAG/PE bilayer film observed in experiment can be well explained. In the following, theoretical analysis will be performed to predict the bending curvature of SAG/PE bilayer after constrained tempering.

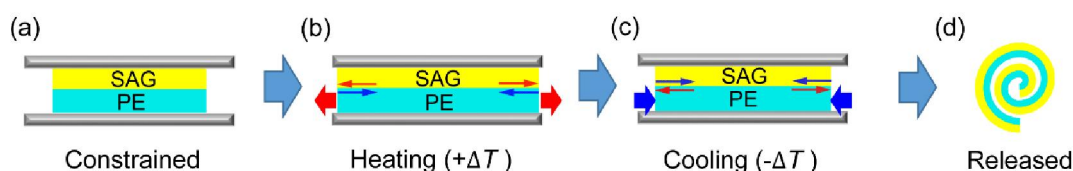


Figure 6.4 Schematic illustration showing the constrained tempering process of SAG/PE bilayer. (a) An SAG/PE bilayer is sandwiched by two rigid plates. (b) Upon heating by  $\Delta T$ , the PE layer expands laterally, resulting in tensile force in SAG layer and compressive force in PE layer. (c) Upon cooling, the PE layer would return to its initial configuration while the deformation in SAG layer cannot be fully recovered due to the plastic deformation in step (b), resulting in the residual tensile force in PE layer and residual compressive force in SAG layer. (d) After releasing the constraint of the plates, the SAG/PE bilayer film coils due to the internal residual stress.

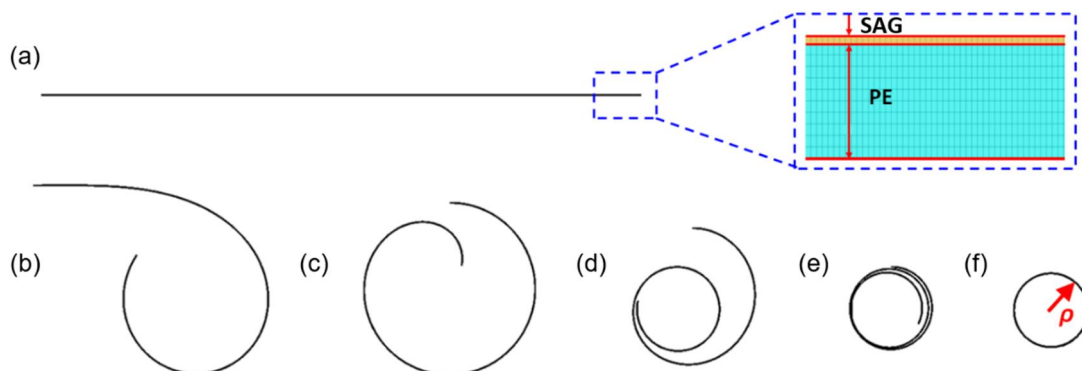


Figure 6.5 Simulated deforming process of a tempered SAG/PE bilayer film after being released from external constraint. (a) Configuration of an SAG/PE bilayer film

after constrained tempering. (b-f) Snapshots of the deforming process of the tempered SAG/PE bilayer after removing the constraint. Parameters adopted in the simulation:  $E_{PE}=300$  MPa,  $\nu_{PE}=0.46$ ,  $t_{PE}=10$   $\mu\text{m}$ ,  $\alpha=4\times 10^{-4}/^{\circ}\text{C}$ ,  $E_{SAG}^t=20.7$  GPa,  $S_{SAG}^t=20.4$  MPa,  $E_{SAG}^c=2.2$  GPa,  $\nu_{SAG}=0.19$ ,  $t_{SAG}=0.6$   $\mu\text{m}$ ,  $\Delta T=40$   $^{\circ}\text{C}$ .

Firstly, during heating stage (Figure 6.4(b)), given the negligible thermal expansion of the SAG layer, its deformation mainly results from the stretching by the attached PE layer. For the PE layer, on the other hand, the deformation includes two portions. One is the thermal expansion and the other is the strain caused by the reaction forces (compression) from the SAG layer. Consider a segment of a bilayer strip. The forces experienced are shown in Figure 6.6. The perfect bonding condition between the SAG and PE layers implies that

$$\alpha\Delta T(1+\nu_{PE})-\frac{F}{E'_{PE}bt_{PE}}=\frac{F}{E'^t_{SAG}bt_{SAG}} \quad (6.15)$$

where  $\Delta T$  is the temperature increment during heating,  $F$  is the lateral interaction force between the SAG and PE layers,  $E'_{PE}=E_{PE}/(1-\nu_{PE}^2)$  and  $E'^t_{SAG}=E^t_{SAG}/(1-\nu_{SAG}^2)$  with  $E_{PE}$ ,  $\nu_{PE}$  being the elastic modulus and Poisson's ratio,  $\alpha$  and  $t_{PE}$  are the thermal expansion coefficient and thickness of the PE layer respectively, and  $E^t_{SAG}$ ,  $\nu_{SAG}$ ,  $t_{SAG}$  denote the tensile elastic modulus, Poisson's ratio and thickness of the SAG layer respectively, and  $b$  is the width of the bilayer strip. The normal stress in the SAG layer along  $x$  direction, if assumed uniform on the cross-section, is given by

$$\sigma_x^{(SAG)}=\frac{F}{bt_{SAG}}=\frac{\alpha\Delta T(1+\nu_{PE})}{1/E'^t_{SAG}+t_{SAG}/t_{PE}E'_{PE}} \quad (6.16)$$

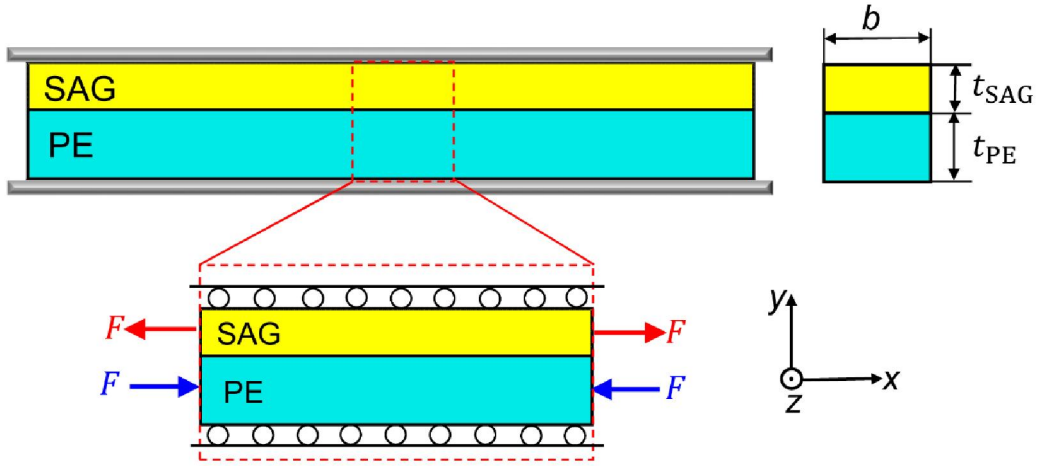


Figure 6.6 Forces experienced by the SAG/PE bilayer under constrained heating

Similarly, according to Hooke's law and plane strain condition, we have  $\sigma_z^{(SAG)} = \nu_{SAG} \sigma_x^{(SAG)}$ . The constraint applied along  $y$  direction mainly functions to restrain the bending deformation of bilayer strip, while the compressive stress exerted is negligible compared with the stresses along  $x$  and  $z$  directions. In our analysis, therefore, the stress along  $y$  direction is neglected, i.e.,  $\sigma_y^{(SAG)} = 0$ . Based on von Mises criterion, yielding will not happen until

$$\begin{aligned} \sigma_v &= \sqrt{\frac{1}{2} \left[ \left( \sigma_x^{(SAG)} - \sigma_y^{(SAG)} \right)^2 + \left( \sigma_x^{(SAG)} - \sigma_z^{(SAG)} \right)^2 + \left( \sigma_y^{(SAG)} - \sigma_z^{(SAG)} \right)^2 \right]} \\ &= \sigma_x^{(SAG)} \sqrt{1 - \nu_{SAG} + \nu_{SAG}^2} = S_{SAG}^t \end{aligned} \quad (6.17)$$

in which  $S_{SAG}^t$  is the tensile yield strength of SAG layer. By inserting Eq. (6.16) into Eq. (6.17), the minimum temperature increment to cause plastic deformation in the SAG layer is determined as

$$\Delta T_p^t = \frac{S_{SAG}^t}{\alpha(1 + \nu_{PE}) \sqrt{1 - \nu_{SAG} + \nu_{SAG}^2}} \cdot \left( \frac{1}{E_{SAG}^t} + \frac{t_{SAG}}{t_{PE} E_{PE}'} \right) \quad (6.18)$$

Taking  $E_{\text{SAG}}^t = 20.7 \text{ GPa}$  ,  $S_{\text{SAG}}^t = 20.4 \text{ MPa}$  ,  $\nu_{\text{SAG}} = 0.19$  ,  $t_{\text{SAG}} = 0.3 \mu\text{m}$  ,  
 $E_{\text{PE}} = 300 \text{ MPa}$  ,  $\nu_{\text{PE}} = 0.46$  ,  $\alpha = 4 \times 10^{-4} / ^\circ\text{C}$  and  $t_{\text{PE}} = 10 \mu\text{m}$ , estimation based on  
 Eq. (6.18) indicates that  $\Delta T_p^t \approx 4.8^\circ\text{C}$ . At the critical moment of yielding,  $F$   
 saturates at its maximum value, which can be determined by

$$\alpha \Delta T_p^t (1 + \nu_{\text{PE}}) - \frac{F_{\text{max}}}{E'_{\text{PE}} b t_{\text{PE}}} = \frac{F_{\text{max}}}{E'_{\text{SAG}} b t_{\text{SAG}}} \quad (6.19)$$

When  $\Delta T > \Delta T_p^t$ , temperature increment will only cause plastic strain ( $\varepsilon_p^t$ ) in the  
 SAG layer, while  $F_{\text{max}}$  remains constant. Therefore, when  $\Delta T > \Delta T_p^t$ , the perfect  
 bonding condition implies

$$\alpha \Delta T (1 + \nu_{\text{PE}}) - \frac{F_{\text{max}}}{E'_{\text{PE}} b t_{\text{PE}}} = \frac{F_{\text{max}}}{E'_{\text{SAG}} b t_{\text{SAG}}} + \varepsilon_p^t \quad (\text{for } \Delta T > \Delta T_p^t) \quad (6.20)$$

Eqs. (6.19) and (6.20) imply that the plastic strain  $\varepsilon_p^t$  can be written as

$$\varepsilon_p^t = \alpha (1 + \nu_{\text{PE}}) (\Delta T - \Delta T_p^t) \quad (6.21)$$

After the heating stage, the temperature then is reduced to the initial value (Figure  
 6.4(c)). The PE layer contracts, and the tensile load applied on the SAG layer gets  
 released. This causes the recovery of the elastic tensile strain in the SAG layer. Since  
 the SAG layer has experienced permanent elongation during the heating stage,  
 contraction of the PE layer would lead to compressive stress in the SAG layer while  
 tensile stress in the PE layer. After removing the external constraint, the strain misfit  
 between the SAG and PE layers, which is equal to the plastic strain ( $\varepsilon_p^t$ ) of the SAG

in the heating stage, causes the bilayer to curl with the PE layer being wrapped inside (Figure 6.4(d)). Consider a segment of the bilayer strip (see Figure 6.7). All the forces acting on the cross-section of the bilayer can be equivalently simplified as axial forces  $F$  plus a bending moment  $M$  (Figure 6.7). Perfect bonding along the interface implies that

$$\varepsilon_p^t - \frac{F}{E_{SAG}^{rc} b t_{SAG}} = \frac{F}{E_{PE}' b t_{PE}} \quad (6.22)$$

where  $E_{SAG}^{rc} = E_{SAG}^c / (1 - \nu_{SAG}^2)$  with  $E_{SAG}^c$  being the compressive elastic modulus of the SAG layer. Here, compressive elastic modulus of SAG layer is used since the stress in the SAG layer is compression dominant, which will be discussed later. From Eq. (6.22), we can determine  $F$  as

$$F = \varepsilon_p^t \left( \frac{1}{E_{PE}' b t_{PE}} + \frac{1}{E_{SAG}^{rc} b t_{SAG}} \right)^{-1} \quad (6.23)$$

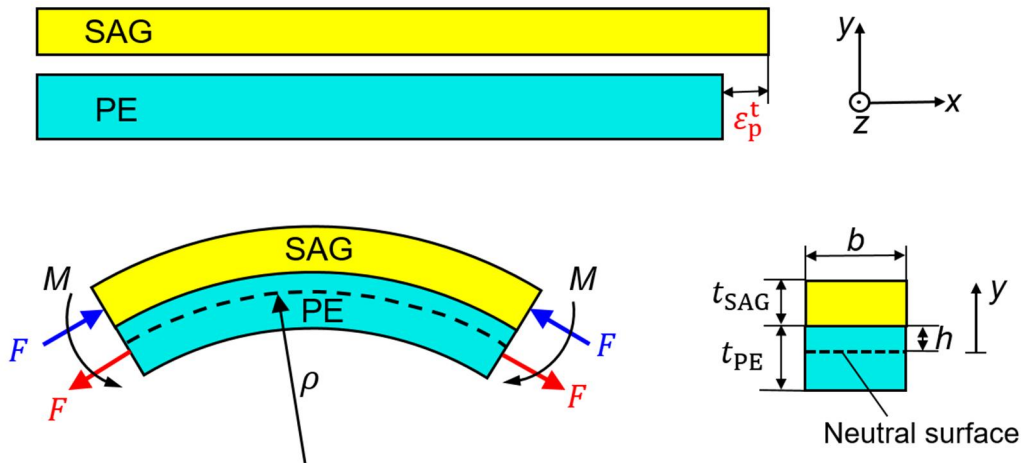


Figure 6.7 Curling of SAG/PE bilayer after constrained tempering and releasing

Denote the radius of curvature of the neutral surface as  $\rho$ , as shown in Figure 6.7.

The bending-induced strain is given by

$$\varepsilon_{x\text{-bend}} = \frac{y}{\rho} \quad (h - t_{\text{PE}} \leq y \leq h + t_{\text{SAG}}) \quad (6.24)$$

where  $h$  is the distance from the SAG/PE interface to the neutral surface. The stresses along lateral direction caused by axial force and bending moment in both SAG and PE layers are given by

$$\sigma_x^{(\text{SAG})} = \sigma_{x\text{-bend}}^{(\text{SAG})} + \sigma_{x\text{-axial}}^{(\text{SAG})} = E_{\text{SAG}}' \frac{y}{\rho} - \frac{F}{bt_{\text{SAG}}} \quad (h \leq y \leq h + t_{\text{SAG}}) \quad (6.25a)$$

$$\sigma_x^{(\text{PE})} = \sigma_{x\text{-bend}}^{(\text{PE})} + \sigma_{x\text{-axial}}^{(\text{PE})} = E_{\text{PE}}' \frac{y}{\rho} + \frac{F}{bt_{\text{PE}}} \quad (h - t_{\text{PE}} \leq y \leq h) \quad (6.25b)$$

In Eq. (6.25a), the whole SAG layer is assumed under compression along the lateral direction. This point will be discussed later.

The resultant force on the entire cross-section of the bilayer is zero, which implies

$$\int_h^{h+t_{\text{SAG}}} \sigma_x^{(\text{SAG})} b dy + \int_{h-t_{\text{PE}}}^h \sigma_x^{(\text{PE})} b dy = 0 \quad (6.26)$$

Inserting Eq. (6.25) into Eq. (6.26) determines  $h$  as

$$h = \frac{1}{2} \cdot \frac{E_{\text{PE}}' t_{\text{PE}}^2 - E_{\text{SAG}}' t_{\text{SAG}}^2}{E_{\text{PE}}' t_{\text{PE}} + E_{\text{SAG}}' t_{\text{SAG}}} \quad (6.27)$$

The resultant moment on the entire cross-section is also zero, giving rise to

$$\int_h^{h+t_{\text{SAG}}} \sigma_x^{(\text{SAG})} y dy + \int_{h-t_{\text{PE}}}^h \sigma_x^{(\text{PE})} y dy = 0 \quad (6.28)$$

Inserting Eq. (6.25) into Eq. (6.28) yields

$$\frac{E'_{\text{SAG}}}{3\rho} \left[ (h + t_{\text{SAG}})^3 - h^3 \right] + \frac{E'_{\text{PE}}}{3\rho} \left[ h^3 - (h - t_{\text{PE}})^3 \right] = \frac{F}{2b} (t_{\text{PE}} + t_{\text{SAG}}) \quad (6.29)$$

Combining Eqs. (6.21) (6.23) (6.27) and (6.29) gives the curvature of the bilayer strip,  $\kappa$ , as

$$\kappa = \frac{1}{\rho} = \frac{6\alpha(1 + \nu_{\text{PE}})(\Delta T - \Delta T_{\text{p}}^t)(t_{\text{PE}} + t_{\text{SAG}})}{4(t_{\text{PE}}^2 + t_{\text{SAG}}^2) + 6t_{\text{SAG}}t_{\text{PE}} + \frac{E'_{\text{PE}}t_{\text{PE}}^3}{E'_{\text{SAG}}t_{\text{SAG}}} + \frac{E'_{\text{SAG}}t_{\text{SAG}}^3}{E'_{\text{PE}}t_{\text{PE}}}} \quad (6.30)$$

The prediction of the curvature of SAG/PE bilayer above is based on the assumption that the whole SAG layer is under compression along lateral direction. This, according to Eq. (6.25a), requires that

$$\sigma_x^{(\text{SAG})} \Big|_{y=h+t_{\text{SAG}}} = E'_{\text{SAG}} \frac{h + t_{\text{SAG}}}{\rho} - \frac{F}{bt_{\text{SAG}}} < 0 \quad (6.31)$$

Recalling Eqs. (6.23) and (6.30), Eq. (6.31) can be rewritten as

$$4(t_{\text{PE}}^2 + t_{\text{SAG}}^2) + 6t_{\text{SAG}}t_{\text{PE}} + \frac{E'_{\text{PE}}t_{\text{PE}}^3}{E'_{\text{SAG}}t_{\text{SAG}}} + \frac{E'_{\text{SAG}}t_{\text{SAG}}^3}{E'_{\text{PE}}t_{\text{PE}}} - 6(t_{\text{PE}} + t_{\text{SAG}})(h + t_{\text{SAG}}) \left( 1 + \frac{E'_{\text{SAG}}t_{\text{SAG}}}{E'_{\text{PE}}t_{\text{PE}}} \right) > 0 \quad (6.32)$$

Taking  $E'_{\text{SAG}} = 2.2 \text{ GPa}$  ,  $\nu_{\text{SAG}} = 0.19$  ,  $E'_{\text{PE}} = 300 \text{ MPa}$  ,  $\nu_{\text{PE}} = 0.46$  and  $t_{\text{PE}} = 10 \mu\text{m}$ , the satisfaction of above inequality requires  $t_{\text{SAG}} \leq 2.2 \mu\text{m}$ . Thus the assumption of compressive stress in SAG layer is ensured.

By substituting related parameters into Eq. (6.30), the bending curvature of the SAG/PE bi-material after constrained tempering can be calculated. Figure 6.8 shows

the dependence of bending curvature on the thickness of SAG, which is well verified via finite element simulation. Therefore, the deformation of SAG/PE bilayer after constrained tempering can be well predicted and controlled. Based on these results, the configuration of SAG/PE bilayer can be programmed and customized.

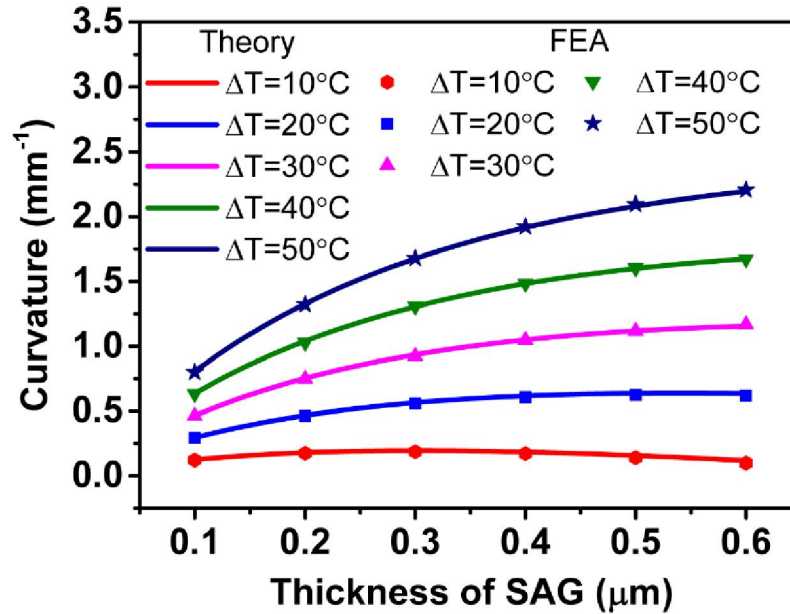


Figure 6.8 Bending curvature of the SAG/PE bi-material after constrained tempering predicted by theory and simulation. Parameters adopted:  $E_{PE}=300$  MPa,  $\nu_{PE}=0.46$ ,  $t_{PE}=10$   $\mu\text{m}$ ,  $\alpha=4\times 10^{-4}/^{\circ}\text{C}$ ,  $E_{SAG}^t=20.7$  GPa,  $S_{SAG}^t=20.4$  MPa,  $E_{SAG}^c=2.2$  GPa,  $\nu_{SAG}=0.19$ ,  $t_{SAG}=0.1\text{-}0.6$   $\mu\text{m}$ .

The curling of the SAG/PE bi-material after constrained tempering is owing to the residual plastic strain ( $\varepsilon_p^t$ ) in SAG layer serving as misfit strain between them. When the bi-material is reheated to such an extent that the thermal expansion in PE layer can exactly counterbalance the residual plastic strain ( $\varepsilon_p^t$ ) in SAG, the bi-material can be re-flattened. At this critical moment, the strains in SAG and PE layers should be equal without interaction forces between them, that is,

$$\alpha \Delta T_f (1 + \nu_{PE}) = \varepsilon_p^t \quad (6.33)$$

in which  $\Delta T_f$  is the temperature increment to re-flatten the SAG/PE bilayer. By recalling Eqs. (6.18) and (6.21), we have

$$\Delta T - \Delta T_f = \frac{S_{SAG}^t / E_{SAG}' + S_{SAG}^t t_{SAG} / E_{PE}' t_{PE}}{\alpha (1 + \nu_{PE}) \sqrt{1 - \nu_{SAG} + \nu_{SAG}^2}} \quad (6.34)$$

Clearly, the discrepancy between temperatures  $\Delta T - \Delta T_f$  is only dependent on the properties and dimensions of the bilayer. By substituting associated parameters into Eq. (6.34), the temperature difference  $\Delta T - \Delta T_f$  can be calculated as shown in Figure 6.9, which is well validated by finite element simulation. The re-flattening of SAG/PE is a reversible process and the bilayer will coil again upon temperature decrement. That is, the curled SAG/PE bi-material after constrained tempering can achieve a reversible uncurling-curling deformation under thermal cycles.

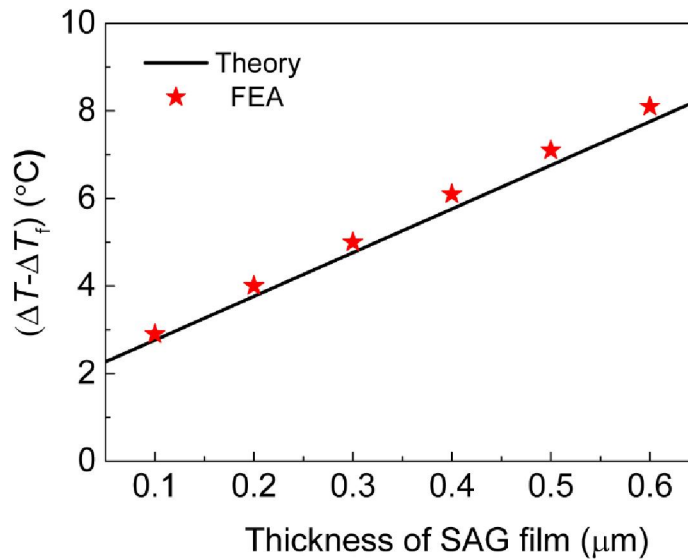


Figure 6.9 The dependence of  $(\Delta T - \Delta T_f)$  on the thickness of SAG layer. Here,  $\Delta T$  and  $\Delta T_f$  represent the tempering temperature and the critical temperature increment to

re-flatten the tempered SAG/PE bilayer, respectively. Parameters adopted in simulation:  $E_{PE}=300$  MPa,  $\nu_{PE}=0.46$ ,  $t_{PE}=10$   $\mu\text{m}$ ,  $\alpha=4\times 10^{-4}/^{\circ}\text{C}$ ,  $E_{SAG}^t=20.7$  GPa,  $S_{SAG}^t=20.4$  MPa,  $E_{SAG}^c=2.2$  GPa,  $\nu_{SAG}=0.19$ ,  $t_{SAG}=0.1-0.6$   $\mu\text{m}$ .

### **6.3 Summary**

In this chapter, the morphing behaviors of SAG/PE bilayer under thermal variations were systematically studied via a combination of theoretical modeling and finite element simulation. As SAG layer exhibits asymmetric elastoplastic properties, i.e., high plasticity under tension and high elasticity under compression, the strain misfit between the two distinct materials can be from either thermal mismatch or plastic strain. Through theoretical analysis, the morphing behaviors of SAG/PE bilayer under different thermal loadings were well predicted. These theoretical results can not only explain the abnormal morphing behaviors of SAG/PE bilayer observed in experiment, but also provide guidelines for controllable morphing behaviors in SAG/PE bilayer, which is of great importance for its application in the field of sensors, actuators and soft robotics, etc.



## **Chapter 7. Conclusions and future work**

In this thesis, interfacial mechanics were systematically studied to solve the interface-related problems in bi-materials and structures. Some strategies and guidelines were proposed for the design of bi-materials and structures with enhanced or controllable mechanical behaviors. In this chapter, we will summarize and discuss these strategies and guidelines, and an outlook to the future work will be presented.

### **7.1 Conclusions**

By taking advantage of the merits of the individual constituents and minimizing their weaknesses, bi-materials and structures always exhibit exceptional mechanical performance over monolithic counterpart. Nevertheless, they still suffer interface-related problems. One is the weak interface between the two bulk constituents, which makes interfacial crack and subsequent interfacial delamination easy to happen, and finally leads to reduced mechanical properties of the materials. The other is strain misfit-induced stress concentration on the interface between the two monolithic materials, which tends to evoke crack initiation and propagation. Here, several design strategies were proposed to solve these interface-related problems for enhanced mechanical performance in bi-materials and structures. On the other hand, the controllable morphing behaviors of bi-materials by taking advantage of the strain misfit were systematically studied. The typical conclusions are summarized as follows.

- We systematically studied the mechanical behavior of microscopic screw dislocation ( $\mu$ -SD), a type of helical structure in biological laminated composites. Analysis on an individual  $\mu$ -SD showed that the failure of the  $\mu$ -SD under tension involves the delamination of the prolonged spiral interface, giving rise to much higher toughness compared to those of the planar counterpart. Moreover, the corporation of multiple  $\mu$ -SDs was investigated by studying the effect of  $\mu$ -SD density on the mechanical reinforcement. It was found that the reinforcing effect was highly dependent on the density of  $\mu$ -SDs. The higher the density, the higher the reinforcement. The operation of such reinforcing mechanism of  $\mu$ -SD requires the delamination of spiral interface, which is not spontaneous but conditional. Theoretical modeling revealed that the proclivity of crack propagation along the spiral interface can be ensured if the fracture toughness of the interface is less than 60% of that of the matrix material. These findings not only uncover the reinforcing mechanisms of the  $\mu$ -SDs in biological materials but also imply promising application of  $\mu$ -SDs in reinforcing the synthetic laminated composites in engineering.
- We proposed to homogenize the interfacial shear stress distribution in film-substrate bi-material systems caused by strain misfit via thickness gradient. The solutions to the gradient thickness in the films were obtained based on two typical bi-material systems: continuous film on disk-like

substrate and island film on half-space substrate. The effectiveness of these theoretical solutions were well demonstrated via finite element simulation and experimental test. This strategy is believed to be of great value to the enhancement of resistance to interface delamination in a variety of film-substrate bi-material systems.

- We systematically studied the morphing behaviors of stacked assembly of graphene (SAG)/polyethylene (PE) bi-material under thermal variations via a combination of theoretical modeling and finite element simulation. As SAG layer exhibits asymmetric elastoplastic properties, i.e., high plasticity under tension and high elasticity under compression, the strain misfit between the two distinct materials can originate from either thermal mismatch or plastic strain. Through theoretical analysis, the deformation of SAG/PE bilayer under different thermal loadings was well predicted. These theoretical predictions apply to not only SAG/PE bi-material, but also other alike bi-material systems with asymmetric elastoplastic properties. These results are expected to provide guidelines for the application of such bi-material systems in the field of sensors, actuators and soft robotics, etc.

Therefore, in our investigation, some strategies and guidelines were proposed to tackle the interface-related problems in bi-materials and structures. These results would be of significant value for the design of bi-materials and structures with

enhanced or controllable mechanical behaviors.

## **7.2 Outlook to the future work**

### **7.2.1 Application of gradient strategy in bi-material systems**

In Chapter 5, theoretical solutions to the film thickness for a uniformly distributed shear stress on the interface of bi-material systems were demonstrated. Further studies on practical applications will be carried out. In lithium-ion batteries, the electrode film often suffers huge volume change (up to 300%-400% for Si) during charging and discharging cycles, leading to strain mismatch between the electrode film and current collector. As a result, shear stress concentration would be developed on the interface and interfacial delamination follows. If either the electrode film or the current collector is fabricated with well-designed gradient thickness, the shear stress on the interface would be homogenized during charging-discharging cycling. Such lithium-ion batteries are expected to have better electrochemical performance as well as longer cycle life.

Another potential application of our results may lie in the measurement of shear strength of interfaces between coating and substrate or fiber and matrix in composites. Traditionally, shear test [186] or pull-out test [187] is adopted to characterize the shear strength which is often taken as the pull-off force divided by the contact area. Such method tends to underestimate the shear strength because of the presence of stress concentration on the interface [188, 189]. If a uniform shear

stress distribution is achieved with the application of the proposed strategy of gradient thickness, more accurate measurement of shear strength is expected.

### **7.2.2 Determination of the stress-strain curve of SAG**

In Chapter 6, the distinct morphing behaviors of stacked assembly of graphene (SAG)/polyethylene (PE) bilayer under thermal variations are mainly attributed to the unique asymmetric elastoplastic properties in SAG. At present, such distinct mechanical properties of SAG are mainly demonstrated via molecular dynamics (MD) simulation. In the following, the stress-strain curve of SAG layer under tension and compression will be determined via experiment, following a similar method adopted in the study [190], in which the residual stress/strain in the coatings is determined via curvature measurement on bi-materials. On the other hand, the mechanical properties of SAG might be dependent on many factors, such as the average size of graphene flakes, and overlapping length between the graphene flakes. Theoretical modelling will be carried out to predict the mechanical behaviors of SAG under tension and compression.

## References

1. W. Tesch, N. Eidelman, P. Roschger, F. Goldenberg, K. Klaushofer, and P. Fratzl, Graded Microstructure and Mechanical Properties of Human Crown Dentin, *Calcified Tissue International* 69 (2001) 147-157.
2. H. Warshawsky, Organization of Crystals in Enamel, *The Anatomical Record* 224 (1989) 242-262.
3. W. Landis, The Strength of a Calcified Tissue Depends in Part on the Molecular Structure and Organization of Its Constituent Mineral Crystals in Their Organic Matrix, *Bone* 16 (1995) 533-544.
4. J.-Y. Rho, L. Kuhn-Spearing, and P. Zioupos, Mechanical Properties and the Hierarchical Structure of Bone, *Medical Engineering & Physics* 20 (1998) 92-102.
5. S. Weiner and H. D. Wagner, The Material Bone: Structure-Mechanical Function Relations, *Annual Review of Materials Science* 28 (1998) 271-298.
6. S. Weiner, A. Veis, E. Beniash, T. Arad, J. W. Dillon, B. Sabsay, and F. Siddiqui, Peritubular Dentin Formation: Crystal Organization and the Macromolecular Constituents in Human Teeth, *Journal of Structural Biology* 126 (1999) 27-41.
7. G. W. Marshall Jr, S. J. Marshall, J. H. Kinney, and M. Balooch, The Dentin Substrate: Structure and Properties Related to Bonding, *Journal of Dentistry* 25 (1997) 441-458.
8. H. Gao, B. Ji, I. L. Jäger, E. Arzt, and P. Fratzl, Materials Become Insensitive to Flaws at Nanoscale: Lessons from Nature, *Proceedings of the National Academy of Sciences* 100 (2003) 5597-5600.
9. B. Ji and H. Gao, Mechanical Properties of Nanostructure of Biological Materials, *Journal of the Mechanics and Physics of Solids* 52 (2004) 1963-1990.
10. Y. Shao, H.-P. Zhao, X.-Q. Feng, and H. Gao, Discontinuous Crack-Bridging Model for Fracture Toughness Analysis of Nacre, *Journal of the Mechanics and Physics of Solids* 60 (2012) 1400-1419.
11. H. Tang, F. Barthelat, and H. D. Espinosa, An Elasto-Viscoplastic Interface Model for Investigating the Constitutive Behavior of Nacre, *Journal of the Mechanics and Physics of Solids* 55 (2007) 1410-1438.
12. S. Wang, G. Wu, Z. Ling, and Z. Huang, Microstructure and Mechanical Properties of  $YAl_2$  Reinforced MgLiAl Composite, *Materials Science and Engineering: A* 518 (2009) 158-161.

13. P. F. Becher and G. C. Wei, Toughening Behavior in SiC-Whisker-Reinforced Alumina, *Journal of the American Ceramic Society* 67 (1984) C-267-C-269.
14. A. J. Caputo, D. P. Stinton, R. A. Lowden, and T. M. Besmann, Fiber-Reinforced SiC Composites with Improved Mechanical Properties, *American Ceramic Society Bulletin* 66 (1987).
15. N. Chawla and Y. L. Shen, Mechanical Behavior of Particle Reinforced Metal Matrix Composites, *Advanced Engineering Materials* 3 (2001) 357-370.
16. S. Grützner, L. Krüger, M. Radajewski, and I. Schneider, Characterization of In-Situ TiB/TiC Particle-Reinforced Ti-5Al-5Mo-5V-3Cr Matrix Composites Synthesized by Solid-State Reaction with B<sub>4</sub>C and Graphite through SPS, *Metals* 8 (2018) 377.
17. M. Montaigu, M. Robert, E. A. Ahmed, and B. Benmokrane, Laboratory Characterization and Evaluation of Durability Performance of New Polyester and Vinylester E-Glass GFRP Dowels for Jointed Concrete Pavement, *Journal of Composites for Construction* 17 (2012) 176-187.
18. M. K. Brun and R. N. Singh, Effect of Thermal Expansion Mismatch and Fiber Coating on the Fiber/Matrix Interfacial Shear Stress in Ceramic Matrix Composites, *Advanced Ceramic Materials;(USA)* 3 (1988).
19. A. Akisanya and N. Fleck, Interfacial Cracking from the Freeedge of a Long Bi-Material Strip, *International Journal of Solids and Structures* 34 (1997) 1645-1665.
20. V. Hein and F. Erdogan, Stress Singularities in a Two-Material Wedge, *International Journal of Fracture Mechanics* 7 (1971) 317-330.
21. A. Rao, Stress Concentrations and Singularities at Interface Corners, *ZAMM-Journal of Applied Mathematics and Mechanics/Zeitschrift für Angewandte Mathematik und Mechanik* 51 (1971) 395-406.
22. R. Vaßen, S. Giesen, and D. Stöver, Lifetime of Plasma-Sprayed Thermal Barrier Coatings: Comparison of Numerical and Experimental Results, *Journal of Thermal Spray Technology* 18 (2009) 835.
23. Z. Guo, L. Zhou, and H. Yao, Improving the Electrochemical Performance of Si-Based Anode via Gradient Si Concentration, *Materials & Design* 177 (2019) 107851.
24. J. Currey and J. Taylor, The Mechanical Behaviour of Some Molluscan Hard Tissues, *Journal of Zoology* 173 (1974) 395-406.
25. A. Jackson, J. F. Vincent, and R. Turner, The Mechanical Design of Nacre,

*Proceedings of the Royal Society of London. Series B. Biological Sciences* 234 (1988) 415-440.

26. S. E. Naleway, M. M. Porter, J. McKittrick, and M. A. Meyers, Structural Design Elements in Biological Materials: Application to Bioinspiration, *Advanced Materials* 27 (2015) 5455-5476.

27. Y. Li, C. Ortiz, and M. C. Boyce, Bioinspired, Mechanical, Deterministic Fractal Model for Hierarchical Suture Joints, *Physical Review E* 85 (2012) 031901.

28. A. Danin and J. Reyes-Betancort, The Status of *Portulaca Oleracea* in Tenerife, the Canary Islands, *Lagascalia* 26 (2006) 71-81.

29. Y. Li, C. Ortiz, and M. C. Boyce, Stiffness and Strength of Suture Joints in Nature, *Physical Review E* 84 (2011) 062904.

30. L. Liu and Y. Li, Failure Mechanism Transition of 3D-Printed Biomimetic Sutures, *Engineering Fracture Mechanics* 199 (2018) 372-379.

31. Y. Li, C. Ortiz, and M. C. Boyce, A Generalized Mechanical Model for Suture Interfaces of Arbitrary Geometry, *Journal of the Mechanics and Physics of Solids* 61 (2013) 1144-1167.

32. E. Lin, Y. Li, C. Ortiz, and M. C. Boyce, 3D Printed, Bio-Inspired Prototypes and Analytical Models for Structured Suture Interfaces with Geometrically-Tuned Deformation and Failure Behavior, *Journal of the Mechanics and Physics of Solids* 73 (2014) 166-182.

33. K. Miroshnichenko, L. Liu, I. Tsukrov, and Y. Li, Mechanical Model of Suture Joints with Fibrous Connective Layer, *Journal of the Mechanics and Physics of Solids* 111 (2018) 490-502.

34. I. Malik, M. Mirkhalaf, and F. Barthelat, Bio-Inspired “Jigsaw”-Like Interlocking Sutures: Modeling, Optimization, 3D Printing and Testing, *Journal of the Mechanics and Physics of Solids* 102 (2017) 224-238.

35. I. A. Malik and F. Barthelat, Bioinspired Sutured Materials for Strength and Toughness: Pullout Mechanisms and Geometric Enrichments, *International Journal of Solids and Structures* 138 (2018) 118-133.

36. M. Mirkhalaf and F. Barthelat, Design, 3D Printing and Testing of Architected Materials with Bistable Interlocks, *Extreme Mechanics Letters* 11 (2017) 1-7.

37. C. A. Long, Intricate Sutures as Fractal Curves, *Journal of Morphology* 185 (1985) 285-295.

38. T. L. Daniel, B. S. Helmuth, W. B. Saunders, and P. D. Ward, Septal

Complexity in Ammonoid Cephalopods Increased Mechanical Risk and Limited Depth, *Paleobiology* 23 (1997) 470-481.

39. M. A. Hassan, G. E. Westermann, R. A. Hewitt, and M. A. Dokainish, Finite-Element Analysis of Simulated Ammonoid Septa (Extinct Cephalopoda): Septal and Sutural Complexities Do Not Reduce Strength, *Paleobiology* 28 (2002) 113-126.

40. W. B. Saunders and D. M. Work, Shell Morphology and Suture Complexity in Upper Carboniferous Ammonoids, *Paleobiology* 22 (1996) 189-218.

41. W. Saunders, D. Work, and S. Nikolaeva, Evolution of Complexity in Paleozoic Ammonoid Sutures, *Science* 286 (1999) 760-763.

42. E. Lin, Y. Li, J. C. Weaver, C. Ortiz, and M. C. Boyce, Tunability and Enhancement of Mechanical Behavior with Additively Manufactured Bio-Inspired Hierarchical Suture Interfaces, *Journal of Materials Research* 29 (2014) 1867-1875.

43. B.-W. Li, H.-P. Zhao, Q.-H. Qin, X.-Q. Feng, and S.-W. Yu, Numerical Study on the Effects of Hierarchical Wavy Interface Morphology on Fracture Toughness, *Computational Materials Science* 57 (2012) 14-22.

44. Z. Zhang and J. Yang, Biomechanical Dynamics of Cranial Sutures During Simulated Impulsive Loading, *Applied Bionics and Biomechanics* 2015 (2015).

45. R. P. Hubbard, J. W. Melvin, and I. T. Barodawala, Flexure of Cranial Sutures, *Journal of Biomechanics* 4 (1971) 491-496.

46. C. R. Jaslow, Mechanical Properties of Cranial Sutures, *Journal of Biomechanics* 23 (1990) 313-321.

47. K. L. Rafferty and S. W. Herring, Craniofacial Sutures: Morphology, Growth, and in Vivo Masticatory Strains, *Journal of Morphology* 242 (1999) 167-179.

48. J. Song, S. Reichert, I. Kallai, D. Gazit, M. Wund, M. C. Boyce, and C. Ortiz, Quantitative Microstructural Studies of the Armor of the Marine Threespine Stickleback (*Gasterosteus aculeatus*), *Journal of Structural Biology* 171 (2010) 318-331.

49. S. Krauss, E. Monsonego-Ornan, E. Zelzer, P. Fratzl, and R. Shahar, Mechanical Function of a Complex Three-Dimensional Suture Joining the Bony Elements in the Shell of the Red-Eared Slider Turtle, *Advanced Materials* 21 (2009) 407-412.

50. N. Lee, M. Horstemeyer, H. Rhee, B. Nabors, J. Liao, and L. N. Williams, Hierarchical Multiscale Structure-Property Relationships of the Red-Bellied Woodpecker (*Melanerpes carolinus*) Beak, *Journal of the Royal Society Interface* 11

(2014) 20140274.

51. L. Liu, Y. Jiang, M. Boyce, C. Ortiz, J. Baur, J. Song, and Y. Li, The Effects of Morphological Irregularity on the Mechanical Behavior of Interdigitated Biological Sutures under Tension, *Journal of Biomechanics* 58 (2017) 71-78.

52. C. Gao, B. P. Hasseldine, L. Li, J. C. Weaver, and Y. Li, Amplifying Strength, Toughness, and Auxeticity via Wavy Sutural Tessellation in Plant Seedcoats, *Advanced Materials* 30 (2018) 1800579.

53. M. Mirkhalaf, A. K. Dastjerdi, and F. Barthelat, Overcoming the Brittleness of Glass through Bio-Inspiration and Micro-Architecture, *Nature Communications* 5 (2014) 3166.

54. I. A. Malik and F. Barthelat, Toughening of Thin Ceramic Plates Using Bioinspired Surface Patterns, *International Journal of Solids and Structures* 97 (2016) 389-399.

55. R. Wang, Z. Suo, A. Evans, N. Yao, and I. A. Aksay, Deformation Mechanisms in Nacre, *Journal of Materials Research* 16 (2001) 2485-2493.

56. M. A. Meyers, A. Y.-M. Lin, P.-Y. Chen, and J. Muiyco, Mechanical Strength of Abalone Nacre: Role of the Soft Organic Layer, *Journal of the Mechanical Behavior of Biomedical Materials* 1 (2008) 76-85.

57. F. Song, A. Soh, and Y. Bai, Structural and Mechanical Properties of the Organic Matrix Layers of Nacre, *Biomaterials* 24 (2003) 3623-3631.

58. A. Lin and M. A. Meyers, Growth and Structure in Abalone Shell, *Materials Science and Engineering: A* 390 (2005) 27-41.

59. R. Rabiei, S. Bekah, and F. Barthelat, Failure Mode Transition in Nacre and Bone-Like Materials, *Acta Biomaterialia* 6 (2010) 4081-4089.

60. G. Mayer and M. Sarikaya, Rigid Biological Composite Materials: Structural Examples for Biomimetic Design, *Experimental Mechanics* 42 (2002) 395-403.

61. G. Mayer, Rigid Biological Systems as Models for Synthetic Composites, *Science* 310 (2005) 1144-1147.

62. F. Barthelat and H. D. Espinosa, An Experimental Investigation of Deformation and Fracture of Nacre–Mother of Pearl, *Experimental Mechanics* 47 (2007) 311-324.

63. F. Barthelat, H. Tang, P. Zavattieri, C.-M. Li, and H. D. Espinosa, On the Mechanics of Mother-of-Pearl: A Key Feature in the Material Hierarchical Structure, *Journal of the Mechanics and Physics of Solids* 55 (2007) 306-337.

64. H. D. Espinosa, J. E. Rim, F. Barthelat, and M. J. Buehler, Merger of Structure and Material in Nacre and Bone—Perspectives on De Novo Biomimetic Materials, *Progress in Materials Science* 54 (2009) 1059-1100.

65. B. L. Smith, T. E. Schäffer, M. Viani, J. B. Thompson, N. A. Frederick, J. Kindt, A. Belcher, G. D. Stucky, D. E. Morse, and P. K. Hansma, Molecular Mechanistic Origin of the Toughness of Natural Adhesives, Fibres and Composites, *Nature* 399 (1999) 761.

66. F. Barthelat and R. Rabiei, Toughness Amplification in Natural Composites, *Journal of the Mechanics and Physics of Solids* 59 (2011) 829-840.

67. F. Song and Y. Bai, Effects of Nanostructures on the Fracture Strength of the Interfaces in Nacre, *Journal of Materials Research* 18 (2003) 1741-1744.

68. A. Evans, Z. Suo, R. Wang, I. A. Aksay, M. He, and J. Hutchinson, Model for the Robust Mechanical Behavior of Nacre, *Journal of Materials Research* 16 (2001) 2475-2484.

69. H. D. Espinosa, A. L. Juster, F. J. Latourte, O. Y. Loh, D. Gregoire, and P. D. Zavattieri, Tablet-Level Origin of Toughening in Abalone Shells and Translation to Synthetic Composite Materials, *Nature Communications* 2 (2011) 173.

70. Y. Ni, Z. Song, H. Jiang, S.-H. Yu, and L. He, Optimization Design of Strong and Tough Nacreous Nanocomposites through Tuning Characteristic Lengths, *Journal of the Mechanics and Physics of Solids* 81 (2015) 41-57.

71. M. R. Begley, N. R. Philips, B. G. Compton, D. V. Wilbrink, R. O. Ritchie, and M. Utz, Micromechanical Models to Guide the Development of Synthetic ‘Brick and Mortar’ composites, *Journal of the Mechanics and Physics of Solids* 60 (2012) 1545-1560.

72. N. Abid, M. Mirkhalaf, and F. Barthelat, Discrete-Element Modeling of Nacre-Like Materials: Effects of Random Microstructures on Strain Localization and Mechanical Performance, *Journal of the Mechanics and Physics of Solids* 112 (2018) 385-402.

73. L. Addadi, D. Joester, F. Nudelman, and S. Weiner, Mollusk Shell Formation: A Source of New Concepts for Understanding Biomineralization Processes, *Chemistry—A European Journal* 12 (2006) 980-987.

74. F. Song, J. Zhou, X. Xu, Y. Xu, and Y. Bai, Effect of a Negative Poisson Ratio in the Tension of Ceramics, *Physical Review Letters* 100 (2008) 245502.

75. K. Gries, R. Kröger, C. Kübel, M. Schowalter, M. Fritz, and A. Rosenauer, Correlation of the Orientation of Stacked Aragonite Platelets in Nacre and Their Connection via Mineral Bridges, *Ultramicroscopy* 109 (2009) 230-236.

76. A. G. Checa, J. H. Cartwright, and M.-G. Willinger, Mineral Bridges in Nacre, *Journal of Structural Biology* 176 (2011) 330-339.

77. Y. Shao, H.-P. Zhao, and X.-Q. Feng, Optimal Characteristic Nanosizes of Mineral Bridges in Mollusk Nacre, *RSC Advances* 4 (2014) 32451-32456.

78. K. S. Katti, D. R. Katti, S. M. Pradhan, and A. Bhosle, Platelet Interlocks Are the Key to Toughness and Strength in Nacre, *Journal of Materials Research* 20 (2005) 1097-1100.

79. K. S. Katti and D. R. Katti, Why Is Nacre So Tough and Strong? *Materials Science and Engineering: C* 26 (2006) 1317-1324.

80. I. Corni, T. Harvey, J. Wharton, K. Stokes, F. Walsh, and R. Wood, A Review of Experimental Techniques to Produce a Nacre-Like Structure, *Bioinspiration & Biomimetics* 7 (2012) 031001.

81. F. Bouville, E. Maire, S. Meille, B. Van de Moortèle, A. J. Stevenson, and S. Deville, Strong, Tough and Stiff Bioinspired Ceramics from Brittle Constituents, *Nature Materials* 13 (2014) 508.

82. Z. Yin, F. Hannard, and F. Barthelat, Impact-Resistant Nacre-Like Transparent Materials, *Science* 364 (2019) 1260-1263.

83. H. Gao and H. Yao, Shape Insensitive Optimal Adhesion of Nanoscale Fibrillar Structures, *Proceedings of the National Academy of Sciences* 101 (2004) 7851-7856.

84. H. Yao and H. Gao, Optimal Shapes for Adhesive Binding between Two Elastic Bodies, *Journal of Colloid and Interface Science* 298 (2006) 564-572.

85. B. Aksak, K. Sahin, and M. Sitti, The Optimal Shape of Elastomer Mushroom-Like Fibers for High and Robust Adhesion, *Beilstein Journal of Nanotechnology* 5 (2014) 630-638.

86. S. Gorb, M. Varenberg, A. Peressadko, and J. Tuma, Biomimetic Mushroom-Shaped Fibrillar Adhesive Microstructure, *Journal of the Royal Society Interface* 4 (2006) 271-275.

87. A. Spuskanyuk, R. McMeeking, V. Deshpande, and E. Arzt, The Effect of Shape on the Adhesion of Fibrillar Surfaces, *Acta Biomaterialia* 4 (2008) 1669-1676.

88. A. Del Campo, C. Greiner, and E. Arzt, Contact Shape Controls Adhesion of Bioinspired Fibrillar Surfaces, *Langmuir* 23 (2007) 10235-10243.

89. R. Balijepalli, M. Begley, N. Fleck, R. McMeeking, and E. Arzt, Numerical Simulation of the Edge Stress Singularity and the Adhesion Strength for Compliant Mushroom Fibrils Adhered to Rigid Substrates, *International Journal of Solids and Structures* 85 (2016) 160-171.

90. G. Carbone and E. Pierro, Sticky Bio-Inspired Micropillars: Finding the Best Shape, *Small* 8 (2012) 1449-1454.
91. X. Xiao, P. Liu, M. Verbrugge, H. Haftbaradaran, and H. Gao, Improved Cycling Stability of Silicon Thin Film Electrodes through Patterning for High Energy Density Lithium Batteries, *Journal of Power Sources* 196 (2011) 1409-1416.
92. H. Gao, X. Wang, H. Yao, S. Gorb, and E. Arzt, Mechanics of Hierarchical Adhesion Structures of Geckos, *Mechanics of Materials* 37 (2005) 275-285.
93. B. J. Bruet, J. Song, M. C. Boyce, and C. Ortiz, Materials Design Principles of Ancient Fish Armour, *Nature Materials* 7 (2008) 748.
94. P.-Y. Chen, J. Schirer, A. Simpson, R. Nay, Y.-S. Lin, W. Yang, M. I. Lopez, J. Li, E. A. Olevsky, and M. A. Meyers, Predation Versus Protection: Fish Teeth and Scales Evaluated by Nanoindentation, *Journal of Materials Research* 27 (2012) 100-112.
95. H. Yao and H. Gao, Gibson-Soil-Like Materials Achieve Flaw-Tolerant Adhesion, *Journal of Computational and Theoretical Nanoscience* 7 (2010) 1299-1305.
96. G. Marshall Jr, M. Balooch, R. Gallagher, S. Gansky, and S. Marshall, Mechanical Properties of the Dentinoenamel Junction: AFM Studies of Nanohardness, Elastic Modulus, and Fracture, *Journal of Biomedical Materials Research: An Official Journal of the Society for Biomaterials and the Japanese Society for Biomaterials* 54 (2001) 87-95.
97. Y. Lee and F. Erdogan, Residual/Thermal Stresses in FGM and Laminated Thermal Barrier Coatings, *International Journal of Fracture* 69 (1994) 145-165.
98. C. Wang, Y. Wang, S. Fan, Y. You, L. Wang, C. Yang, X. Sun, and X. Li, Optimized Functionally Graded  $\text{La}_2\text{Zr}_2\text{O}_7/8\text{YSZ}$  Thermal Barrier Coatings Fabricated by Suspension Plasma Spraying, *Journal of Alloys and Compounds* 649 (2015) 1182-1190.
99. S. Suresh, M. Olsson, A. Giannakopoulos, N. Padture, and J. Jitcharoen, Engineering the Resistance to Sliding-Contact Damage through Controlled Gradients in Elastic Properties at Contact Surfaces, *Acta Materialia* 47 (1999) 3915-3926.
100. D. Pender, N. Padture, A. Giannakopoulos, and S. Suresh, Gradients in Elastic Modulus for Improved Contact-Damage Resistance. Part I: The Silicon Nitride–Oxynitride Glass System, *Acta Materialia* 49 (2001) 3255-3262.
101. D. Bernoulli, S. C. Cao, J. Lu, and M. Dao, Enhanced Repeated Frictional Sliding Properties in 304 Stainless Steel with a Gradient Nanostructured Surface, *Surface and Coatings Technology* 339 (2018) 14-19.

102. J. Jitcharoen, N. P. Padture, A. E. Giannakopoulos, and S. Suresh, Hertzian-Crack Suppression in Ceramics with Elastic-Modulus-Graded Surfaces, *Journal of the American Ceramic Society* 81 (1998) 2301-2308.
103. A. Prasad, M. Dao, and S. Suresh, Steady-State Frictional Sliding Contact on Surfaces of Plastically Graded Materials, *Acta Materialia* 57 (2009) 511-524.
104. H. Peisker, J. Michels, and S. N. Gorb, Evidence for a Material Gradient in the Adhesive Tarsal Setae of the Ladybird Beetle *Coccinella septempunctata*, *Nature Communications* 4 (2013) 1661.
105. R. G. Balijepalli, S. C. Fischer, R. Hensel, R. M. McMeeking, and E. Arzt, Numerical Study of Adhesion Enhancement by Composite Fibrils with Soft Tip Layers, *Journal of the Mechanics and Physics of Solids* 99 (2017) 357-378.
106. A. Rafsanjani, V. Brulé, T. L. Western, and D. Pasini, Hydro-Responsive Curling of the Resurrection Plant *Selaginella lepidophylla*, *Scientific Reports* 5 (2015) 8064.
107. P. Zhang, P.-Y. Chen, B. Wang, R. Yu, H. Pan, and B. Wang, Evaluating the Hierarchical, Hygroscopic Deformation of the *Daucus Carota* Umbel through Structural Characterization and Mechanical Analysis, *Acta Biomaterialia* 99 (2019) 457-468.
108. S. Timoshenko, Analysis of Bi-Metal Thermostats, *Josa* 11 (1925) 233-255.
109. A. Kotikian, C. McMahan, E. C. Davidson, J. M. Muhammad, R. D. Weeks, C. Daraio, and J. A. Lewis, Untethered Soft Robotic Matter with Passive Control of Shape Morphing and Propulsion, *Science Robotics* 4 (2019) Art. No. eaax7044.
110. K. Hou, Y. Nie, I. T. Mugaanire, Y. Guo, and M. Zhu, A Novel Leaf Inspired Hydrogel Film Based on Fiber Reinforcement as Rapid Steam Sensor, *Chemical Engineering Journal* (2019) 122948.
111. M. Wang, B.-P. Lin, and H. Yang, A Plant Tendril Mimic Soft Actuator with Phototunable Bending and Chiral Twisting Motion Modes, *Nature Communications* 7 (2016) 13981.
112. X. Lu, S. Guo, X. Tong, H. Xia, and Y. Zhao, Tunable Photocontrolled Motions Using Stored Strain Energy in Malleable Azobenzene Liquid Crystalline Polymer Actuators, *Advanced Materials* 29 (2017) 1606467.
113. Y. Wang, K. Li, X. Li, H. Cui, G. Liu, H. Xu, X. Wu, W. Yao, B. Zhong, and X. Huang, Electro-Thermally Driven Flexible Robot Arms Based on Stacking-Controlled Graphite Nanocomposites, *Carbon* 152 (2019) 873-881.

114. Y. Wu, J. K. Yim, J. Liang, Z. Shao, M. Qi, J. Zhong, Z. Luo, X. Yan, M. Zhang, and X. Wang, Insect-Scale Fast Moving and Ultrarobust Soft Robot, *Science Robotics* 4 (2019) eaax1594.
115. B. Shin, J. Ha, M. Lee, K. Park, G. H. Park, T. H. Choi, K.-J. Cho, and H.-Y. Kim, Hygrobot: A Self-Locomotive Ratcheted Actuator Powered by Environmental Humidity, *Science Robotics* 3 (2018) eaar2629.
116. J. Hu, X. Li, Y. Ni, S. Ma, and H. Yu, A Programmable and Biomimetic Photo-Actuator: A Composite of a Photo-Liquefiable Azobenzene Derivative and Commercial Plastic Film, *Journal of Materials Chemistry C* 6 (2018) 10815-10821.
117. M. Duduta, F. Berlinger, R. Nagpal, D. Clarke, R. Wood, and F. Z. Temel, Electrically-Latched Compliant Jumping Mechanism Based on a Dielectric Elastomer Actuator, *Smart Materials and Structures* 28 (2019) 09LT01.
118. S. Ma, X. Li, S. Huang, J. Hu, and H. Yu, A Light-Activated Polymer Composite Enables on-Demand Photocontrolled Motion: Transportation at the Liquid/Air Interface, *Angewandte Chemie* 131 (2019) 2681-2685.
119. P. Grönquist, D. Wood, M. M. Hassani, F. K. Wittel, A. Menges, and M. Rüggeberg, Analysis of Hygroscopic Self-Shaping Wood at Large Scale for Curved Mass Timber Structures, *Science Advances* 5 (2019) eaax1311.
120. B. J. Cafferty, V. E. Campbell, P. Rothemund, D. J. Preston, A. Ainla, N. Fulleringer, A. C. Diaz, A. E. Fuentes, D. Sameoto, and J. A. Lewis, Fabricating 3D Structures by Combining 2D Printing and Relaxation of Strain, *Advanced Materials Technologies* 4 (2019) 1800299.
121. N. Bowden, S. Brittain, A. G. Evans, J. W. Hutchinson, and G. M. Whitesides, Spontaneous Formation of Ordered Structures in Thin Films of Metals Supported on an Elastomeric Polymer, *Nature* 393 (1998) 146.
122. J. Lim, S. J. Choi, and P. Kim, Controlling Wrinkle Propagation in the Bilayer System with Thickness-Gradient, *Advanced Materials Interfaces* 5 (2018) 1701109.
123. J. Wang, B. Li, Y.-P. Cao, X.-Q. Feng, and H. Gao, Wrinkling Micropatterns Regulated by a Hard Skin Layer with a Periodic Stiffness Distribution on a Soft Material, *Applied Physics Letters* 108 (2016) 021903.
124. J. Y. Chung, A. J. Nolte, and C. M. Stafford, Surface Wrinkling: A Versatile Platform for Measuring Thin-Film Properties, *Advanced Materials* 23 (2011) 349-368.
125. P.-C. Lin, S. Vajpayee, A. Jagota, C.-Y. Hui, and S. Yang, Mechanically Tunable Dry Adhesive from Wrinkled Elastomers, *Soft Matter* 4 (2008) 1830-1835.

126. E. P. Chan, E. J. Smith, R. C. Hayward, and A. J. Crosby, Surface Wrinkles for Smart Adhesion, *Advanced Materials* 20 (2008) 711-716.
127. D. Chandra, S. Yang, and P.-C. Lin, Strain Responsive Concave and Convex Microlens Arrays, *Applied Physics Letters* 91 (2007) 251912.
128. D.-Y. Khang, H. Jiang, Y. Huang, and J. A. Rogers, A Stretchable Form of Single-Crystal Silicon for High-Performance Electronics on Rubber Substrates, *Science* 311 (2006) 208-212.
129. E. P. Chan and A. J. Crosby, Fabricating Microlens Arrays by Surface Wrinkling, *Advanced Materials* 18 (2006) 3238-3242.
130. W. H. Koo, S. M. Jeong, F. Araoka, K. Ishikawa, S. Nishimura, T. Toyooka, and H. Takezoe, Light Extraction from Organic Light-Emitting Diodes Enhanced by Spontaneously Formed Buckles, *Nature Photonics* 4 (2010) 222.
131. D.-H. Kim, J.-H. Ahn, W. M. Choi, H.-S. Kim, T.-H. Kim, J. Song, Y. Y. Huang, Z. Liu, C. Lu, and J. A. Rogers, Stretchable and Foldable Silicon Integrated Circuits, *Science* 320 (2008) 507-511.
132. K. Autumn, Y. A. Liang, S. T. Hsieh, W. Zesch, W. P. Chan, T. W. Kenny, R. Fearing, and R. J. Full, Adhesive Force of a Single Gecko Foot-Hair, *Nature* 405 (2000) 681.
133. K. Autumn, M. Sitti, Y. A. Liang, A. M. Peattie, W. R. Hansen, S. Sponberg, T. W. Kenny, R. Fearing, J. N. Israelachvili, and R. J. Full, Evidence for Van Der Waals Adhesion in Gecko Setae, *Proceedings of the National Academy of Sciences* 99 (2002) 12252-12256.
134. M. Scherge, S. N. Gorb, and S. Gorb, *Biological Micro-and Nanotribology* 2001: Springer Science & Business Media.
135. S. Gorb, *Attachment Devices of Insect Cuticle* 2001: Springer Science & Business Media.
136. S. Goyal, K. Srinivasan, G. Subbarayan, and T. Siegmund, A Non-Contact, Thermally-Driven Buckling Delamination Test to Measure Interfacial Fracture Toughness of Thin Film Systems, *Thin Solid Films* 518 (2010) 2056-2064.
137. M. J. Cordill, F. D. Fischer, F. G. Rammerstorfer, and G. Dehm, Adhesion Energies of Cr Thin Films on Polyimide Determined from Buckling: Experiment and Model, *Acta Materialia* 58 (2010) 5520-5531.
138. J. Andersons, S. Tarasovs, and Y. Leterrier, Evaluation of Thin Film Adhesion to a Compliant Substrate by the Analysis of Progressive Buckling in the Fragmentation Test, *Thin Solid Films* 517 (2009) 2007-2011.

139. Q. Wang, H. Xie, J. Lu, P. Chen, and Q. Zhang, Measurement of Interfacial Toughness of Metal Film Wire and Polymer Membrane through Electricity Induced Buckling Method, *Journal of Colloid and Interface Science* 358 (2011) 491-496.
140. A. Pronin and V. Gupta, Measurement of Thin Film Interface Toughness by Using Laser-Generated Stress Pulses, *Journal of the Mechanics and Physics of Solids* 46 (1998) 389-410.
141. D. Antartis and I. Chasiotis, Residual Stress and Mechanical Property Measurements in Amorphous Si Photovoltaic Thin Films, *Solar Energy* 105 (2014) 694-704.
142. T. L. Anderson and T. L. Anderson, *Fracture Mechanics: Fundamentals and Applications* 2005: CRC press.
143. O. C. Zienkiewicz, R. L. Taylor, and J. Z. Zhu, *The Finite Element Method: Its Basis and Fundamentals* 2005: Elsevier.
144. J. D. Watson and F. H. Crick, Molecular Structure of Nucleic Acids, *Nature* 171 (1953) 737-738.
145. A. Wang, G. J. Quigley, F. J. Kolpak, J. L. Crawford, J. H. van Boom, G. van der Marel, and A. Rich, Molecular Structure of a Left-Handed Double Helical DNA Fragment at Atomic Resolution, *Nature* 282 (1979) 680-686.
146. S. O. Kelley and J. K. Barton, Electron Transfer between Bases in Double Helical DNA, *Science* 283 (1999) 375-381.
147. H. Vogel, A Better Way to Construct the Sunflower Head, *Mathematical Biosciences* 44 (1979) 179-189.
148. A. Mathai and T. A. Davis, Constructing the Sunflower Head, *Mathematical Biosciences* 20 (1974) 117-133.
149. M. D. Weinberg, Detection of a Large-Scale Stellar Bar in the Milky Way, *The Astrophysical Journal* 384 (1992) 81-94.
150. A. Brunthaler, M. J. Reid, K. M. Menten, X. W. Zheng, A. Bartkiewicz, Y. K. Choi, T. Dame, K. Hachisuka, K. Immer, and G. Moellenbrock, The Bar and Spiral Structure Legacy (Bessel) Survey: Mapping the Milky Way with VLBI Astrometry, *Astronomische Nachrichten* 332 (2011) 461-466.
151. N. Yao, A. Epstein, and A. Akey, Crystal Growth Via Spiral Motion in Abalone Shell Nacre, *Journal of Materials Research* 21 (2006) 1939-1946.
152. L. Li and C. Ortiz, A Natural 3D Interconnected Laminated Composite with Enhanced Damage Resistance, *Advanced Functional Materials* 25 (2015) 3463-3471.

153. K. Wada, Spiral Growth of Nacre, *Nature* 211 (1966) 1427.
154. G. I. Taylor, The Mechanism of Plastic Deformation of Crystals. Part I. Theoretical, *Proceedings of the Royal Society of London. Series A, Containing Papers of a Mathematical and Physical Character* 145 (1934) 362-387.
155. R. F. Gibson, *Principles of Composite Material Mechanics* 1994, United States: McGraw-Hill.
156. N. Yao, A. K. Epstein, W. W. Liu, F. Sauer, and N. Yang, Organic-Inorganic Interfaces and Spiral Growth in Nacre, *Journal of the Royal Society Interface* 6 (2009) 367-376.
157. K. Tushtev, M. Murck, and G. Grathwohl, On the Nature of the Stiffness of Nacre, *Materials Science and Engineering: C* 28 (2008) 1164-1172.
158. A. K. Dastjerdi, R. Rabiei, and F. Barthelat, The Weak Interfaces within Tough Natural Composites: Experiments on Three Types of Nacre, *Journal of the Mechanical Behavior of Biomedical Materials* 19 (2013) 50-60.
159. W. Voigt, Ueber Die Beziehung Zwischen Den Beiden Elasticitätsconstanten Isotroper Körper, *Annalen der physik* 274 (1889) 573-587.
160. A. Reuss, Berechnung Der Fließgrenze Von Mischkristallen Auf Grund Der Plastizitätsbedingung Für Einkristalle, *ZAMM-Journal of Applied Mathematics and Mechanics/Zeitschrift für Angewandte Mathematik und Mechanik* 9 (1929) 49-58.
161. J. Chang, J. Q. Xu, and Y. Mutoh, A General Mixed-Mode Brittle Fracture Criterion for Cracked Materials, *Engineering Fracture Mechanics* 73 (2006) 1249-1263.
162. A. A. Griffith, The Phenomena of Rupture and Flow in Solids, *Proceedings of the Royal Society of London. Series A, Containing Papers of a Mathematical and Physical Character* 221 (1921) 163-198.
163. M. A. Volosova, S. N. Grigoriev, and E. A. Ostrikov, Use of Laser Ablation for Formation of Discontinuous (Discrete) Wear-Resistant Coatings Formed on Solid Carbide Cutting Tool by Electron Beam Alloying and Vacuum-Arc Deposition, *Mechanics & Industry* 17 (2016) 720.
164. E. Soroka, B. Lyashenko, S. Qiao, and C. Zhang, Tribological Behaviour and Cutting Performance of PVD-TiN Coating/Substrate System with Discontinuous Surface Architecture, *Rare Metal Materials and Engineering* 40 (2011) 580-584.
165. S. Ramachandra and T. C. Ovaert, Effect of Coating Geometry on Contact Stresses in Two-Dimensional Discontinuous Coatings, *Journal of Tribology* 122 (2000) 665-671.

166. V. Antonyuk, E. Soroka, B. Lyashenko, and A. Rutkovskii, Discontinuous Coatings on Cutting Tools, *Strength of Materials* 39 (2007) 99-102.
167. H. Haftbaradaran, X. Xiao, M. W. Verbrugge, and H. Gao, Method to Deduce the Critical Size for Interfacial Delamination of Patterned Electrode Structures and Application to Lithiation of Thin-Film Silicon Islands, *Journal of Power Sources* 206 (2012) 357-366.
168. H. Haftbaradaran, S. K. Soni, B. W. Sheldon, X. Xiao, and H. Gao, Modified Stoney Equation for Patterned Thin Film Electrodes on Substrates in the Presence of Interfacial Sliding, *Journal of Applied Mechanics* 79 (2012) 031018.
169. S. K. Soni, B. W. Sheldon, X. Xiao, M. W. Verbrugge, A. Dongjoon, H. Haftbaradaran, and H. Gao, Stress Mitigation During the Lithiation of Patterned Amorphous Si Islands, *Journal of the Electrochemical Society* 159 (2011) A38-A43.
170. K. L. Johnson, *Contact Mechanics* 1987: Cambridge University Press.
171. H.-H. Yu and J. W. Hutchinson, Delamination of Thin Film Strips, *Thin Solid Films* 423 (2003) 54-63.
172. A. Ingrole, A. Hao, and R. Liang, Design and Modeling of Auxetic and Hybrid Honeycomb Structures for in-Plane Property Enhancement, *Materials & Design* 117 (2017) 72-83.
173. R. Kurniawan and T. J. Ko, A Study of Surface Texturing Using Piezoelectric Tool Holder Actuator on Conventional CNC Turning, *International Journal of Precision Engineering and Manufacturing* 14 (2013) 199-206.
174. B. Pan, K. Qian, H. Xie, and A. Asundi, Two-Dimensional Digital Image Correlation for in-Plane Displacement and Strain Measurement: A Review, *Measurement Science and Technology* 20 (2009) 062001.
175. J. Blaber, B. Adair, and A. Antoniou, Ncorr: Open-Source 2D Digital Image Correlation Matlab Software, *Experimental Mechanics* 55 (2015) 1105-1122.
176. S. R. Choi, J. W. Hutchinson, and A. G. Evans, Delamination of Multilayer Thermal Barrier Coatings, *Mechanics of Materials* 31 (1999) 431-447.
177. F. Qin, J. Hu, Y. K. Chou, and R. G. Thompson, Delamination Wear of Nano-Diamond Coated Cutting Tools in Composite Machining, *Wear* 267 (2009) 991-995.
178. S. Basu, S. Suresh, K. Ghatak, S. F. Bartolucci, T. Gupta, P. Hundekar, R. Kumar, T.-M. Lu, D. Datta, and Y. Shi, Utilizing Van Der Waals Slippery Interfaces to Enhance the Electrochemical Stability of Silicon Film Anodes in Lithium-Ion Batteries, *ACS Applied Materials & Interfaces* 10 (2018) 13442-13451.

179. M. Schaldach and C. Kranz, *Stent Having Discontinuous Coating in the Form of Coating Islands*, 2004, Google Patents.

180. V. B. Shenoy, P. Johari, and Y. Qi, Elastic Softening of Amorphous and Crystalline Li–Si Phases with Increasing Li Concentration: A First-Principles Study, *Journal of Power Sources* 195 (2010) 6825-6830.

181. S. Wang, Y. Gao, A. Wei, P. Xiao, Y. Liang, W. Lu, C. Chen, C. Zhang, G. Yang, H. Yao, and T. Chen, Asymmetric Elastoplasticity of Stacked Graphene Assembly Actualizes Programmable Untethered Soft Robotics, *Nature Communications* (2020).

182. V. Singh, S. Sengupta, H. S. Solanki, R. Dhall, A. Allain, S. Dhara, P. Pant, and M. M. Deshmukh, Probing Thermal Expansion of Graphene and Modal Dispersion at Low-Temperature Using Graphene Nanoelectromechanical Systems Resonators, *Nanotechnology* 21 (2010) 165204.

183. X. Huang, P. Jiang, and T. Tanaka, A Review of Dielectric Polymer Composites with High Thermal Conductivity, *IEEE Electrical Insulation Magazine* 27 (2011) 8-16.

184. G. Carotenuto, S. De Nicola, M. Palomba, D. Pullini, A. Horsewell, T. W. Hansen, and L. Nicolais, Mechanical Properties of Low-Density Polyethylene Filled by Graphite Nanoplatelets, *Nanotechnology* 23 (2012) 485705.

185. N. Ladizesky and I. Ward, Determination of Poisson's Ratio and Young's Modulus of Low-Density Polyethylene, *Journal of Macromolecular Science, Part B: Physics* 5 (1971) 661-692.

186. Y. L. Zhu, S. N. Ma, and B. S. Xu, Finite-Element Evaluation and Improvement of a Test Procedure for Coating Shear Bond Strength Determination, *Journal of Thermal Spray Technology* 8 (1999) 328-332.

187. A. Valadez-Gonzalez, J. M. Cervantes-Uc, R. Olayo, and P. J. Herrera-Franco, Effect of Fiber Surface Treatment on the Fiber–Matrix Bond Strength of Natural Fiber Reinforced Composites, *Composites Part B: Engineering* 30 (1999) 309-320.

188. H. Era, F. Otsubo, T. Uchida, S. Fukuda, and K. Kishitake, A Modified Shear Test for Adhesion Evaluation of Thermal Sprayed Coating, *Materials Science and Engineering: A* 251 (1998) 166-172.

189. M. R. Piggott, Why Interface Testing by Single-Fibre Methods Can Be Misleading, *Composites Science and Technology* 57 (1997) 965-974.

190. J. Gunnars and U. Wiklund, Determination of Growth-Induced Strain and Thermo-Elastic Properties of Coatings by Curvature Measurements, *Materials*

*Science and Engineering: A 336 (2002) 7-21.*